Instituto de Física de Cantabria
Universidad de Cantabria y
Consejo Superior de Investigaciones Científicas

“Estudio de Nuevos Sensores de Silicio para Experimentos en Futuros Colisionadores de Partículas”

“Study of New Silicon Sensors for Experiments at Future Particle Colliders”

Memoria presentada por
A dissertation submitted by

Francisca J. Muñoz Sánchez

para optar al título de Doctora en Física
for the degree of Doctor of Philosophy in Physics

Director: Iván Vila Álvarez
Santander, Marzo de 2014

Este trabajo ha sido financiado por el Ministerio de Ciencia e Innovación (actualmente Ministerio de Economía y Competitividad) de España a través de los proyectos FPA 2007-66387 "I + D en detectores y estudios fenomenológicos para el colisionador lineal internacional" y FPA 2011-28694-C02-01 "Física de colisionadores hadrónicos".

Esta tesis ha sido desarrollada dentro del "Programa Oficial de Doctorado en Ciencias, Tecnología y Computación" regulado por el Real Decreto 1393/2007 (BOE núm. 36, de 10 de febrero de 2010. RUCT: 5310324) con mención hacia la excelencia (BOE núm. 253, de 20 de octubre de 2011. Referencia:MEE2011-0061).

Para la realización de esta tesis, Francisca J. Munõz Sánchez ha disfrutado de una ayuda del subprograma de Formación de Personal Investigador (FPI) en el organismo Consejo Superior de Investigaciones Científicas (CSIC) y en el centro del Instituto de Física de Cantabria (IFCA). Durante la misma y para fomentar la excelencia del programa de doctorado, la formación de la doctoranda y para la obtención de la Mención Internacional en el título de Doctora en Física concedida por Orden ECD/3628-2011 de 26 de Diciembre (BOE de 14 de Enero de 2012), la autora ha realizado una estancia breve en el Centro Europeo de Investigación Nuclear (CERN) con una duración de cuatro meses - de Enero a Mayo de 2011- bajo la supervisión del director del laboratorio de detectores de estado sólido del CERN, el Dr. Michael Moll.

A mi gran familia "Tropela"
y a las crías

Nothing in life is to be feared, it is only to be understood.

En la vida no hay nada que temer, solo hay que entender.

Marie Sklodowska Curie

Agradecimientos

Eto era una vè una zagalica de "Lo Tropel" en Cantabria...

Más de 4 años y medio de mi vida he pasado haciendo mi tesis doctoral en el IFCA, en Santander y son muchas las cosas que tengo que agradecer.

Iván Vila ha sido el director de esta tesis y él tiene por tanto parte de culpa en que yo esté donde estoy ahora. De él he aprendido a buscar entender el por qué de cada cosa tan al detalle como sea posible, a ser sistemática, a realizar los más rigurosos análisis y tantas medidas como sean necesarias, a discutir y a perseverar. Me ha animado a viajar, a acudir a congresos y a trabajar con gente de otros países en otros países.

En el IFCA tengo que estarle agradecida a todo el personal del IFCA, en particular al grupo de física de altas energías y en especial: a Santi, mi amigo y familia desde el principio de esta aventura y espero que hasta el final de ésta y de otras muchas que vendrán; a Esteban, por su apoyo incondicional tanto dentro como fuera del IFCA; a Richard por su paciencia en el laboratorio o en test beams donde hemos tenido malos y buenos momentos entre pasitos, sensores y láseres. A Marcos, el chico "test beam", gracias por facilitarme las cosas en el CERN, donde hemos aprendido a hacer frente a "casi" cualquier situación. A Gerva, por animarse a "hardwarear", por su apoyo y necesarias correcciones.

A esos chicos del café donde echamos unas risas, habláis de fútbol o arreglamos el mundo. A Jordi, porque siempre que se lo he pedido ha estado disponible y me ha ayudado. A Javi, que aunque hemos coincidido muy poco, hemos compartido despacho, el final de nuestras tesis y momentos "de foto" bastante divertidos .

A las chicas del grupo, Teresa, Rocío, Alicia, Amparo y Ana por servir de inspiración y de ánimo a las que empezamos en esto. A Teresa en especial, por su ánimo, su interés y sus siempre acertadas palabras, por su sinceridad y por ponerme los pies en el suelo.

A Miguel Ángel por tantas risas y tanta paciencia, por aguantarme y por su disponibilidad a ayudar, gracias.

No puedo olvidarme de gestión: Chichina y sobre todo a Silvia e Inés que siempre sonríen y me han hecho mucho más fácil el lidiar con los temas burocráticos (o no) durante estos años.

En el CNM, tengo que agradecer a todo el grupo: Giulio, David, Consuelo, Celeste, Joaquim y Manolo, por acogerme como una más y hacer que me sintiese miembro del CNM desde que crucé sus puertas, he aprendido mucho de vosotros. En especial agradezco la colaboración, el reconocimiento y el apoyo recibido de Giulio, David, Salva y Rogelio durante estos años; a Daniela, todo lo que hemos aprendido y reído juntas tanto dentro como fuera del laboratorio.

Tengo que dedicarle unas líneas al grupo de Granada, el que me vió nacer. Antonio y Sergio, gracias por vuestra confianza, por hablarme siempre claro y por seguir ahí cada vez que os he necesitado. Gracias Melga y Ángel, por ayudarme a dar mis primeros pasos entre galletas en un laboratorio.

Gracias a mis amigos en la ciudad más bonica del mundo, Granada: Eli, Isa, Jose, Dani, Rakel, Pablo, Bea, Sheila, Antonio, Jorge, Lidia, Alberto, Ayrton, Pepe, Farid... por todos aquellos buenos momentos, por mantener el contacto y porque he sentido vuestro apoyo estos años en los que cada uno está en una parte del mundo.

A mi familia de inmigrantes en la tierruca... Carolina, Ana, Bea, mi querido Jorge, Santi, Esteban, Jony, Patri, Pelayo, Ana, Anita y Maricruz. Gracias porque siempre nos hemos animado, acompañado, escuchado y apoyado los unos a los otros, por las risas, las rutas, las cervezas, las cenas, los conciertos, kinitos y juegos, por los abrazos... en definitiva gracias por haber gastado parte de vuestro tiempo conmigo. En esta famila destacan Carol, Ana y Bea, compañeras de piso y de vida. ¡Una gran suerte la de encontrarnos (y la de encontrar a Ricky)!. Gracias a los tangueros, en especial a Pilar, Miguel y Angelines. Por estar ahí incluso cuando soy yo la que no estoy.

A las crías (y cía): ¡Gracias! Siempre estáis, cada una con su vida pero en cada vida.

Por último y lo más importante, a mi familia “tropela”, por su esfuerzo para que yo estudiase Física en Granada. Por enseñarme a afrontar los problemas con valentía y esfuerzo, a no tener miedo a equivocarme o a empezar de cero. Por su apoyo incondicional, pero sobre todo por su amor, el que siempre siento conmigo a pesar de la distancia.

Acknowledgements

I am very grateful to the Solid State Detectors laboratory team at CERN, were I expended four months. Michael, Nicola, Irena and Markus, you accepted me sooner than later as one of yours, thanks!. Nowadays, I can confirm that all I know about radiation damage I learned from you, together with how to set up a TCT setup; and at the some point, in a very natural way, you became very good friends. We shared tons of physics discussions, smiles, guffaws and also some beers and songs. Michael, I have to thank expressly your support to me and my career in recent times.

In the same way I am very grateful to the Laboratory for particle physics team at PSI. Tilman, Hans Christian, Silvan, Beat, Danek, Wolfram, Frank and Roland, all of you accepted me very quickly in your team. Your advices and discussions during the weekly meetings were extremely helpful. All of you were always ready to teach and help me. I thank specifically: Silvan your availability to wire bond sensors; Hans Christian for your effort helping us with the bump bonding machine alignment; Beat for your help with the test boards firmwares and Tilman for your patient teaching about all you know about pixel sensors sitting with me in the lab, in a board, in the PC or in the test beams. I was very lucky having you supporting me from that time and until now. Tilman, I found myself very comfortable learning from you, working with you. Thanks for giving me your time. It was a great present.

During these years I had the opportunity of working with many other people from other institutes in several test beams. In my first test beam I got the support, help and friendship of the HEPHY team (Tomas, Marko, Manfred and Christian). I shared time and frustration with Stefan and Thomas from the KIT team in a test beam “without beam”. In several of them, I worked with ETHZ team (Dmitry, Andrey and Marco), I thank specially Andrey his patient and chip-calibration lessons that were extremely helpful and useful. Finally, I can not be more grateful to the support that we had in DESY test beams from the CMS pixel team and telescope crew. Daniel, Simon and Hano, I really appreciate the time that you dedicated on helping us either during the test beam or later with the data analysis that close this dissertation.

Contents

Contents **i**

Preface **xi**

1 Introduction **1**

1.1 Motivation 1
1.2 Semiconductor detectors 5
  1.2.1 Hybrid detectors 7
  1.2.2 Monolithic detectors 20
  1.2.3 High Voltage CMOS. HV-CMOS 23
  1.2.4 3D-Integration detectors 24
1.3 Microtrip and pixel sensors beyond tracking and vertexing . . . 25
1.4 Summary of trends on semiconductor detectors 28

2 Silicon detectors **31**

2.1 Semiconductor detectors. Silicon 32
  2.1.1 Doping 32
  2.1.2 PN-Junction 34
  2.1.3 Principle of operation 36
  2.1.4 Basic structures 37
  2.1.5 3D detectors 39
2.2 Signal formation 41
  2.2.1 Ramo's Theorem 41
  2.2.2 Signal processing 42
  2.2.3 Noise contributions 44

2.2.4 Ballistic deficit 47

2.3 Radiation damage in Silicon 48

2.3.1 The NIEL hypothesis 49

2.3.2 Impact on the detector 51

3 Laboratory Techniques 55

3.1 Electrical Characterization 56

3.1.1 Description and objectives 56

3.2 Laser characterization 66

3.2.1 Setup description 67

3.2.2 Test-stand optimization 67

3.3 Characterization with a radio-active source 69

3.4 Test Beam Characterization 73

3.4.1 DESY Facilities 73

3.5 Irradiation Facilities 76

4 Novel 2D position sensitive microstrip sensor 79

4.1 Resistive charge division in microstrip detectors 80

4.1.1 Resistive charge division 80

4.1.2 Description of the prototypes 81

4.1.3 Effect of the resistive electrodes on the detector response 82

4.2 Electrical characterization 84

4.3 Laser Characterization 86

4.3.1 Readout electronics 86

4.3.2 Model and simulation of the detector 86

4.3.3 Laser Measurements 90

4.4 Noise sources and its contribution to the position resolution . . 94

4.4.1 Position error estimation 95

4.4.2 Measured noise in prototypes 98

4.5 Signal to noise evaluation 102

4.6 Prototypes with integrated signal routing lines 102

4.7 Study of parasitic couplings 106

4.8 Summary 107

5 3D pixel detectors 111

5.1 Introduction 111

5.1.1 The CMS vertex detector 112

5.1.2 The vertex Phase II upgrade 114

5.2 Description of the devices 115

5.3 Electrical characterization 118

5.4 Readout Chip. PSI46 123

5.5 Interconnection process 126

5.5.1 Bump bonding test in 3D pixel sensors 129

5.6 ROC calibration 131

5.6.1 ROC qualification in irradiated samples 136

5.7 Radioactive Source Characterization 137

5.8 Test Beam characterization 140

5.8.1 Unirradiated sensors 141

5.8.2 Irradiated sensors 147

5.9 Summary of the results and next steps 152

6 Conclusions 155

Resumen 159

1 Motivación e Introducción 159

2 Descripción de dispositivos 161

2.1 Detectores de microtiras sensible en dos coordenadas . . 162

2.2 Detectores de píxeles con tecnología 3D 162

3 Técnicas de Laboratorio 163

4 Resultados 164

4.1 Detectores de microtiras sensible en dos coordenadas . . 164

4.2 Detectores de píxeles con tecnología 3D 165

5 Conclusiones 166

List of Figures 169

List of Tables 175

Bibliography 177

Preface

This dissertation is submitted for the degree of Doctor of Philosophy in Physics at the University of Cantabria. The research described herein was conducted under the supervision of Doctor Iván Vila Álvarez at the Instituto de Física de Cantabria (IFCA) between September 2009 and March 2014.

This work is on the study of novel silicon sensors for experiments at future particle colliders. The characterization techniques and results of two types of detectors is presented:

- Two dimensional position-sensitive microstrip sensors
- Double-sided 3D pixel sensors

Except where references or acknowledgments are made, the work and results here presented are original.

Chapter 1

Introduction and Motivation

1.1 Motivation

In the last decades, several high energy discovery machines have been developed. The two biggest were LEP (CERN, Geneva) [1] and Tevatron (Fermilab, Chicago) [2]. Both machines were circular colliders, colliding electrons and positrons or proton and antiprotons respectively, and were able to discover new particles already predicted by the standard model, such as the W and Z bosons in LEP or the top quark in Tevatron.

The Large Hadron Collider (LHC) [3] has been successfully operating since end 2010 at the European Laboratory for particle physics (CERN), in Geneva. LHC is a circular collider of protons or lead ions. This machine accelerates bunches of hadrons or ions until they reach speeds close to the light speed, and makes them collide in four different points along their trajectory. On all those points there is an experiment: ALICE studies ion collisions [4], trying to understand the first instants of the Universe, LHCb [5] studies b-particle physics and tries to understand the matter- antimatter asymmetry and finally, CMS [6] and ATLAS [7], have been built as general purpose experiments. CMS and and ATLAS collaborations announced the discovery of a new Higgs boson like particle on 4^{th} of July, 2012. This discovery has been confirmed with the later data collected until the 2013 technical stop of the LHC.

In Figure 1.1 a schematic of the CMS experiment is shown and several particle tracks are visible. Collider experiments are huge and have a cylindrical symmetry around the beam axis with a layers structure. From the outermost to the innermost layer, the most external layer is a muon spectrometer, then hadronic and electromagnetic calorimeters and finally the innermost subdetector is the tracker, which is composed by several layers of silicon detectors. Radiation interaction with the different detector layers allows to identify the particles. For example, while a muon interacts with all the experiment detector layers, a photon interacts only with the electromagnetic calorimeter and a hadronic particle will end its trajectory at the hadronic calorimeter.

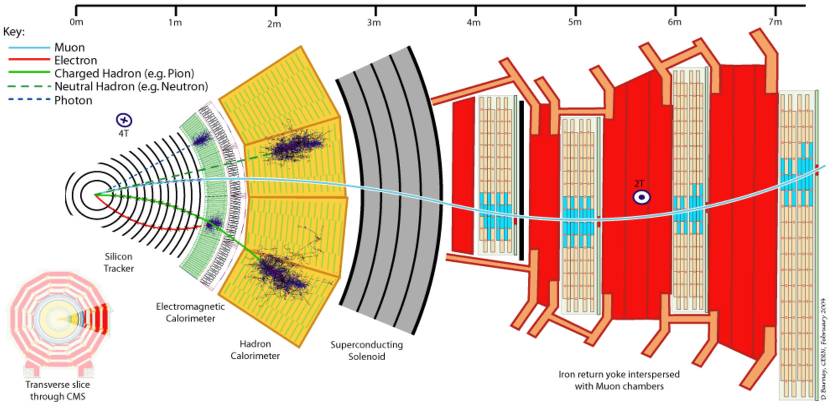

Figure 1.1: *Schematic of the CMS experiment. From left to right: Silicon tracker, electromagnetic and hadron calorimeters, the superconducting solenoid and the muon chambers are the different sub-detectors that form it. Different particle tracks are also visible.*

In this thesis the technologies under study belong to the silicon tracker. A silicon tracker can be divided in two sub-detectors: vertex and tracker. The vertex detector is made of pixel detectors and is formed by the innermost layers of the silicon tracker (in the case of CMS the three innermost layers), it has the highest granularity and its main objective is to be able to resolve secondary interaction vertices. The tracker detector is made by microstrip detectors, the granularity is lower but still high enough to reconstruct tracks with a resolution below tens of micrometers.

Semiconductor silicon sensors are being used in high energy physics experiments for the last thirty years [8] becoming a standard technology in tracking detectors. In these experiments several characteristics are required. A high granularity is necessary to reach low occupancy and a good resolution on the position measurement. Simultaneously the material has to be reduced as much as possible to reduce multiple scattering. In terms of sensor performance a small amount of energy must produce a signal big enough to be detected and the used technology must be radiation resistant. These characteristics must be balanced against material and processing technology cost, which are also important properties when large surfaces have to be covered with sensors (a full description of silicon sensors working principles and performance is given in chapter 2).

However, the requirements for future collider detectors are more demanding than in present experiments depending on the accelerator nature. New accelerators point either to higher luminosities, as is the case of a High Luminosity Large Hadron Collider (HL-LHC) [9] where sensors will endure higher radiation doses or to higher precision machines as in the case of future linear colliders, like the International Linear Collider (ILC), where while the radiation fluences are not expected to be as large as in the HL-LHC scenarios, the granularity has to increase considerably and the material budget has to be reduced down to very low values to improve the measurement's accuracy.

The HL-LHC has as main objective to increase the LHC luminosity from $10^{34}\mathrm{cm}^{-2}\mathrm{s}^{-1}$ to $5\times10^{35}\mathrm{cm}^{-2}\mathrm{s}^{-1}$, therefore the fluences of particles hitting the detectors will rise significantly, especially in the innermost layers of the detector, increasing occupancies and radiation damage in silicon sensors. The collaboration RD50 [10] studies the performance of different silicon substrates and technologies after irradiation.

The International Linear Collider [11] will collide electrons and their antiparticles, positrons, at nearly the speed of light. Surrounding the collision point will be an experiment (ILD or SiD) [12]. The beams collide 14,000 times every second at high energies (500 GeV - 1 TeV). Each collision will produce a bunch of particles that allow to make high accuracy measurements in particle properties and also discover new physics beyond the standard model. The tracker detectors at ILC will require mainly to decrease as much as possible the material budget keeping high detector granularity. Therefore it requires as light materials as possible, affecting mainly to the cooling system. Another important technological challenge is the pulsed powering for decreasing the energy dissipation while working in the standby mode, but implies new studies in the detector and electronic technologies.

The structure of this thesis is as follow: in this chapter, the state of the art in silicon sensors used in collider's trackers is reviewed, the recently developed technologies as well as future trends; the purpose of this chapter is the contextualization of this work inside the particle physics (also called High Energy Physics, HEP) field as well as its industrial applications in other areas; in chapter 2, a view of a silicon sensor from the solid state physics point of view is given, as well as a brief description of the signal processing; a detailed description of the laboratory setups and techniques is given in chapter 3; in chapter 4 results from the qualification of new 2D position-sensitive microstrip detectors are presented and in chapter 5, results of the characterization of 3D double-sided pixel detectors are shown.

This thesis focuses on the qualification of two different new silicon devices as proposals for future tracking systems:

- **Microstrip sensors** with resistive electrodes instead of the standard metallic electrodes [13]. This allows the implementation of the resistive charge division method to determine the particle impact point along the strip while the perpendicular coordinate is extracted using the capacitive charge sharing between strip as usual for microstrips detectors. These kind of technology could be appropriate for a future linear collider or in experiments where the material budget is crucial. In this work, proof of concept as well as performance of prototypes of 2D position sensitive strip detectors and a detailed noise study is presented in chapter 4.

- **Pixel sensors** with an array of vertical electrodes, also called 3D-pixel sensors. This kind of technology shows higher radiation resistance, and is suitable to work in experiments that will be exposed to high particle fluences, like HL-LHC. These sensors present also some other technical advantages described in chapter 5. A full characterization of these devices was done, starting from a full electrical characterization to know their functionality and electrical parameters and studying the performance of theses sensors under their exposure to a radioactive source and in a test beam before and after irradiation. These measurements show what is the depletion voltage and signal in the device after irradiation. Comparing them against the unirradiated samples responses, the radiation damage in terms of sensor efficiency and performance can be evaluated. A complete irradiation campaign was done, irradiating several samples up to fluences of $1{\times}10^{16}\mathrm{n}_{eq}/\mathrm{cm}^2$ which is similar to the expected value in HL-LHC in the closest layers to the collision point. The irradiations were done in a TRIGA reactor in Ljubljana [14] and in a proton cyclotron in Karlsruhe [15] using the full energy spectrum of reactor neutrons and 23 MeV protons respectively.

1.2 Semiconductor detectors

Silicon sensors are used in tracker systems for collider experiments; they give information about the charged particle's trajectory. To know what are the hit positions in the sensors, sensors are classified according to their diode segmentation pattern as pixel sensors if they are divided in an matrix of diodes (pixel cells with a size $\sim$ 100 µm × 100 µm), and as microstrips sensors when the sensor is segmented in thin parallel microstrips having a width of tens of microns and a length of several centimeters. In Figure 2.3 the two different detector segmentations are shown. In this example the segmentation is done in the pn-junction side, but it can be also done in the ohmic contact. Every channels in a strip detector can be readout from a side while in a pixel detector the readout electronic has to be one-to-one and needs to be placed on top of the sensor.

In collider tracker detectors, the ideal detector will have as much granularity as possible in a good balance with the material budget. Pixels offer a good granularity, but need one to one read-out, making the interconnection process and data handling more difficult, adding material in the sensitive area (read-out chip and bumps) and increasing the cost of the technology. These needs make pixel technologies not feasible to cover large areas. Usually pixel detectors are in the innermost layers close to the interaction point to resolve secondary vertices and microstrip detectors are in the outer layers of the silicon tracker.

The tracker resolution has a very important role in the final track reconstruction and therefore in the identification of the involved particles and

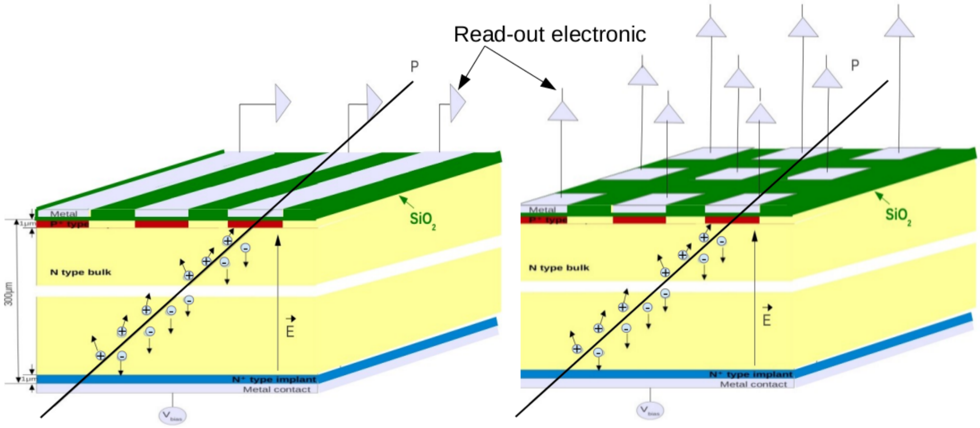

Figure 1.2: *Basic structure of p-on-n type sensors. Left: microstrip sensor. Right: Pixel sensor.*

physics. Talking about semiconductor detectors, three different elements have to be distinguished: sensor, readout electronics and their interconnection.

Detectors are classified depending on how these three structures are integrated in a full device as: hybrids, monolithic or 3D-integration detectors.

The coupling in segmented silicon sensors is relevant [16]. Each strip or pixel of a silicon sensor must be connected to its own readout channel. This can be done in two different ways. One way is a direct connection from the strip or pixel to the amplifier input (DC coupling). This implies that the amplifier must sink a fraction of the detector leakage current that corresponds to the strip or pixel. This contribution is usually small on pixels because of their limited size, but can be much higher than the signal current in strip detectors, especially in irradiated ones. The leakage current depends on the applied bias voltage and the radiation damage, it is difficult to build an amplifier which can handle such a wide range of input currents. The solution is to bypass the DC leakage current over a resistor and pick up only the AC part over a capacitor (AC coupling). Obviously, this is the preferred technique for present silicon detectors.

In silicon strip detectors, resistors and coupling capacitors are usually integrated into the sensor. The bias resistor is commonly implemented as a polysilicon structure, which is less vulnerable to radiation damage. The ca-

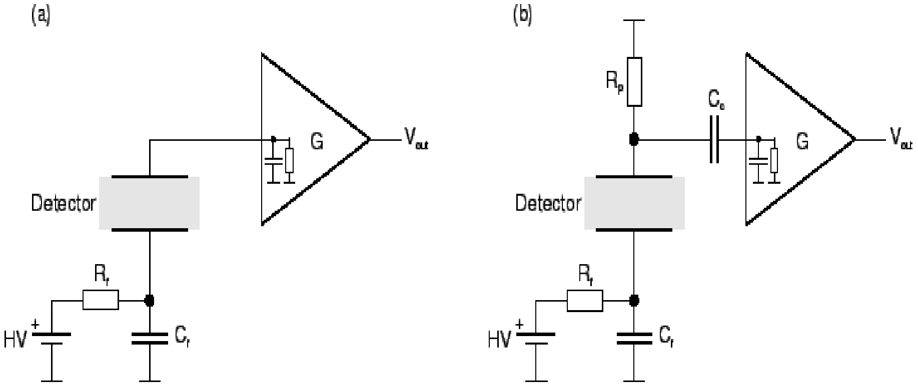

Figure 1.3: *DC coupling (a) and AC coupling (b) in silicon detectors. Both cases implement the backplane bias voltage filtered by an RC network. Source: [16].*

pacitor is built by a metal layer over silicon oxide on top of the strip implant. The bias voltage, which is applied to the backplane, is usually decoupled with an RC filter. In Figure 1.3 a schema of both couplings is shown.

After this introduction, a brief review on the silicon sensor technology is given next. The sources for this section are mainly three different review jobs ([8], [17], [18]). Any other reference will be detailed in the text.

1.2.1 Hybrid detectors

In a hybrid detector, readout electronic and sensor are developed separately and require an interconnection process to build the final detector. A hybrid detector can be AD or DC coupled as it was explained above.

Among hybrid detectors we can distinguish between microstrip and pixel sensors depending on the diode segmentation.

- **Microstrip detectors**.
  In a microstrip detector every strip can be readout through an ASIC usually located at one end of the strips, therefore the interconnection process used to connect sensor and readout chip is the ultrasonic wire bonding that is a low-cost standard technique used in the semiconductor industry. The resolution on the position along the transverse coordinate to the strip is determined, in the case of binary readout, by the distance between strips or pitch (p) with an accuracy of $\sigma = p/\sqrt{12}$.

As an example of microstrip detector in tracker colliders, the strips sensor used in the CMS tracker are 10 cm × 10 cm single-sided, AC-coupled silicon strip sensors with polysilicon bias resistors and a single guard ring structure. It is manufactured in a standard p-on-n planar technology process on medium to high resistivity silicon. The strip pitch varies from the inner to the outer layers keeping constant the strip width to pitch ratio at 0.25. The pitch is tuned in order to match the electronic modularity of 128 read-out channels, which are the read-out channels in the APV25 read-out chip at CMS strip tracker detector [19]. A complete description of the design and qualification of current and future CMS microstrips sensors is included in reference [20].

The most common strip detectors nowadays have a pitch of 80 μm which give them a geometrical resolution $\sigma \sim 20\mu m$. This resolution on the position measurement can be improved by interpolation thanks to the charge sharing between several strips. Neighbors can also have analog signal due to diffusion, capacitive coupling (inter-strip), Lorentz angle or inclined tracks. Thanks to these effects, that imply to have signal also in neighbor strips, the position determination becomes more precise using the cluster-finding algorithms [21].

Microstrip sensors technology evolution have two main trends: one is in the sensor layout, by decreasing the pitch between strips in the device or by adding intermediate strips to favor the charge sharing between strips. The other one is based on the fact that sensor and read-out chip pitches don't fit each other and a so-called *pitch adapter* is need. There are also researching lines on the pitch adapter integration on the sensors.

- **Layout trends.**
  Some experiments use the so-called *Double Sided double Strip* detectors. Those detectors segment also the backside of the sensor in the perpendicular direction to the opposite part. In this way, in a single sensor, a two-dimensional position measurement is achieved. The limitation in these detectors is the fact that they have some fake events at high occupancy. One proposed partial solution is to have the strip from different sizes rotated by a small angle between

each other instead of a perpendicular one (*"small-angle stereo"* technique). In such a way, the appearance of ghost hits is quite suppressed, but with a deterioration of the second coordinate resolution.

There are also several studies on the insertion of an *intermediate strip* (not readout) in between two strips that are readout. This allows to produced an extra capacitive charge division. In this case the used algorithm is called η-algorithm [22]. Conclusions from the BELLE II collaboration [23], show that the most convenient configuration, for their application, is a microstrip sensor with 50 μm pitch, a single intermediate strip and a strip width of 12.5-17.5 μm. This is the one that offers a better performance in terms of signal to noise ratio (S/N) and resolution (5μm).

Other studies [24], in this case in the CMS collaboration, are developing a full characterization campaign (HPK-campaign), testing different structure geometries. A new structure was included to study sensor performance depending on strip geometries, it is called *Multi-Geometry Silicon Strip Detector (MSSD)*, manufactured by Hamamatsu [25]. A MSSD consists on different strip geometries in a single detector with different pitch, strip-width to pitch ratio (w/p) and insulation material between the n-electrodes (p-stop or p-spray). Up to now they confirmed that sensors with n-electrodes performance is better after irradiation than those with p-electrodes, that p-spray insulation performs well after irradiation and there are still not relevant conclusions in terms of geometry parameters.

A novel technology in strip sensors is the so-called *FOSTER - **FO**urfold segmented **ST**rip sensors with **E**dge **R**ead-out.* This new sensor layout is also included in the CMS-tracker HPK-campaign [26, 27]. The fourfold strip segmentation gives the sensor a higher granularity, the strips are read-out at the edges. The sensor is divided in two identical halves with a bias line and routing lines are carried out to read-out the full sensor (See Figure 1.4). Up to now the qualification measurements show that there is capacitive coupling between the routing lines and the implants and deeper studies are ongoing.

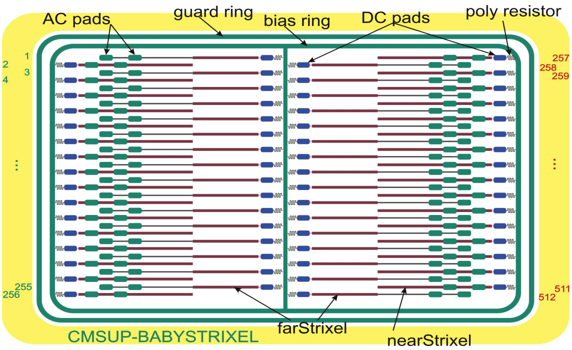

Figure 1.4: *Structure of FOSTER sensor. Source: [27].*

Another novelty in strip sensors is the two dimensional position-sensitive strip detector [13]. These detectors have a resistive electrode instead of the usual metal one. In this way, capacitive charge sharing between strips gives the position in the transverse direction to the strips and the resistive charge sharing along the electrode gives the coordinate along the strip, this technique is known as *charge division*. Chapter 4 of this thesis is dedicated to this sensor and its performance, including results after its characterization using two different sensor layouts, one that includes a metal routing for the readout and one that does not include it.

- **Routing trends**

  As has been explained before, the sensor and read-out chip pitches usually don't fit each other and a *pitch adapter* is necessary as interface between them. Those pieces have to be placed between sensor and chip and they need some space. Novel studies are integrating pitch adapters in the sensor itself [28]. Two kinds of these sensors can be distinguished.

  There are sensors with a single metal layer, where there is not metal overlap (see Figure 1.5). The area of the sensor at the pitch adapter has no metal layer on top of the strip implants.

  There are also designs with two metal layers, the total of the strips are covered with the metal, allowing the signal transfer through it.

In this case, the pitch adapter metal structure overlaps with strip metal vias.

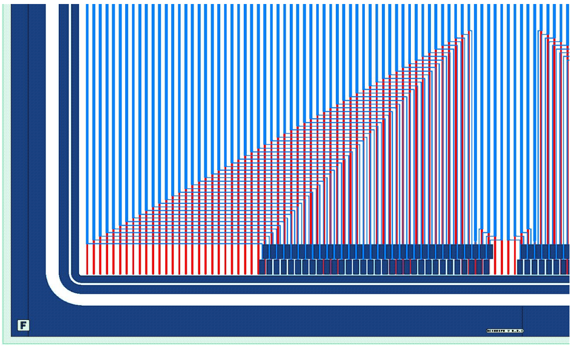

Figure 1.5: *Layout of an integrated pitch adapter in the sensor itself. It has a single metal layer (blue indicates metal vias and red indicate implants). Source: [28].*

Results so far show that sensors with a single metal layer perform as expected. The S/N when the particle's hits are outside of the pitch adapter area is equal to the S/N obtained in a standard strip detector, and the S/N over the pitch adapter area decreases as a function of the length of the metal line missing over the implant. This is a consequence of the high resistivity of the implant that causes a signal attenuation along the way where the signal is not transmitted through a metal via.

- **Pixel detectors.**
  A pixel sensor is a matrix of silicon diodes where every cell (matrix element) is read-out by an Application-Specific Integrated Circuit (ASIC) cell that includes amplification, discrimination and read-out. This requires a one-to-one connection for reading out. All these readout cells are implemented in an ASIC chip. The high segmentation of a pixel sensor makes necessary a large number of channels to read-out. In Figure 1.6 a schematic of a hybrid pixel detector is shown, and requires of a non standard interconnection process. Nowadays, the used process is the so-called *bump bonding technique*, but new techniques known as *Solid Liquid Inter-Diffusion (SLID)* are under study.

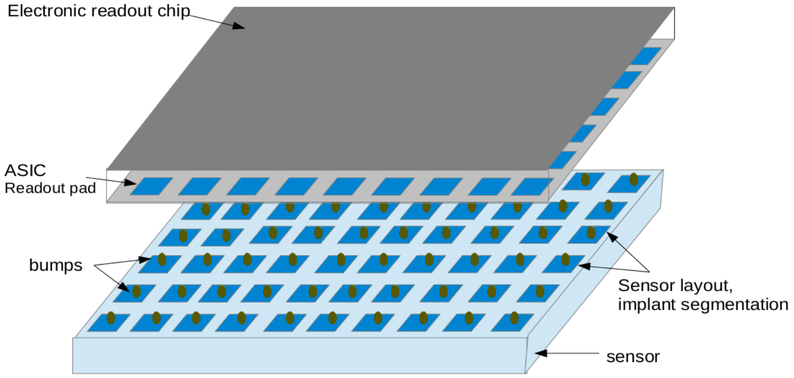

Figure 1.6: *Schematic of a hybrid pixel sensor. The sensor and readout chip are connected by bumps.*

- Interconnection Techniques.

  The *Bump Bonding* technique is based on an electrochemical process. This complex mechanism can be summarized in three main steps: first is the *underbump metalization* where a layer of a metal mixture is deposited on top of the metal contact for each unit-cell or pixel. Second is the *"reflow"* that occurs when this metal mixture is heated until it melts and by surface tension transforms into a metal ball. The third step consist on the flip-chip and reflow; the connection between sensor and the Read-Out Chip (ROC) is made and a *"second reflow"* is needed to stabilize the connection. This second reflow facilitates the self-alignment between sensor and ROC thanks to the surface tension during the melting process.

  Some of the disadvantages of this technique are its complexity and that the wafers have to be pre-processed, the underbump metalization has to be done over complete wafers, where the size of the bumps and pitch between connections are, nowadays, limited to 20 and 50-100 µm, respectively due to technical restrictions. However, this kind of connections have shown to be solid and give a very high yield per sensor (99.9% of working connections). A more detailed schema of bump-bonding technique is shown in Figure 1.7, where the particular case of the technique used in the CMS pixel detector is shown. The main metal used in the bumps is indium. A complete description of this process is in reference [29] and in chapter 5, where a detailed description of this technique applied to 3D pixel sensors is included.

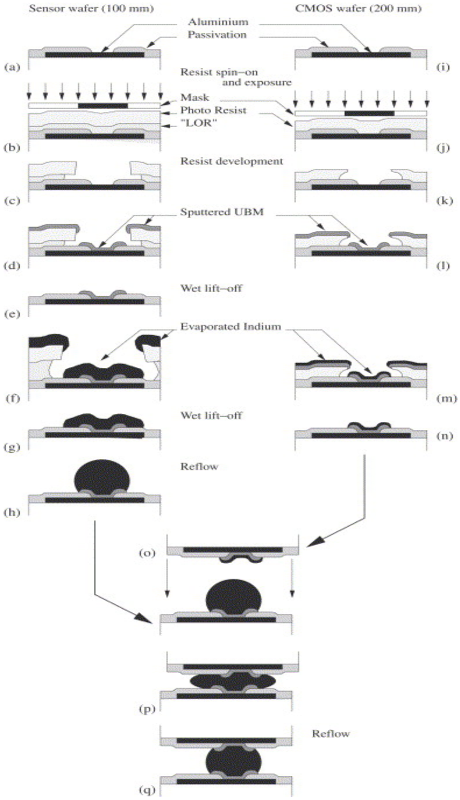

Figure 1.7: *Diagram of bump-bonding technique. From (a)-(g) is the underbump metalization in case of the sensor and from (i) to (n) in case of the ASIC chip (all these steps are made on wafer). Step (h) is the first "reflow" after dicing. Steps (o) and (p) are the flip-chip process and the final step (q) is the second and final "reflow" after which the contact is finally stable and robust. Source: [29].*

The *wire bonding* interconnection process is also used in pixel sensors, but can only be used in those pixels with a projected read-out, read by rows or strips.

The *SLID interconnection* technique is under study in the framework of the ATLAS pixel upgrade as an alternative to the bump bonding technique [30]. This technology can be summarized in different steps, the main of them are represented on Figure 1.8: the last metal layer on the wafers is done by a BCB (Benzocyclobuten) coating that offers a higher planarization and isolation; chip and sensor need a 100 nm thin TiW diffusion barrier, the process continues with the electroplating of a 5 µm Cu layer in sensor and chip, and only in one side an extra Sn 3 µm thick layer is applied on top of the Cu layer. The connection is formed when both devices are aligned and heated up to 240-320 ℃. At that temperature, the tin melts and diffuses into the copper to form a Cu_3Sn alloy.

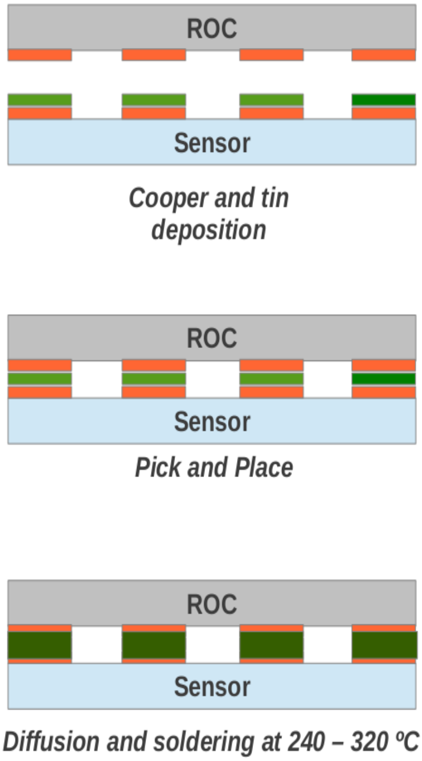

Figure 1.8: *Schematic of the SLID process. Different metal layers to build the final connection alloy are distinguishable.*

Some advantages of this process are that the connection size can be reduced to 10 µm, the pitch reachable between connections is smaller (20 µm) and less process steps are needed, which can reduce the production cost.

- **R & D trends in hybrid detectors**

  Silicon sensors, used in a hybrid pixel detector, can be classified in terms of silicon materials (depending on the silicon's ingot growth process), in terms of doping type (p or n bulks) or in terms of the diode junction layout (as a function of their internal geometry: planar or 3D structure). In this section, the differences and our current knowledge of how these different implementations influence the sensor's radiation hardness are briefly reviewed.

  Silicon growth techniques. There are several growth techniques to produce the monocrystalline silicon needed for detectors manufacturing. The most frequently used are Float Zone, Czochralski and Epitaxial.

  - Float Zone process (FZ). It is the most commonly used in silicon detectors. This kind of silicon production has a high crystalline purity and high resistivity. This process was invented by Theuerer in 1962 [31] and starts with a highly polycrystalline bar and a monocrystalline seed in an Argon atmosphere where oxygen can be added making the silicon more radiation hard. Seed and bar are in contact and using a radio-frequency (RF) field as heating to melt the ingot, the bar will take the crystal's seed orientation. With this technique is easier to have more homogeneous p-type silicon than n-type.
  - Czochralski process (Cz). It can be divided into standard Cz (SCz), magnetic field applied Cz (MCz) and continuous Cz (CCz). The MCz is nowadays the standard Cz technology because it achieves higher homogeneity. The process, from a general view, consists of melting high purity silicon in a quartz container able to rotate around a central axis (in this step dopant can be added to reach the desired intrinsic resistivity). Then a monocrystalline silicon seed is introduced in the "bath" and slowly extracted of the bath.

The material in contact with the seed will cool down acquiring the crystal seed orientation. An external magnetic field is applied during the process to control density and temperature allowing to obtain higher uniformity in the ingot. Silicon wafers developed using the Czochralski method [32] show a better thermal stress resistance, are faster and cheaper to produce and have high oxygen concentration.

- Epitaxial process (Epi) [33]. This method is based on chemical vapor deposition, which requires a support wafer acting as an ohmic contact. Silicon with the required dopants is evaporated in a vacuum chamber, depositing on the support wafer and acquiring its crystal orientation. Simultaneously, oxygen is diffused into the new layers keeping the higher concentration closer to the supporting wafer. This process allows to develop substrates with very thin active areas and high oxygen concentration.

Sensor doping. Doping silicon ingots, the bulk resistivity and carriers concentration is tuned. They can be n or p doped. The difference between p-type or n-type silicon bulks is in the dopants nature, having more acceptors or donors, respectively. Dopants typically used in n^+ contacts are phosphorus ions while boron is used to create p^+ contacts both added by implantation. After the dopants implantation an annealing time is required to anneal the radiation damage and to activate the dopants.

In silicon detectors bulk and electrodes are doped. We refer either to the doping type in the bulk or in the read-out electrode implants or both. The doping type becomes more important after irradiation because the radiation damage affects differently depending on the bulk doping type. While a n-type bulk will suffer type inversion, the p-type will become more p-type with increasing radiation exposure. These radiation effects will be described in more detail in the next chapter.

Another technological aspect to take into account is the type of carriers collected. In the literature it is found quite frequently “n-in-p” or “n-in-n” detectors; the first index (n or p) indicates the read-out electrode type and the second one the bulk type. In those examples both collect electrons, because both have n-type electrodes. However, the first one has p-type bulk while the second one has a n-type bulk. When n-type electrodes are used, it has to be taken into account that the field oxide is always positively charged and attracts electrons. A conductive layer that can connect the n-electrodes is formed, making the segmentation useless. This electron accumulation layer has to be interrupted. There are two common technologies used to avoid this effect, the so-called p-spray and p-stop. The *p-spray* technology consists of an unstructured p-implantation between n-implants and the *p-stop* which consists of the implantation of p-type barriers surrounding the n-electrodes.

Recent studies compare silicon growth processes and sensor types in a combined way. The main conclusions on the detector performance are that the more recommended options in standard planar technology are; readout on n-type electrodes in FZ processed wafers [34] and readout on p-type electrodes in MCz processed wafers [35].

The detectors in FZ processed wafers with n-type electrodes are already considered as a strong recommendation technology from RD50, but the MCz compensation is still under study and becoming a promising technology, because this kind of wafers are easier and cheaper to produce than FZ. Two graphs are included to illustrate these conclusions. Figure 1.9 shows that the sensors with n-type read-out electrodes perform better after irradiation than those with p-type read-out electrodes. The MCz (p-in-n) detectors compensation effect is shown in Figure 1.10. After a mixed irradiation, damage caused by 24 GeV protons or 300 MeV pions is compensated with damage caused by neutrons in terms of operation voltages requiring lower values than expected. In terms of charge collection the benefits are not so clear at the moment.

Diode junction layout. In terms of the junction geometry we distinguish between planar and 3D technologies. The active area is created between the opposite electrodes. In planar technologies electrodes are

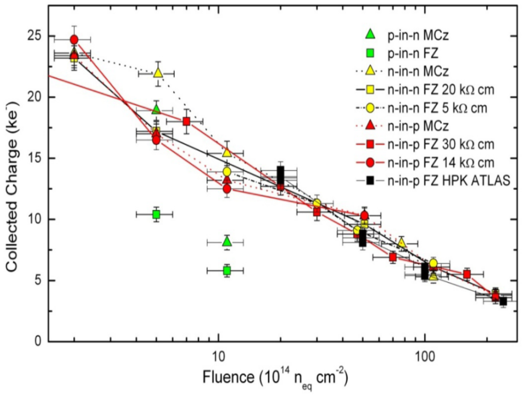

Figure 1.9: *Collected charge for proton (26MeV) irradiated samples biased at 900V. The highest collected charge is given by the detectors that include n-type electrodes. Source: [34].*

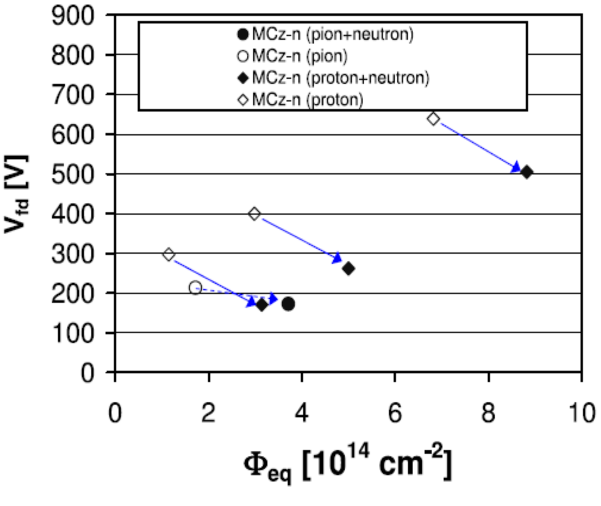

Figure 1.10: *Full depletion voltage as a function of exposure fluence. p-in-n MCz detectors show a radiation damage compensation between damages caused by charged and neutral hadrons. Source: [35].*

placed in the top and the bottom of the sensor coinciding with the sensor bulk thickness. In a 3D sensor, electrodes are columns through the silicon bulk being closer to each other. The voltage needed to fully deplete a sensor is inversely proportional to the square of the distance between electrodes. Therefore a 3D sensor can be fully depleted with lower voltages than in planar sensors. This is also an advantage in irradiated sensors because charge carries have to move shorter distances to be collected in the electrodes in a 3D sensor. Therefore carriers have lower probability to get trapped in a radiation induced defect. This makes them more radiation resistant. A detailed technology description and characterization results in irradiated 3D pixel sensors is included in chapter 5 of this thesis.

Thinned detectors. Another important requirement in tracker detectors is the material budget. This is a crucial point in every collider experiment, but particularly in linear colliders, which are high accuracy machines. To achieve the best measurements resolution it is essential to minimize the material in the experiment, minimizing multiple scattering. From the point of view of silicon sensors, the way to reduce the material is reducing the sensor thickness, but that implies a signal reduction as well. The semiconductor detectors community is working on looking for the compromise between thickness and signal in silicon sensors. This balance becomes even more important after irradiation, when the signal decreases considerably.

Summarizing this section, we can classify the sensors following these three terms; silicon growth techniques, sensor doping and diode junction layout. Nowadays, the most frequently used sensors in tracker detectors are planar devices, float zone p-on-n. Recent studies point to float zone n-on-p in planar detectors and 3D technologies for very radiation hostile scenarios. In addition 3D sensors need lower operation voltages than planar sensors. 3D pixel sensors became a present technology when they were included in the new layer of the pixel detector for ATLAS experiment, the Insertable B-Layer (IBL) [36].

In case of MCz silicon sensors, this technology is still under study, they show signs of radiation damage compensation and are cheaper than silicon grown in other techniques. There are also ongoing studies on irradiated thinned silicon sensors, but still require extremely low operation temperatures after high fluences of irradiation as described on reference [37].

1.2.2 Monolithic detectors

In a Monolithic detector, part of the readout electronic is integrated in the sensor. These detectors are based on CMOS (Complementary Metal-Oxide-Semiconductor) technologies. Three main research lines can be distinguished: DEPFET, CPS (or MAPS) and SOI detectors are remarkable and described below.

- DEPFET. DEPleted Field Effect Transistor.
  DEPFET structures were proposed in 1987 by Kemmer and Lutz [38] and incorporate a MOSFET (Metal Oxide Semiconductor Field Effect Transistor) onto a fully depleted sensor substrate. They combine radiation detection and amplification in each pixel, resulting in a very low noise and high spatial resolution device. In Figure 1.11 the working principle is shown. The inner MOSFET is used to amplify electronic signals. Thanks to these first amplification, a thinner depleted bulk can be enough to obtain a proper signal amplitude. One of the most important parameters in a DEPFET sensor is the intrinsic amplification or g_q, this parameter is defined as the ratio between the change in the transistor current ΔI_D and the charge collected in the internal gate Δq_{in}.

  Nowadays, DEPFET pixels are included in BELLE II pixel layers. In the complete qualification of DEPFET pixels made by the BELLE II collaboration [39], they obtained as working parameters a gain of $g_q \approx 400\ pA/e^-$, considering that 6000 electron-hole pairs are produced in a 75 µm silicon layer when a Minimum Ionizing Particle (MIP) traverses the sensor. The detector is operated in a gated mode continuously accumulating at the inner gate those electrons ionized by the traversing charged particle. Electrons are drained after the transistor read out. In the current design the active sensor area consumes only 0.5 W per half ladder making the low power consumption of DEPFET sensors another of their advantages.
  In terms of performance as a detector, a hit detection efficiency of 99.5%, an intrinsic resolution of 12 µm and a signal to noise ratio between 20

and 40 for MIPs (Minimum Ionizing Particle) depending on the pixel cell design was measured in test beam. Tests of radiation hardness have been also performed and DEPFET sensors show a good behavior after the particle fluences that are expected during ten years of detector life ($1.2\times 10^{13}\ n_{eq}/cm^2$). The expected dose per year is 1.85 MRad/yr. Finally the read-out time of a frame, in the case of BELLE II, takes 20 µs which is also an important parameter.The BELLE II pixel detector including DEPFET sensors is expected to be taking data in 2015.

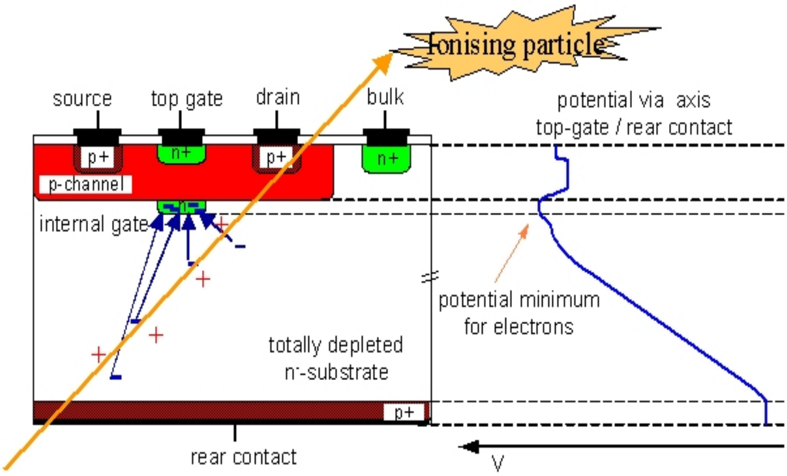

Figure 1.11: *Transverse section of a DEPFET pixel sensor and field distribution. Source: [40].*

- **CPS. CMOS Pixel Sensor.**
  CMOS pixel monolithic technologies integrate the sensor and read-out electronics into a single device. In the case of DEPFET, the integration includes only a first amplification stage into the sensor cell; in the case of CPS (also called MAPS), a complex CMOS circuit integrating analog and digital processing is implemented together with the sensor. A complete review work on this kind of technology can be found in [41] while a brief summary is here included. Figure 1.12 shows the structure of a CPS. A p-epitaxial layer acts as sensitive volume while charge is collected by diffusion in the standard N-well (n-implants). As advantages, this technology allows to decrease the pixel size (10 × 10 µm^2) reaching

very good resolution, the circuit is powered only during the read-out and the epitaxial layer used to generate the signal can be $< 20\mu$m, decreasing power consumption and material in the final detector. The main disadvantage of CPSs is that while the NMOS transistors can be in the active area, PMOS transistors need to be isolated by n-wells that can be parasitic anodes. Therefore, this limits the complexity of the integrated circuit. Other disadvantages in CPS is the low signal amplitude and radiation resistance as well as their long read out. They are used mainly in lepton or ion colliders, as is the case of STAR experiment [42].

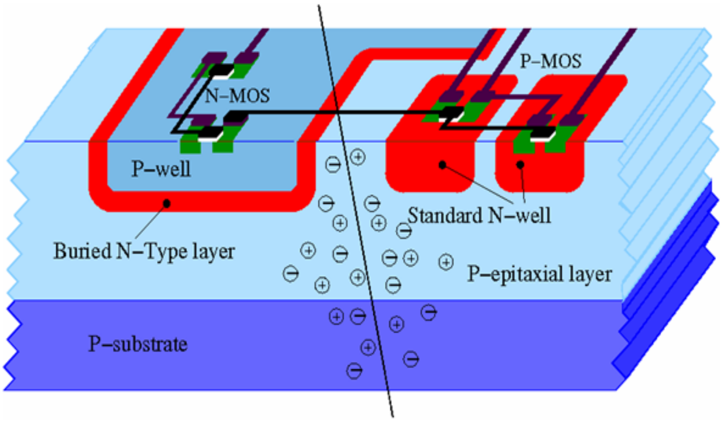

Figure 1.12: *Structure of a CMOS Pixel Sensor, CPS. Source: [43].*

- **SOI. Silicon On Insulator.**
  As in DEPFET and CPSs technologies, in SOI technologies the goal is to fabricate the sensor and its read-out electronic in the same wafer [44]. This particular process consists of connecting the CMOS wafer (read-out circuit) to a sensor wafer. The CMOS electronic is processed after the connection in a sensor wafer, which can be thinned down to tens of microns, depending on the application. Between both wafers there is an oxide layer (Buried OXide, BOX). The read-out CMOS circuit can be made of both, NMOS or PMOS transistors, which present an advantage versus the CPSs sensors. In Figure 1.13 a device section is shown. This sensors are fully depleted devices and one of the disadvantages of them is the interference between the electronic circuits and the high electric

field applied to the sensor. This problem is nowadays under study looking for some technique to insulate the circuits from the sensor wafer. Another disadvantage, and this is in common with CPSs, is that CMOS technology is limited in terms of device sizes up to a few centimeters. Their radiation resistance has also to be measured.

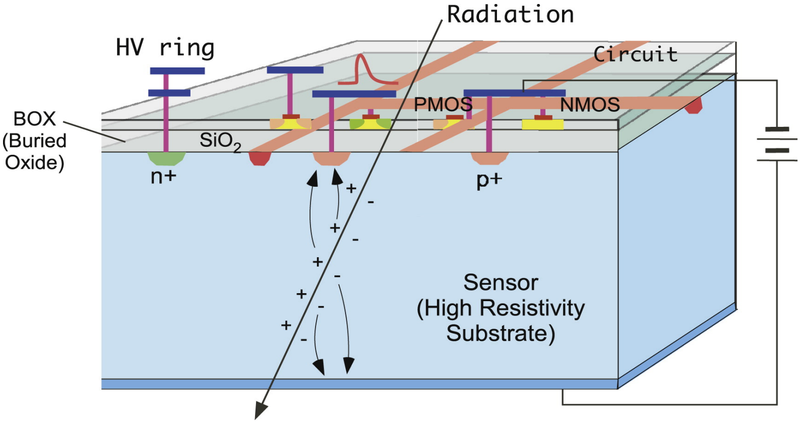

Figure 1.13: *Structure of a SOI sensor. Source: [44].*

1.2.3 High Voltage CMOS. HV-CMOS

Particle pixel detectors in standard high-voltage CMOS technology are a new detector family that allows implementation of low-cost radiation-tolerant detectors with good time resolution [45]. This technology allow to implement CMOS in pixel electronics, they are fast and radiation tolerant, HV-CMOS sensors have a good signal to noise ratio, use a standard technology in the industry that makes them accessible in the market. Figure 1.14 shows a HV CMOS sensor, we can see how the CMOS circuitry is placed inside the HV deep n-well. The inserted electronic includes the charge amplifier, shaper, comparator, DAC and RAM. They show a very high resolution ($\sim$ 4µm) and good performance up to fluence of $1 \cdot 10^{15} n_{eq}/cm^2$. The main disadvantage of this technology is the large crosstalk caused by active CMOS logic gates or comparators. One of the possibilities to avoid it is using the 3D integration technique described bellow.

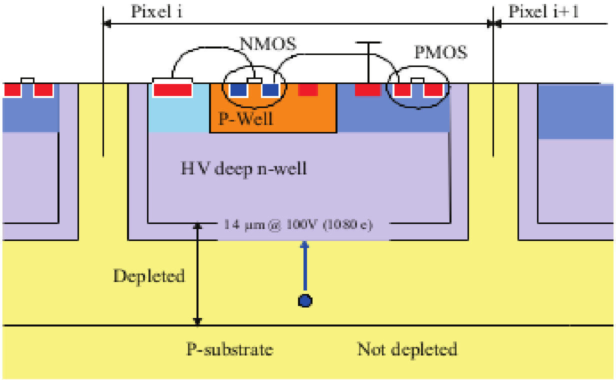

Figure 1.14: *Structure of a HV-CMOS sensor (source: [45]). The CMOS electronics is placed inside the deep n-well acting also as electrode.*

1.2.4 3D-Integration detectors

The so-called *3D-Integration detectors* is a new detector developing technique [46]. This technique consists of the direct connection of very thin silicon layers. It uses Inter-Chip Vias (ICV), which are vias through the silicon layers making vertical connections. This new technique would allow to stack up even more than two layers, giving the possibility of including sensor, analog read-out and digital control layers separating every technology in a way that they don't interfere with each other. A schema of a sensor including this technology is shown in Figure 1.15, where the three different layers are visible. There are several problems that don't allow this technology to be feasible at the moment, which are mainly technological. Manufacturers prefer to process complete wafers, but for R&D purposes this is not always possible. Some other issues are the interconnection capacitance, which is typically much higher than the pixel cell capacitance. This has relevance in its contribution to the noise. The interconnection material (high Z metals) is also important, specially in terms of radiation length.

This technology is still a non-standard technology and will require deeper studies in order to make it reliable in terms of cost and production yield.

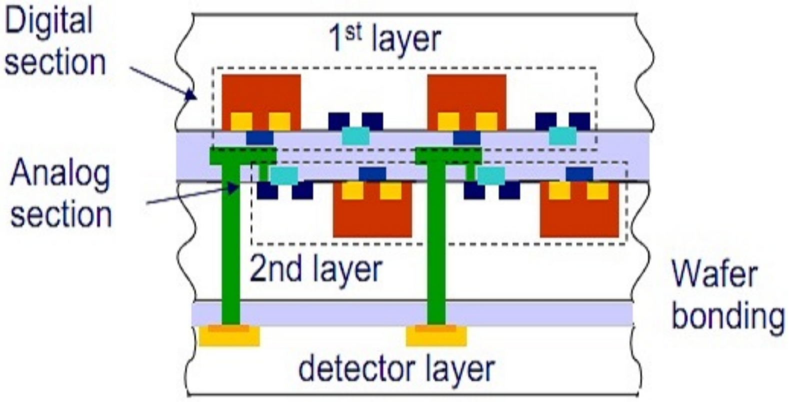

Figure 1.15: *Structure of a sensor in 3D integration technology (source: [46]).*

1.3 Microtrip and pixel sensors beyond tracking and vertexing

- **Strips technologies beyond tracking applications**

  Microstrip sensors can be applied in different areas and with different purposes. As explained before they play an important role in collider's trackers, but other strip detector applications are in beam monitoring or as alignment detectors.

  In beam monitoring, the most promising new application is in hadron-therapy. In this kind of cancer treatment, the particle beam must be monitored in real time without being degraded [47]. Silicon strip detectors in beam monitoring requires as thin as possible detector, good collection efficiency, radiation resistance and, in order to maintain the beam profile, the pitch and strip width have to be as big and small as possible, respectively.

  In alignment systems, strip sensors are used as position reference. An example of this application can be found in the CMS experiment tracker alignment system, where a network of strip sensors and a laser beam are used to know what are the real positions of the different detector parts [48]. The main requirement for alignment microstrip sensors is the transparency because a single laser beam has to go through several sensors. Actual alignment strip sensors in the CMS experiment are thin-film amorphous silicon strip sensors that provide up to 90% transmittance for red laser light combined with minimum beam distortion and a typical position resolution of 1 µm over a sensitive area of several square centimeters [49]. New studies on silicon transparent sensors have been developed [50], in this case on monocrystalline instead of amorphous silicon, and it has been shown that the sensor transmittance can be improved tunning the passivation layer thicknesses.

- **Pixel technologies beyond vertexing applications**

  All the technologies that have been described are applicable to different HEP experiments and also to other applications like electron microscopy or imaging at Free Electron Laser experiments (XFEL or SWISSFEL). In such experiments radiation conditions are not compatible with usual imaging devices, CCDs (Charge Couple Device), which are also slower in response. However, we dedicate here some paragraphs to other kinds of silicon detector technologies that are used in different applications, like image or radiation detectors.

  The most common application, outside of the HEP field for pixel technologies, is on digital image sensors. Two different technologies are dominant: CCD (Charge Couple Device) and CMOS (Complementary Metal-Oxide Semiconductor) [51]. CCDs are an array of photo-detectors (a layer of epitaxial silicon) and a shift register, analog components that need more complicated electronic circuits than CMOS sensors. CMOS sensors implement the amplifier and the analog to digital converter, they are faster in response, can be smaller in size and have lower power consumption than CCD. CMOS are the standard technology nowadays in this field.

  There are other pixel applications still in radiation detection but outside of collider tracker applications. We talk about photodetection. These detection techniques detect scintillating or Cherenkov light and an interacting medium is required. When a particle traverses a scintillating medium, it excites the medium atoms that afterwards decay to their stable status emitting scintillating light. One example of these applications is in the electromagnetic calorimeter of CMS [52], which use as scintillator material lead tungstate crystals. The scintillating light emitted is detected using either Avalanche Photo-Diodes (APDs) in the barrel or Vacuum Photo-Triodes (VPTs) in the end caps.

In the case of a particle moving at velocities higher than light speed in a medium, Cherenkov light is emitted, and a photodetector in needed to detect it. The most popular example of a Cherenkov experiment is the Super-Kamiokande experiment in Japan working on neutrino detection [53]. The target or interacting medium is water, where particles move at higher velocities than light speed in that medium, and the light detection is taking place using large area PhotoMultiplier Tubes (PMT). In photodetection, the technology is evolving to the so-called Silicon PhotoMultiplier (SiPM). A brief description of the main characteristics of these other silicon detectors (APDs and SiPM) and their main applications is given.

- APD. Avalanche PhotoDiode
  Avalanche photodiodes are very similar to p-on-n diodes but including a multiplication effect when they are operated at high voltages (400 - 2000 V, depending on the device) [54]. In Figure 1.16 a schema of an APD is shown. The APD has an extra multiplication layer adjacent to the depletion area. This multiplication layer has a very localized and high electric field in the junction. This high electric field causes that electrons drifted into it produce an avalanche or multiplication effect in the collected charge. APDs are sensitive to very low signals and unlike PMT (standard photodetectors), APDs can perform properly in magnetic fields.
- SiPM. Silicon PhotoMultiplier
  A silicon photomultiplier is a matrix of APDs operating in a geiger mode, that can have sizes between (20-100 µm) each cell. Due to their high gain (10^6), quantum efficiency (QE $\sim$ 20%), compactness, magnetic field resistance and granularity. They are becoming a promising technology in photodetection, particularly, for medical

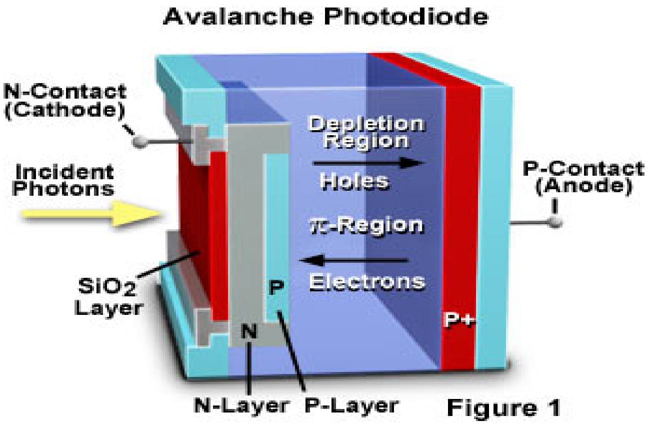

Figure 1.16: *Structure of an APD sensor, sourced from [54].*

applications [55]. For example, in Positron-Electron Tomography (PET), they detect photons coming out from the electron-positron annihilation. In order to have as much information as possible for the tumor diagnostic, light detection in medical application requires as good energy, spatial and time resolution as possible, and with SiPM instead of the standard APD (used nowadays) the position resolution can be improved, their intrinsic gain is higher and are faster in reading out. In this application, their compactness and low sensitivity to magnetic field are clear advantages too.

1.4 Summary of trends on semiconductor detectors

In general, for silicon sensors the major effort on research and development is in the material election either for the electrodes or for the bulk. The bulk material is important because n or p-type bulks behaves differently after radiation. Relative to the electrodes material, depending on the electrodes doping (resistivity), one can reach a balance between signal attenuation and noise, to increase the granularity and improve the measurement resolution.

In particular for microstrip sensors, a research line is pointing to different layout distributions and sizes of the strips, including or not pitch adapters. However, there are other novel efforts on more specific applications, like in hadron therapy, beam monitoring or alignment sensors. In beam applications, the main objective is to reduce to the minimum the sensor disturbance in the beam, while in alignment systems the purpose is to improve the optical properties in order to develop more transparent devices in a specific wavelength.

In case of hybrid pixel sensors, the effort is on thinned sensors or 3D technologies that are more radiation resistant and need lower operation voltages. The hybrid pixel sensors are used in vertexing detectors at LHC experiments. But there is a strong working line which is pointing to the total or partial integration of the electronics into the sensor itself (monolithic, HV-CMOS or 3D- integration).

Some of these technologies are already properly tested and already in use; DEPFETs are implemented in the BELLE II vertex detector and CPSs are used in ALICE or STAR experiments. More recent studies are ongoing on SOI, 3D integration techniques and HV-CMOS, all of them aim at reducing the material budget by implementing part of the electronic circuits in the device. These technologies allow to fully deplete the sensor. In case of the HV-CMOS, they are manufactured with standard electronic technology which low the cost and can be thinned easily. In case of CPS, they can include PMOS transistors but isolating them using n-wells that can act as parasitic anodes degrading the final signal in the real anodes, the sensitive layer is not depleted and the signal collection is by carriers diffusion. In case of SOI, a full CMOS circuitry can be implemented and the sensitive area is fully depleted, however the electric field affects to the electronic part requiring a stronger isolation. Some of the insulation problems that CPS, SOI or HV-CMOS present could be solved using 3D integration, but this technique is still young and in a R&D phase.

In table 1.1 a summary is presented for the different technologies in terms of; resolution, radiation fluence (tested), status of the technology, read-out speed and fully depleted volume. The numbers or estimations in there presented are illustrative. In every sensors, either strip or pixel sensors, the resolution and readout speed are not depending only in the sensor layout itself but in the readout chip as well. From ID = 1 to 7 correspond to hybrid sensors, for them, the strip or pixel pitch is limited by the interconnection techniques (wire or bump bonding). And in case of those sensors still under R & D, studies are still undergoing to test their feasibility.

ID	Technology	Resolution*	Radiation hardness	status	readout speed	fully depleted	Reference
1	Planar strips p-on-n	pitch/$\sqrt{12}$	$1\cdot 10^{14} n_{eq}/cm^2$	LHC outer trackers	$\sim ns$	yes	[56]
2	Planar strips n-on-p	pitch/$\sqrt{12}$	$1\cdot 10^{15} n_{eq}/cm^2$	R & D (HL-LHC)	$\sim ns$	yes	[57]
3	Resistive strips	pitch/$\sqrt{12}$ $\frac{\Delta l}{l} \approx 2.35\frac{N}{S}$ [58]	—	R & D (ILC)	$\sim ns$	yes	[13,59,60]
4	Thin strip detectors up to 75 µm	pitch/$\sqrt{12}$	$2\cdot 10^{16} n_{eq}/cm^2$	R & D (HL-LHC)	$\sim ns$	yes	[10]
5	Planar pixels n-on-n	size/$\sqrt{12}$	$1\cdot 10^{15} n_{eq}/cm^2$	LHC inner trackers	$\sim ns$	yes	[61]
6	Planar pixels n-on-p	size/$\sqrt{12}$	$1\cdot 10^{16} n_{eq}/cm^2$	R & D (HL-LHC)	$\sim ns$	yes	[62]
7	3D pixels	size/$\sqrt{12}$	$2\cdot 10^{16} n_{eq}/cm^2$	ATLAS IBL and HL-LHC	$\sim ns$	yes	[36]
8	Thin pixel sensors	size/$\sqrt{12}$	$2\cdot 10^{16} n_{eq}/cm^2$	R & D (HL-LHC)	$\sim ns$	yes	[37]
9	DEPFET	size/$\sqrt{12}$	$1.2\cdot 10^{13} n_{eq}/cm^2$	BELLE II	$\sim$ µs	yes	[39]
10	CPS	size/ $\sqrt{12}$	$1\cdot 10^{13} n_{eq}/cm^2$	R & D (STAR)	$\sim$ µs	no	[63]
11	SOI	size/ $\sqrt{12}$	$1\cdot 10^{15} p/cm^2$	R & D	$\sim$ µs	yes	[64]
12	HV-CMOS	size/ $\sqrt{12}$	$1\cdot 10^{15} n_{eq}/cm^2$	R & D	$\sim$ µs	no	[65]

Table 1.1: *State of the art table, see text for details.*
Devices 9,10,11 and 12 belong to CMOS technology and they can have smaller pixel sizes (between 14 and 40 µm).
* *One-pixel clusters, normal incidence.*

Chapter 2

Physics of silicon detectors

There are two different perspectives to study a silicon detector, micro and macroscopic. To understand properly the macroscopic behavior it is necessary to understand first what is happening in the microscopic scale. Microscopically, a silicon sensor is studied in solid state physics as any semiconductor material. Macroscopically, the sensor is considered as a diode from which a signal is obtained and interpreted as the sensor response to an ionizing particle or radiation that goes through it. In this chapter both perspectives are reviewed in order to set the basis for the complete understanding of this document, as well as the basics of the signal processing. Finally a specific section on radiation damage in silicon and its consequences on the detector performance are included .

The information, except specific references, that has been used to write this chapter has been extracted from several well known textbooks on silicon devices. These books are: H. Spieler [66], G.F. Knoll [67] and G. Lutz [68]. To complete the section on radiation damage, additional references apart from those already cited have been used. These are three different thesis: Michael Moll [69], Gregor Kramberger [70] and Nicola Pacifico [71]. These works study in detail the radiation damage in silicon detectors in the highly hostile collider experiment environments.

2.1 Semiconductor detectors. Silicon

To understand what is a semiconductor, it is necessary to know that the energy levels allowed for the electrons in a crystalline material are structured in bands and defined by the periodic lattice of the material. The energy of any of the electrons has to be confined to one of these energy bands and they are separated by gaps or ranges of forbidden energies. There are two distinguished bands *valence band* and *conduction band.* The valence band is the energy band corresponding to electrons bounded to specific nucleus of the lattice's atoms and to the conduction band belong the free electrons that are able to migrate through the crystal. Electrons in the conduction band contribute to the electrical conductivity of the material.

Valence and conductivity bands are next each other but separated by a band gap. The size of the band gap determines if the material is an insulator, semiconductor or conductor. The main difference between conductors, semiconductors and insulators is the energy gap between the valence and conduction bands, being $E_g = 0\ eV$ in conductors (valence and conduction band overlap), $E_g \cong 1\ eV$ in semiconductors and $E_g > 5\ eV$ in insulators.

In a thermal equilibrium situation, electrons fully fill the valence band and the conduction band is empty. In this equilibrium, both semiconductor and insulator will not show any electrical conductivity. When the electrons have enough energy to pass the gap and reach the conduction band, they become free to move in the crystal leaving a vacancy in the valence band called *hole.*

Crystalline silicon is a semiconductor, and in the next sections a deeper description of its behavior as a detector is given as well as an explanation of how silicon can become a radiation detector.

2.1.1 Doping

The crystalline silicon used in detectors is a semiconductor that has almost no impurities in the material therefore it has only the few electrons, generated by thermal excitation, in the conduction band (holes in the valence band) and it is not conductive. In silicon detectors the purity is altered intentionally in order to manipulate the silicon electric properties. This process, that can be done during the silicon growth or later in selected areas in the crystal, is called *doping.* We talk either about *n-type* or *p-type* silicon when an excess of electrons in the conduction band is added to the crystal silicon or when the added excess is of holes into the valence band, respectively. The dopants can be classified as *donors* or *acceptors*, if they include free electrons or holes in the lattice that contributes to the material conductivity. The elements that are used as dopants are from groups V or III (typically Phosphorus or Boron), because they have five or three electrons in their outer shell, while silicon has four electrons. In this way, the number of majority carriers increases (electrons in n-type and holes in p-type silicon) and the amount of minority carriers decreases, causing a displacement of the Fermi level towards the conduction band (n-type) or to the valence band (p-type), see equations 2.1. The density of carriers -n or p- depends on the intrinsic density -n_i- (undoped silicon), and on the deviation of the Fermi level -E_F- from its value in the undoped silicon E_i.

$$n = n_i e^{\frac{E_F - E_i}{kT}} \qquad\qquad p = n_i e^{\frac{E_i - E_F}{kT}} \tag{2.1}$$

In thermal equilibrium, semiconductors are electrically neutral bodies. Movable carriers are electrons in the conduction band and holes in the valence band. They can move either by diffusion (inhomogeneous distribution of carriers) or by drift (applying an external voltage).

By diffusion, the carriers flux (Φ_n) is due to the gradient of the carrier density as:

$$\Phi_n = -D_n \nabla n \qquad\qquad \Phi_p = -D_p \nabla p \tag{2.2}$$

The diffusion factor D is related to the mobility factor μ by the Einstein relation following:

$$D = \frac{kT}{q}\mu \tag{2.3}$$

Free electrons and holes can be generated in silicon by three different processes. These processes move electrons from the valence to the conduction band generating electron-hole pairs in the sensor's bulk, namely:

- Thermal generation. The thermal pairs generation is unavoidable, and it occurs when the energy gap between valence and conduction bands is small enough compared with the thermal voltage at room temperature $\frac{kT}{q} = 0.0259\ V$.

- Electromagnetic Radiation. In this case a photon is absorbed and its energy is transfered to a valence band electron, promoting it into the conduction band leaving a hole in the valence band.

- Charged particles. This is the case of interest for tracking and vertexing applications. Charged particles lose part of their energy traversing a material due mostly to interactions with material electrons. The loss of energy by length unit can be quantified by using the *Bethe-Bloch Formula*. This formula has been developed first by Bohr (classical) and later improved by Bethe - 1930, Bloch - 1933 and Landau - 1944 taking into account the quantum corrections, and is shown in Equation 2.4. Energy loss per unit length depends on the material (Z, A and ρ are atomic number, atomic weight and density of the medium), the particle nature and energy (z is the charge, β and γ are related to the velocity of the particle), the effective ionization potential I , the maximum energy transfer in a single collision W_{max} and correction factors δ and C. In a semiconductor sample with a finite thickness, the average energy lost by a charged particle can be calculated from the Bethe-Bloch formula by integration.

$$\frac{dE}{dx} = constant \cdot \rho \frac{Z}{A} \frac{z^2}{\beta^2} [ln(\frac{2m_e \gamma^2 v^2 W_{max}}{I^2}) - 2\beta^2 - \delta - 2\frac{C}{Z}] \tag{2.4}$$

2.1.2 PN-Junction

A pn-junction (also called rectifying junction) is formed when p-type and n-type silicon are connected (see Figure 2.1). Both silicon types are considered separately, with a homogeneous distribution of carriers (in a thermal equilibrium). When they are in contact, the gradient of electron and hole densities causes a diffusion of the carriers along the junction, recombining themselves until the charge difference between both material creates an electric field strong enough to block the diffusion. This electric field is created because now part of the p-type silicon has a net negative charge and the opposite occurs to the n-type silicon, forming the so-called *p-n junction* in which a space charge (SCR) or depletion area is created. In this area, the carriers concentration is much smaller ($\sim$ 100 carriers/cm^3) than in p or n-type silicon (10^{10} carriers/cm^3).

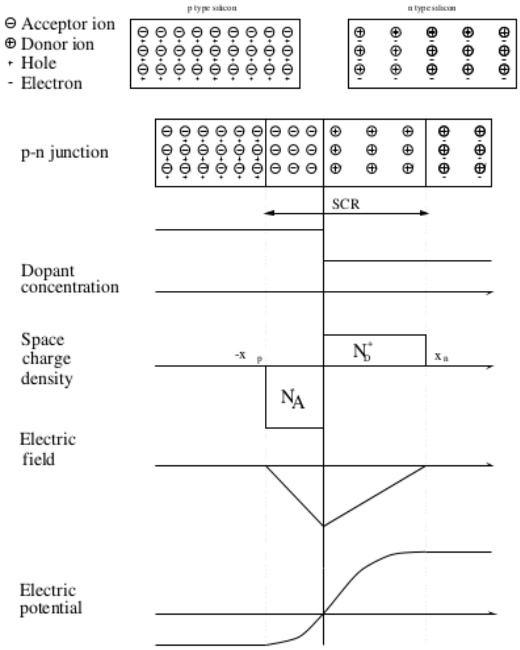

Figure 2.1: *The p-n junction description: initial state, p-n junction, dopant concentration, charge density (N_A and N_D are numbers of acceptors and donors respectively. X_p and X_n are the depleted area limits in p and n-type silicon respectively), electric field and potential along the union (source: [70].)*

If the concentration of donors and acceptors are similar in p and n areas, the depleted region extends equal distances into both sides of the union.

When the junction is created and in static equilibrium. We can apply the Poisson equation in order to determine the electrical properties in the junction:

$$-\frac{d^2V}{dx^2} = \frac{\rho_e(x)}{\epsilon_{Si}\epsilon_0} \tag{2.5}$$

The charge density, assuming sharp transitions between SCR and bulk, is given by:

$$\rho_e(x) = \begin{cases} e_0 N_D & \text{if } X_n > x > 0 \\ e_0 N_A & \text{if } -X_p < x < 0 \end{cases} \tag{2.6}$$

Resulting in the electric field and potential shown in Figure 2.1. The potential difference over the depleted area without an external bias is called the built-in potential V_{bi} and is given by:

$$V_{bi} = \frac{e_0}{2\epsilon_{Si}\epsilon_0}(N_D X_n^2 + N_A X_p^2) \tag{2.7}$$

Applying electrical neutrality:

$$N_A X_p = N_D X_n \tag{2.8}$$

The effective carrier density $N_{eff} = N_D - N_A$ is used as variable and the depleted region is written as follows:

$$W = \sqrt{\frac{2\epsilon_{Si}\epsilon_0}{e_0} \frac{V_{bi}}{|N_{eff}|}} \tag{2.9}$$

Typically the value for V_{bi} is between 0.5 and 1 Volt and the depletion region in an unbiased junction will be around few tens of micrometers. In a real HEP detector, one of the sides in the junction is much more doped than the other. In this case, the depletion region length is much larger in the lower doped side, the highly doped region length becomes negligible (according with equation 2.8) and we can consider that the depletion region is $W = X_p + X_n \approx X_{p,n}$.

2.1.3 Principle of operation

When an ionizing particle traverses the depleted region it creates electron-hole (e-h) pairs, which are separated by the electric field, collected and readout. Increasing the depleted area, the number of created e-h pairs and therefore the collected charge increases accordingly. To increase the depleted area, an external voltage V_{bias} with the same built-in polarity is applied. Typically $V_{bias} >> V_{bi}$, therefore $V_{total} = V_{bias} + V_{bi} \approx V_{bias}$. Including the external voltage in equation 2.9, the depletion region is now proportional to the square root of the external voltage as follows:

$$W(V_{bias}) = \sqrt{\frac{2\epsilon_{Si}\epsilon_0}{e_0 \cdot |N_{eff}|} V_{bias}} \tag{2.10}$$

The total voltage necessary to fully deplete a detector is called the full depletion voltage (V_{FD}). In this thesis D is defined as the distance between the detector electrodes with different doping type (also named as pn-junction and ohmic contact); in planar sensors V_{FD} is given by:

$$V_{FD} = \frac{e_0 N_{eff} D^2}{2\epsilon_{si}\epsilon_0}(\propto D^2) \tag{2.11}$$

The full depletion voltage therefore depends linearly on the effective carriers density and quadratically on the distance between electrodes.

A depleted region between electrodes can be considered as a capacitor, where electrodes act as anode and cathode and the depleted region as dielectric. A capacitance per unit area is associated to the depleted region and is given by equation 2.12.

$$\frac{C}{A} = \frac{\epsilon_0 \epsilon_{Si}}{W} = \begin{cases} \sqrt{\frac{e\epsilon_0\epsilon_{Si}|N_{eff}|}{2V_{bias}}} & \text{if } V_{bias} < V_{FD} \\ \frac{\epsilon_0\epsilon_{Si}}{D} & \text{if } V_{bias} \geqslant V_{FD} \end{cases} \tag{2.12}$$

Because of practical reasons, the most used magnitude is $\frac{1}{C^2}$, so we can establish a proportionality relation with V_{FD} as follows:

$$\frac{1}{C^2} \propto \begin{cases} V_{bias} & \text{if } V_{bias} < V_{FD} \\ D^2 & \text{if } V_{bias} \geqslant V_{FD} \end{cases} \tag{2.13}$$

Following this relation, the full depletion voltage can be measured in the laboratory, measuring the capacitance evolution as a function of the applied voltage. Measuring $\frac{1}{C^2}$, a linear behavior is observed initially proportional to V_{bias} that will reach a saturation o constant value proportional to the square of the distance between electrodes. The procedure to experimentally obtain V_{FD} is explained in detail in chapter 3.

2.1.4 Basic structures

The simplest detector is a diode, and it requires a pn-junction and an ohmic contact. The junction is necessary to create a depleted region and the ohmic contact is necessary to apply properly the bias voltage, otherwise a Schottky contact will be created. In Figure 2.2 an example of a p-in-n diode structure

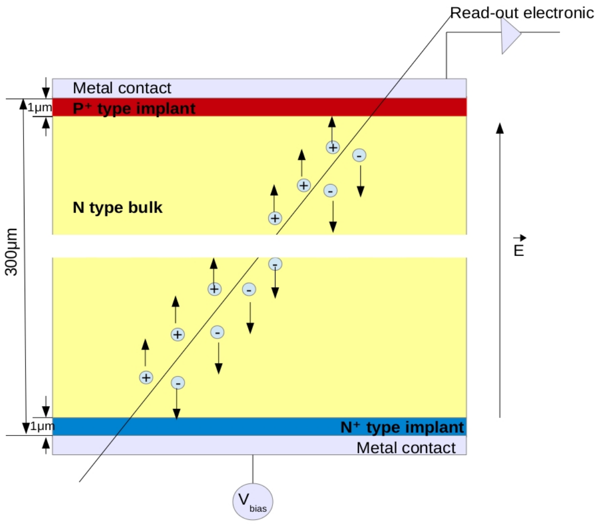

Figure 2.2: *Structure of a diode p-on-n type. The pn-junction is on the top while the ohmic junction is at the bottom of the device.*

is shown (the sign + indicates highly doped silicon). In this case, the p-n junction is on the top of the device, and the ohmic one is at the bottom. They are also called rectifying and non-rectifying junction respectively. When an ionizing particle traverse the device (depleted or active region), pairs of electrons-holes are created. The amount of them is directly proportional to the deposited energy on the crystal following the Bethe-Bloch formula (equation 2.4). According to reference [72] the Most Probable Value (MPV) on average for a charge distribution in silicon is 76 electrons per micrometer and the mean value is 108 $e^-/\mu m$. In a 300 µm thick sensor the expected values are 22800 e^- and 32400 e^-, respectively. The free charge carriers drift in the device due to the field created by the bias voltage applied until they are collected in the respective electrodes. In Figure 2.2 we can exchange p+ and n+ type. Then, to keep the junction in the top of the device, we have to exchange the bulk to a p-type bulk, having instead of a p-in-n a n-in-p device. This nomenclature indicates ”readout electrode-in-bulk type”. Sometimes in the literature we can also find, n-in-n devices. In this case, the readout electronic collects electrons (through the n-type readout electrode) in a sensor with a n-type bulk, the junction in this device is at the bottom, and the signal is readout at the ohmic contact.

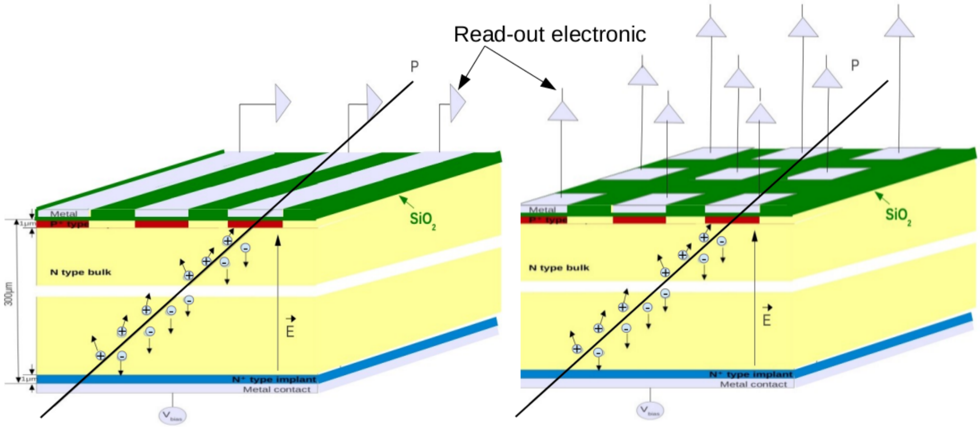

Figure 2.3: *Structure of p-on-n type segmented detectors. Left: microstrip detector, the diode structure is segmented in strips of tens of microns width. Right: Pixel detector, the diode is segmented in squares of hundred microns side approximately.*

Having as primary structure the diode and considering the possibility of segmentation of the p+ collection electrode, a higher position sensitivity can be reached. There are two main segmentation patterns in use nowadays, into strips or into squares. A schema of both structures is shown in Figure 2.3 and as it has been explained in the previous chapter, both have different applications depending on their performance and specific characteristics. The size of the strips and pixels are now reaching widths below 20 µm for strips and 100 µm for pixels. They act as small diodes either with a strip form in microstrip detectors or with a square or rectangular form in the case of pixel detectors.

2.1.5 3D detectors

Two different types of technologies can be distinguished; the more standard one is the so-called *planar technology* that uses simpler fabrication techniques and the distance between electrodes is determined by the device thickness. Combination of planar and Micro Electric Mechanical Systems (MEMS) technology allows to manufacture vertical electrodes. These characterize the so-called *3D-technology* fabrication techniques where electrodes are columns inside the bulk and they can be closer to each other. This new structure was

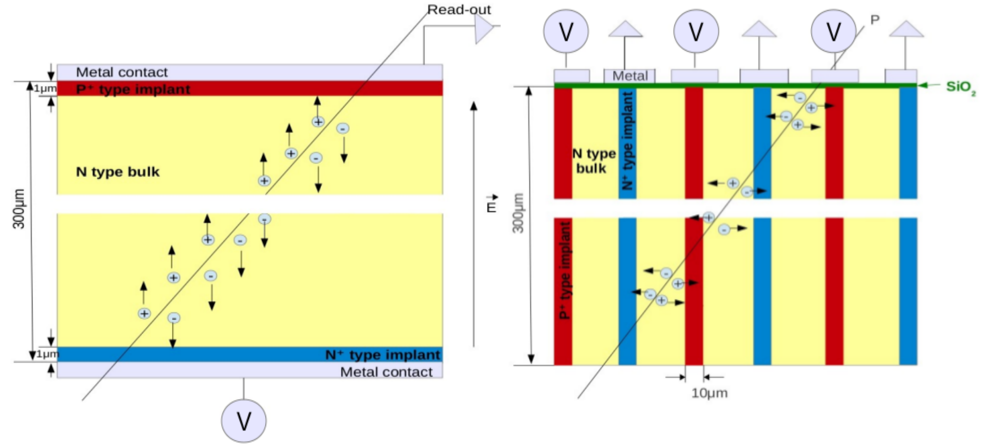

Figure 2.4: *Basic structure of p-on-n type sensor. Left: Planar technology. Right: 3D technology.*

proposed by S. Parker in 1997 [73].

A 3D detector has exactly the same working principle as planar detectors, but instead of a single pn-junction and ohmic junction, there are several of them, with a dielectric or depleted region in between. The structure diagrams are shown in Figure 2.4, where you can see these differences.

In 3D technologies, thanks to the fact that electrodes are closer to each other, the necessary voltage to fully deplete the device is smaller. However, to calculate V_{FD} the planar equation (equation 2.11) is not longer applicable in this kind of structure. A better approximation is the coaxial formula already proposed with this objective in [74]. Applying the equation 2.14, the depletion voltage depends on the distance D (now $\sim 80-90$µm), and on r which is the column radius ($\sim$ 10µm).

For a standard planar sensor with a thickness of about $\sim$ 300µm, the typical V_{FD} is about 100 V, becoming V_{FD} about 10 V in a 3D sensor with the same thickness and N$_{eff}$. This aspect becomes crucial in irradiated samples where the voltage needed to deplete the device increases considerably as will be shown later in this chapter.

$$V_{FD} = \frac{qN_{eff}}{2\epsilon_0\epsilon_{Si}}\left(D^2\left[ln(\frac{D}{r} - 0.5)\right] + 0.5r^2\right) \tag{2.14}$$

As it has been mentioned, differences between planar and 3D technologies are in the junction layout of the detector. The 3D sensors can therefore be segmented in the same way as planar sensors. In 3D-pixel detectors, we will read out n or p-columns and in 3D-strip detectors, all the aligned columns (n or p-type) are shorted together forming strips.

In this thesis, a full chapter is dedicated to 3D pixel detectors including a detailed description of the technology and showing characterization results and performance before and after irradiation.

2.2 Signal formation

Silicon detectors act as ionization chambers. When a particle crosses the depleted volume, it deposits energy that produces *electron-hole pairs*, negative and positive charge carriers. Helped by an electric field created with an external bias voltage, carriers move and induce a current (charge change) on the electrodes.

2.2.1 Ramo's Theorem

To understand the signal formation in semiconductors we have to look back into Ramo's Theorem already formulated in 1939 [75]. The theorem is summarized in equation 2.15, where i is the induced current in a given electrode due to a single electron's motion, $r(t)$ is its instantaneous position at time t, e is the charge of the electron, v is the instantaneous velocity and the weighting field E_w is the electric field component in the v-direction.

This E_w is the electric field that would exist at the electron position when the electron is removed and the electrode is set to $1V$ potential and all other conductors are grounded.

$$i(r(t)) = E_w(r(t)) \cdot e \cdot v(t) \tag{2.15}$$

In a silicon detector, carriers are holes and electrons, therefore equation 2.15 can be applied also to holes. The differences are in the charge sign and in the velocity, because the mobility of the carrier depends on its nature:

$$v_{e,h} = \mu_{e,h} \cdot E \tag{2.16}$$

Electrons and holes have different mobilities (approximately $\mu_e \approx 3 \cdot \mu_h$). A higher mobility can be an advantage in irradiated samples, one of the reasons why trends in silicon detectors are pointing to collect electrons instead of holes.

When a particle or ionizing radiation crosses the depleted volume of the detector, electron-holes pairs are created in a number proportional to the particle energy deposition in the detector. The carriers drift in the device thanks to the bias voltage and induce a current (following equation 2.15) into the electrodes. The signal generation ends when the charge is collected.

The collection time depends on the carrier velocity which is proportional to the mobility and the electric field. In the same conditions collection times are related as $t_{c,h} \approx 3 \cdot t_{c,e}$. The collection time can be reduced increasing the bias voltage, but it is limited by the "breakdown" voltage that occurs when electrons acquire enough energy to form secondary pairs resulting in an avalanche behavior. Another way to reduce the collection time is reducing the electrode distance, something which is naturally reached by design in 3D technologies keeping the same detector volume. In planar technologies, to reduce electrodes distance implies a detector volume reduction.

Once the detector technology and geometry are fixed, the signal will depend on the ionizing radiation or particle nature. In case of photons, it will depend on their energy, that has to be higher than the bandgap in silicon (1.12 eV) to generate an electron-hole pair for single photon absorption processes. In case of a charged particle, the deposited energy follows the Bethe-Bloch formula 2.4.

2.2.2 Signal processing

Concerning the signal processing, when ionizing radiation or particle traverse the detector it deposits energy creating electron-hole pairs that move to the electrodes. The resulting electrical signal is integrated in a charge-sensitive preamplifier, shaped and digitized for storage and analysis. These are the basic stages in a detector (see Figure 2.5).

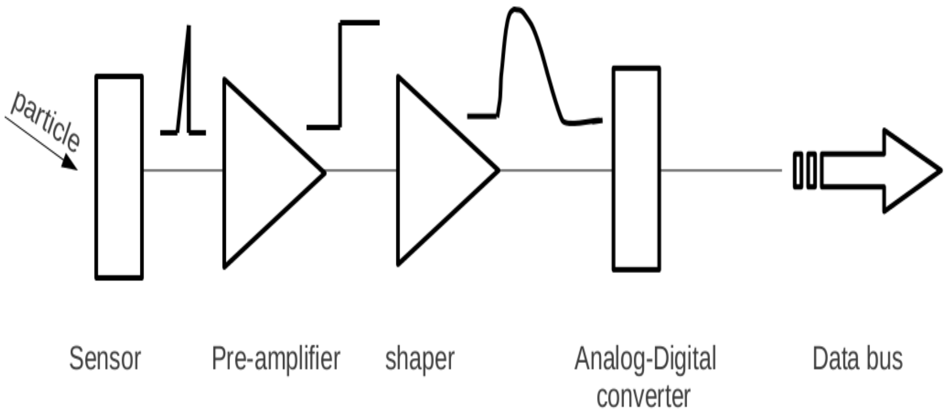

Figure 2.5: *Block diagram of the different detector stages before the signal processing: sensor, preamplifier, shaper and digitizer.*

Integrating the generated current by the carriers movement, the signal charge is obtained and it is proportional to the particle energy. The signal charge is $\sim 4 \cdot 10^{-15}$C in a typical high-energy tracking detector and needs to be amplified. Amplifying the signal, the noise is amplified as well. Therefore the electronic components have to be designed carefully, as we will see later.

The output of the sensor is time dependent. A shaper applies filters that benefit the signal, attenuating the noise. The pulse shape is affected also by this filter increasing the pulse duration and reducing the bandwidth. If pulses become too long in time and if several pulses at a high rate are given, the pile-up of successive pulses is possible.

A more detailed description of the signal processing components is shown in Figure 2.6. The preamplifier receives the current from the detector $i(t)$ and it gives as output a voltage $V_{out} = \frac{Q_i}{C_f}$ (step function output) with a decay time $\tau_f = R_f C_f$. The shaper has two different parts (in its simplest configuration, a CR-RC circuit), a high-pass filter or differentiator that limits the pulse width adding a decay time τ_d and a low-pass filter or integrator (with a time constant τ_i), that increases the rise time and limits the bandwidth to form the final pulse shape. The high frequency bound sets the rise time, while the low frequency determines the pulse duration. Usually a compromise between reducing noise (smaller bandwidth) and speed (shaping time) is required to

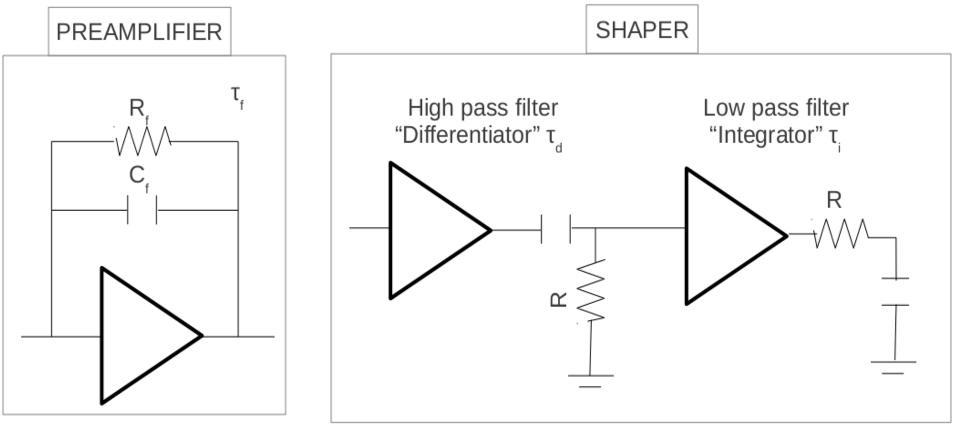

Figure 2.6: *Electronic components in the preamplifier and shaper.*

optimize the detector performance.

The output signal after the shaper is affected by all the electronics components (see equation 2.17)

$$V_{out} = \frac{Q_i}{Q_f} \frac{\tau_d}{\tau_d - \tau_i}[e^{-t/\tau_d} - e^{-t/\tau_i}] \tag{2.17}$$

If $\tau_d = \tau_i = \tau$, the following equation will be a good approximation:

$$V_{out}(t) = \frac{Q_i}{C_f} \frac{t}{\tau} e^{-t/\tau} \tag{2.18}$$

The output pulse will have its maximum at the peaking time $t_p = \tau$.

2.2.3 Noise contributions

Electric signal processing aims to suppress the electronic noise while preserving the signal. To evaluate the noise, its origin has to be identified and understood. In this section general contributions are studied, however in a practical case, a specific study has to be performed taking into account every component in the read out chain as well as the particular sensor characteristics.

In detectors where the position information becomes crucial, the position resolution is determined by the signal-to-noise ratio and decreasing the noise is a critical point to improve the detector resolution.

Considering Ramo's Theorem, a current flowing or induced signal in the simplest configuration (planar diode) is $i = \frac{nev}{d}$ where n is the number of carriers, e the electric charge, v the carrier velocity and d the distance between electrodes. The fluctuation of this current gives two noise contributions (see equation 2.19), from the number of carriers and from their velocity fluctuations.

$$\langle di\rangle^2 = (\frac{ne}{d}\langle dv\rangle)^2 + (\frac{ev}{d}\langle dn\rangle)^2 \tag{2.19}$$

In systems whit a detector response depending on the frequency *(f)*, the noise spectral distribution is needed and it is described as a power density dP_n/df. To understand its influence in the electronic, the noise spectral distribution is written in terms of current and voltage spectral distributions, $i_n \equiv \frac{di_n}{df}$ and $e_n \equiv \frac{dv_n}{df}$ respectively. Integrating the noise power over the interest frequency range, the total noise is obtained ($(di_n)^2 = i_n^2 \cdot (df)^2$).

Noises are interpreted as the manifestation of microscopic random processes. Electronic noises can be classified in terms of their sources and three of them are always present in electronic components: thermal, low-frequency and shot noise.

Thermal noise.
This noise is due to thermal fluctuations of the carriers, that changes the carriers velocity randomly. It is associated to resistors and even without any applied voltage a noise can be measured between the two terminals. It has a constant contribution to the noise spectral density (white noise). Applying thermodynamic laws the current spectral density of this noise is given by equation 2.20, where k is the *Boltzmann constant*, T the absolute temperature and R the resistance of the component.

$$i_n^2 = \frac{4kT}{R} \tag{2.20}$$

Low-frequency noise.
This type of noise is present in most of the electronic components and has a dependence inversely proportional to the frequency (see equation 2.21). It has a relevant roll in transistors and is caused by crystal defects that trap carriers. Carriers are trapped and then released with a time constant τ which gives to

this phenomenon a frequency dependence as follows.

$$i_n^2 \propto \frac{1}{f} \tag{2.21}$$

Shot noise.
Shot noise is a consequence of the carriers charge discreteness and it generates time dependent fluctuations in the current. This noise is present in thermo-ionic or semiconductor diodes but it is not in ohmic conductors where $I = V/R$, this is because any fluctuation in electron density relative to the stationary positive vacancy will set up an electric field that will easily balance the fluctuation.

The spectral density of the current fluctuations is given by equation 2.22, where I is the average current and e the electric charge.

$$i_n^2 = 2eI \tag{2.22}$$

Any noise before the amplifying chain (preamplifier and shaper) will be amplified with the signal. Therefore, every noise sourced after this chain can be neglected, because it is much smaller than the amplified noises. Noise comes mostly from the sensor leakage current (I_{leak}), resistors (bias R_b and those resistors in series to the preamplifier input R_s) and the input transistor of the preamplifier. In general, the sensor leakage current will contribute with *shot noise*, resistors with *thermal noise* and the input transistor contributes with two components, one due to the current (I_a) and one due to the frequency response of the amplifier (A(f)), shot and low-frequency noise respectively.

The magnitude of the charge Q_n which injected in the detector volume would produce the same signal as the one read without a particle traversing the sensor is called Equivalent Noise Charge (ENC). The total noise of a detector system measured as ENC at the input of the amplifier is given by equation 2.23, adding noises due to the leakage current ENC_i, parallel resistors as thermal noise ENC_{th}, resistors in series in the circuit ENC_S and the noise due to the preamplifier frequency response ENC_{pa}.

$$ENC_{tot}^2 = ENC_i^2 + ENC_{th}^2 + ENC_S^2 + ENC_{pa}^2 \tag{2.23}$$

Looking at the ECN dependencies in equation 2.24 we see a relevant roll of the total capacitance C at the input of the preamplifier. This capacitance is mostly the detector capacitance. On the other hand, the ENC depends on the signal peaking time τ as well, but in such a way that a compromise between different noise sources must be made. A high peaking time increases the leakage current contribution to the noise but decreases the one due to serial resistors. The optimal peaking time will be the one that equalizes both terms. Regarding the detector and its characteristics, one should reduce their leakage current, the series resistance and the total capacitance and increase the bias resistor resistance.

$$\begin{aligned} ENC_i^2 &\propto I_{leak,a} \cdot \tau \quad ; \qquad ENC_{th}^2 \propto \frac{T \cdot \tau}{R_b} \\ ENC_S^2 &\propto \frac{C^2 \cdot R_s}{\tau} \quad ; \qquad ENC_{pa}^2 \propto A(f) \cdot C^2 \end{aligned} \tag{2.24}$$

The detector capacitance is inversely proportional to the distance between electrodes. In a planar diode, it is determined by the sensor thickness, but in segmented detectors the total capacitance is higher because the dominant capacitance is the interstrip or interpixel capacitance for strip or pixel detectors because usually the pitch is smaller then the sensor thickness. In the case of the 3D sensors, the interstrip capacitance and the inter-electrodes capacitance are in the same order.

In order to keep an acceptable S/N ratio, these inter-capacitances have to be as low as possible, therefore sensors can not have very small pitches between electrodes. On the other hand the spatial resolution in a segmented sensor depends also on the pitch as $\sigma = \frac{p}{\sqrt{12}}$ (in binary approximation). In silicon position-sensitive detectors a balance between S/N ratio and resolution has to be achieved, finding the optimal distance between electrodes or pitch.

2.2.4 Ballistic deficit

It has been shown in the previous section that the peaking time influences the noise significantly. Theoretically, the output from the front-end should be sampled at the maximum amplitude or peak. In Figure 2.5 we saw that the preamplifier transforms the detector answer into a step function (rise time zero), and then the shaper changes its rising and decay time depending on the time constant of the internal CR-RC circuit. The phase between the sampling clock (read out chip) and the bunch crossing clock (particle hit on the detector) depends on different parameters, such as the distance to the collision point (in a collider, time of flight) and also on the shape of the induced current. This induced current shape changes with the applied voltage, hit position on the detector and the spatial resolution. To sample the pulse in the correct τ_{peak}, each event should be sampled independently. In practice most beneficial sampling time is chosen for each detector maximizing the Charge Collection Efficiency (CCE). This sampling time τ_s is not equal to the real peaking time τ_p.

In case of the induced current extending over the time (pulse rise time comparable with the real peaking time), the fact of having a sampling time smaller than τ_p and the corresponding loss of the measured charge is known as *ballistic deficit*. As a consequence of the ballistic deficit, the collected charge decreases and the peaking time shifts to higher values for current pulses of longer duration.

In standard detectors, the time constant of their electronic circuit is under control and should be well known. In this thesis, a work with strip sensors with resistive electrodes is included, where the influence of the electrode resistance has to be considered, affecting the signal amplitude (attenuation) and pulse rise time (increment). These effects will be studied in detail in Chapter 4.

2.3 Radiation damage in Silicon

In this thesis, the characterization of 3D pixel sensors for the CMS upgrade is presented in Chapter 5. Pixel detectors are usually placed in the innermost layer of a HEP detector in colliders. In the case of CMS, the innermost layer will support a radiation dose is about $1 \cdot 10^{16} n_{eq}/cm^2$. In this section, an overview of the radiation damage in silicon and its effects is given, as well as a description of the detector performance and characteristics after irradiation.

The purity of the silicon wafer and its processing determine the concentration and nature of crystalline defects in the resulting sensor bulk. Crystalline defects introduce new energy levels within the silicon energy band structure.

When a defect is localized in a forbidden band gap, the electrical characteristics of the bulk change. A defect can act as a dopant when it is very close to one of the bands or as an electron-hole generation center when it is very deep in the bandgap. In both cases, it will increase the leakage current of the sensor.

A *Frenkel Pair* is formed in case of an inelastic collision between a highly energetic particle and one of the lattice atoms. The atom can be displaced to a non periodical position in the lattice. This defect is called *interstitial defect* while the empty space is called *vacancy*. The first collision between the radiation and an atom takes the name of *Primary Knock on Atom* (PKA). The minimum necessary energy to form a Frenkel Pair (or PKA) in silicon is 25 keV. If the atom itself absorbs enough energy, it can release energy while moving in the bulk, by ionization and by nuclear collisions generating more *displacement damage* and creating *clusters of defects*.

Frenkel Pairs have a high mobility at room temperature. When the density of pairs is high, they can interact with each other forming defect complexes, constituting impurities in silicon (wanted or accidental impurities). These impurities have different charge states that contribute to the bulk characteristics.

A model developed within the ROSE collaboration [76] quantifies the radiation-induced damage in silicon sensors. The model is called *Non Ionizing Energy Loss (NIEL)* model. The NIEL model allows to predict the change in some macroscopic silicon characteristics due to the radiation damage.

2.3.1 The NIEL hypothesis

The NIEL hypothesis assumes that the bulk radiation damage produced by ionizing radiation is proportional to the *Non-ionizing Energy lost* by the particle through the sensor.

The radiation effects on silicon will depend on the particle nature. While neutral hadrons will interact only by inelastic collisions with the lattice atoms, slow charged hadrons will lose a part of their energy by ionization but will not have enough energy to create large clusters and finally, fast charged hadrons will lose energy by ionization and will have enough energy to create PKA with enough energy to create large clusters in silicon. A detailed description of the

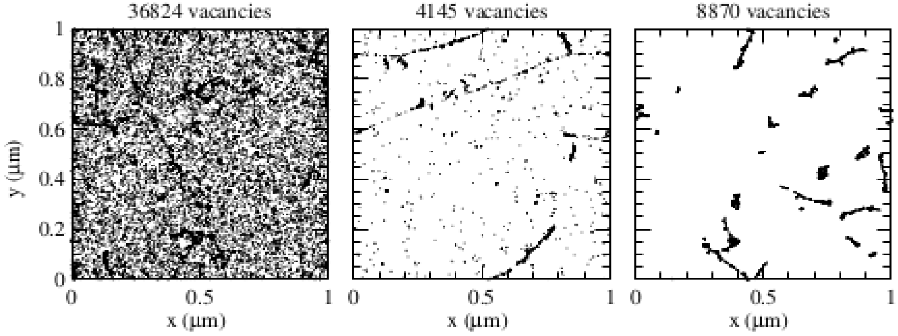

Figure 2.7: *Simulation of defects formation in silicon by different particles. Left: 10 MeV protons. Center: 24 GeV protons. Right: 1 MeV neutrons. Sourced from [77].*

processes and simulation results (see Figure 2.7) are shown in detail in [77].

The NIEL hypothesis considers all the cross sections of all the possible non-ionizing interactions $\sigma_\nu(E)$ for each particle ν with an energy E. Each collision of energy E, producing a recoil on the atom with an energy E_R will occur with a probability $f_\nu(E, E_R)$. The probability for this atom to produce more dislocated atoms can be weighted by the *Lindhard partition function* ($P(E_R)$). The so called *Dislocation damage cross section (D)* is:

$$D_\nu(E) = \sum_\nu \sigma_\nu \int_0^{E_{R,max}} f_\nu(E, E_R) P(E_R) dE_R \tag{2.25}$$

By convention, the displacement damage is rescaled to a reference value. This reference value is the one produced by a monoenergetic beam of 1 MeV neutrons, producing a proportionality constant κ called *hardness factor*:

$$\kappa_\nu = \frac{\int D_\nu(E)\phi_\nu(E)dE}{D(E_n = 1MeV) \cdot \int \phi_\nu(E)dE} \tag{2.26}$$

In equation 2.26, $\phi_\nu(E)$ is the fluence of particles of type ν with an energy E measured in $particles/cm^2$. This fluence can be rescaled to the fluence of 1 MeV neutrons ϕ_{eq} producing the same damage:

$$\phi_{eq} = \kappa_\nu \cdot \phi_\nu(E) \tag{2.27}$$

The NIEL model has some limitations. It is a good approximation and predictive in the case of primary damage, but it does not model the defects movement in the bulk and cluster formation. The process of traveling and combination of the defects takes the name of *defect annealing.* The defect annealing can be classified into two different processes, *Complex formation and dissociation.* Once the defects have been created, they move to a different site in the lattice, typically by thermal excitation. If the defect ends up in a place where there is another defect, depending on the energy they could combine forming a defect complex, a process known as *complex formation.* When one of the defects in a complex escapes and moves in the lattice, it is refereed to a *dissociation process.*

2.3.2 Impact on the detector

This section describes the radiation damage effects on detector performance. These effects can be classified as follows:

- **Leakage Current.**

  Defects that end up in the middle of the bandgap are able to generate electron-hole pairs and recombination by means of thermal excitation. Free electron-hole pairs can also be created in the depleted area, contributing to the inverse current. This effect is already important after very low irradiation fluences. As shown in equation 2.28 the leakage current increment after irradiation is directly proportional to the radiation fluence ϕ and the applied biasing voltage V_{bias}.

  $$\Delta I_{leak}(\phi) = \alpha \cdot \phi \cdot V_{bias} \tag{2.28}$$

  The proportionality constant α is named *damage constant* and depends on temperature and annealing processes, having a different parametrization depending on the annealing time. The detailed parametrization can be found in M. Moll's thesis [69].

- **Depletion Voltage.**

  As seen before, $V_{fd} \propto |N_{eff}|$. Some of the defects induced by radiation act as shallow donors or acceptors. These defects cause levels to shift close to the bands, and become easily fully ionized at room temperature.

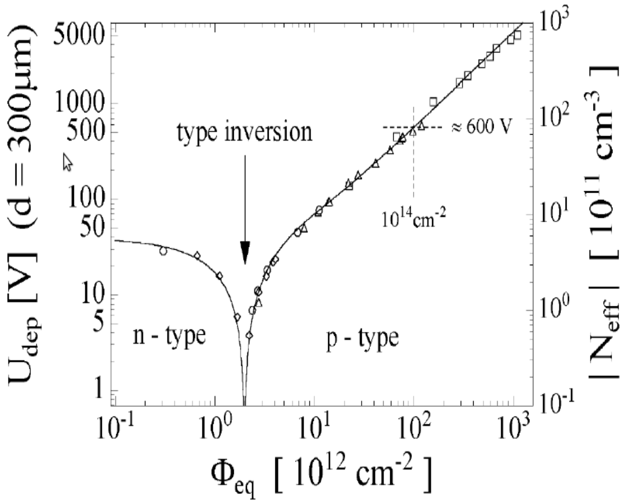

Figure 2.8: *N_{eff} and V_{fd} variation with irradiation fluence for a standard Float Zone p-on-n sensor. Sourced from [79].*

Even deeper defects can also contribute to the change in N_{eff} when a external voltage is applied. A well known effect in irradiated silicon sensors is called *donor and acceptor removal* [78], whereby dopants are moved from their position and inactivated. When the sensor is biased, deep defects will be activated close to the two implants, determining the formation of two separate junctions. The p-like defects will be activated close to the n^+ region and viceversa. This *double-junction* effect is always present in irradiated silicon detectors reaching a *type inversion* in Float Zone n-bulk sensors, see Figure 2.8. The predominant junction is determined by the relative concentration of defects and their activation energies. The depletion process in irradiated sensors involves the creation of two different space charge regions.

Figure 2.8 shows the *type inversion* in a FZ sensor. When applied voltage (U_{dep} in figure) reaches zero, the number of acceptor and donor like defects is balanced. After this point, acceptor-like defects predominate leading to a complete type inversion, moving from a n-type to a p-type bulk.

The variation in the effective carriers density N_{eff} has contributions from the *short term or beneficial annealing*, *long term or reverse annealing* and *stable damage.* Every contribution is proportional to the fluence and to the defect introduction rate. In annealing contributions, the most important one is the reverse annealing, which is strongly dependent on temperature. In the detector operation, temperature should be below 0°C in order to minimize annealing and changes in V_{FD}. The *Stable damage* N_C is a contribution independent from annealing time and temperature.

- **Trapping.**
  Trapping is an unavoidable phenomenon in silicon sensors and it is caused by crystalline defects that introduce energy levels in the bulk with a high capture cross section. When those levels are far from the two bands, the re-emission time will be of the order of milliseconds. From the point of view of the sensor performance, the charge collection will be reduced because part of the charge can be trapped and re-emitted very late to be collected in the proper time. This trapped charge will be lost.

  After irradiation, in addition to those trapping centers present in the original lattice, new ones from radiation induced defects are added. This is a bigger contribution to the trapping centers density. Due to the amount of trapping centers in the bulk after irradiation, the lifetime of the carriers is considerably reduced, reaching values $< 2\ ns$ for samples irradiated up to $1 \cdot 10^{15} n_{eq}/cm^2$. This new lifetime is of the same order of magnitude than the drift time of the carriers in the sensor. As a consequence, the signal will be degraded considerably.

  A parametrization of trapping was proposed in [80], where it is shown that the inverse of the lifetime is proportional to the NIEL-related bulk damage and fluence:

  $$\frac{1}{\tau} = \frac{1}{\tau_i} + \phi \cdot K \tag{2.29}$$

  The parameter τ_i is the intrinsic lifetime of carriers ($\sim ms$ and negligible), and K is a constant that depends on the carrier nature (electron or hole) and particle nature (neutral or charge hadrons), but it is independent of the silicon type (n or p) and the trapping constant [81].

- **Avalanche charge multiplication.**

  The avalanche charge multiplication is an effect recently studied in highly irradiated silicon sensors [82, 83]. The collected charge is higher than that expected for the sensor thicknesses and irradiation doses, with some of the devices showing even higher charge collection than unirradiated devices. This effect is still under study, but a probable reason is the fact that the high value of N_{eff} causes a very high electric field in a small region. This effect could compensate for the charge lost in n-in-p sensors, but up to now, this effect is observed at very high voltages. R&D efforts are focusing in field engineering to decrease the need voltage to reach this effect.

- **Surface damage.**

  Surface damage is unavoidable and it occurs when defects are introduced in the passivation SiO_2 layers of the detector. The damage is mostly caused by ionization of the oxide. When this happens, electrons escape the oxide while positive ions stay on the layer creating a positive space charge in it. To compensate for this, free electrons from the bulk accumulate next to the passivation layer creating a new negative space charge that results in a conductive layer between segmented electrodes (strips or pixel). Another consequence of this is the generation of a high local electric field, causing breakdown and avalanche effects.

  There are two popular techniques used to avoid this effect. One is the so-called *p-stop* and consists of the use of a p-type silicon *"barrier"* surrounding the electrodes. Another one is the *p-spray* technique, that consist of adding a p-type layer between sensor bulk and passivation layers.

Chapter 3

Laboratory Techniques

In this chapter, the different characterization techniques and experimental arrangements used in this work are described. Results of these studies are presented in chapters 4 and 5.

The characterization techniques were:

- Electrical characterization. The objective is to determine the electrical properties of the sensor either in the bulk or in the different device structures. These measurements are necessary to know the sensor electrical properties before connecting it to the readout electronics.

- Laser characterization. This technique was used in two-dimensional position-sensitive strip detectors. The laser beam is used as a signal inductor in the sensor. These measurements were done at the Instituto de Física de Cantabria (IFCA) semiconductor characterization laboratory [84].

- Radioactive source. To characterize detectors response to ionizing radiation a ^{90}Sr radioactive source was used.

- Test beam. In a test beam, the measurements of the 3D pixel sensors efficiency before and after irradiation were performed.

3.1 Electrical Characterization

The electrical characterization is part of the *quality control* of silicon sensors and consists of different electrical tests to verify that the design electrical parameters are achieved in the final sensor production; in addition the sensor full depletion voltage is determined.

Some of these parameters are not easily measurable in the sensor, either because the test itself is destructive or because it is impossible to measure the parameter directly. Therefore a set of dedicated test structures is required to measure them. In practice, every sensor wafer includes several electrical test structures designed with the sole purpose of measuring those specific parameters. The main references used to write this section are taken from the T. Bergauer Diploma Thesis [85] and the A. Furgeri Thesis [86], where the different test structures and the measurement procedures are described in detail.

The results of this characterization are implemented in the detector simulation in order to make it more similar to the real devices.

3.1.1 Description and objectives

Two important electrical characteristics to measure in a sensor are the leakage current and capacitance dependence with the bias voltage, the IV and CV characteristic curves, respectively. The functionality of the device is evaluated with the IV-curve and the depletion voltage is extracted from the CV-curve. The bias resistance is also an important parameter to measure in strip detectors because as was shown in section 2.2.3 it has a significant contribution to the sensor's noise. Measurements of strip and interstrip capacitances and resistances are also necessary, because they play an important role in the signal to noise ratio as well as in the final sensor position resolution.

Figure 3.1 shows the internal and surface structures that compose one of the CMS tracker's strip detectors [86]. This example is used in this section to illustrate the measurement procedures. The sensors used in this work were electrically characterized in the IMB-CNM laboratories [87] using a Cascade Microtech probe station [88],two Keithley 2410 Source/Meters [89] and an Agilent 4284A LCR Meter [90]. In case of capacitance measurements a decoupling box was required in order to decouple the AC signal used to measure

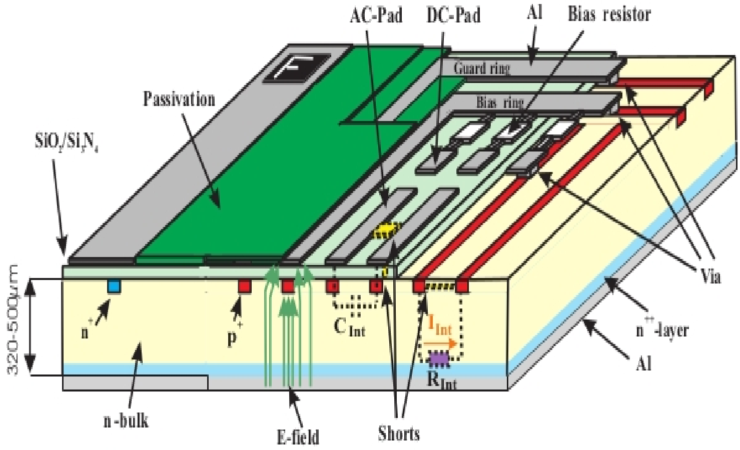

Figure 3.1: *Details of a microstrip detector where the different structures that compose it are visible. Source: [86].*

capacitances and the DC signal from the high voltage applied to bias the sensor. All measurements were done at 20 °C and keeping the relative humidity below the 20 %.

Details of an AC-coupled strip detector front side are shown in Figure 3.2, where part of the AC pads and DC pads connected by the bias resistor to the bias ring are visible. The DC leakage current goes through the biasing circuit while the signal is collected through the AC-pad (see section 1.2).

- Leakage current dependence with bias voltage. IV curve.
  Measurements of the IV curve in sensors give an idea of how good is the silicon bulk purity, because I_{leak} increases proportionally to the amount of defects, either introduced by irradiation or in the manufacturing process.

  To measure this curve, a voltage ramp is done recording the current for every voltage value. A sensor (n-in-p/p-in-n) is biased using two probes at the same voltage (positive or ground/negative or ground) connected to the bias and the guard ring and applying the opposite voltage (ground or negative/ground or positive) to the chuck. The chuck is connected to the sensor backplane and a "capacitor" between anode and cathode

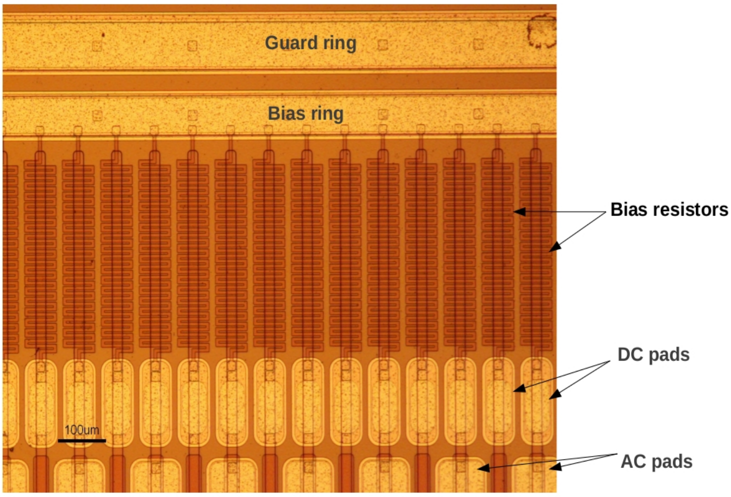

Figure 3.2: *Picture of one area of a 2D positional sensitive microstrip sensor. AC and DC Pads are distinguishable, as well as bias resistors, bias ring and guard ring.*

(ohmic or pn-junction) is created keeping the right polarity to have a reverse polarization applied on the device. The polarity of the applied voltage will depend on the diode structure (see section 2.1.4). In a p-in-n device the backplane will be biased to a higher voltage than the rings and the opposite in an n-in-p device. In our measurements with microstrip sensors (p-in-n), the backplane voltage is set to ground and a negative voltage is applied through the probes. With pixel devices (n-in-p), the backplane was grounded and a positive voltage was applied to the front side.

The IV curve is measured in the sensor and also in the dedicated structures, standard diodes (details in section 2.1.4). These diodes are usually situated in different places on the wafer in order to identify possible wafer inhomogeneities.

The *breakdown voltage* (V_{bd}) is the voltage after which carriers acquire enough energy to form secondary electron-hole pairs producing an avalanche behavior in the diode structure and it can also be measured using this curve.

Typically, the standard requirements in a 300 µm thick sensor are to

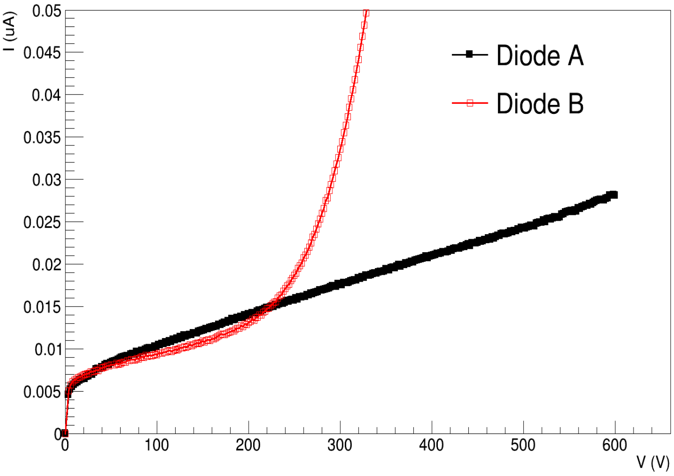

Figure 3.3: *Measurement of the current dependence with the reverse bias voltage in two 1 cm^2 diodes (IV curve). In diode A the breakdown voltage is over 1000 V while in diode B, the breakdown voltage is lower than 300 V.*

keep $I_{leak} < 0.1\ \mu\text{A}/\text{cm}^2$ at the operating voltage V_{op} and to have as high V_{bd} as possible to avoid the undesired avalanche effects during its operation. Two IV curves measured in 300 µm thick diodes are shown in Figure 3.3. In one diode, the breakdown voltage is not visible while in the other is lower than 300 V.

- Capacitance dependence with bias voltage. CV curve.

  As was shown in chapter 2, the capacitance measurement is the standard method to determine the full depletion voltage (V$_{FD}$), see equation 2.13. This magnitude is measured in sensors and diodes. From V$_{FD}$ we can derive the dielectric resistivity of a sensor of thickness d using the following equation:

  $$\rho = \frac{d^2}{2\epsilon_0\epsilon_{Si}\mu_e V_{FD}} \tag{3.1}$$

  And the carrier concentration from:

  $$N = \frac{2\epsilon_0\epsilon_{Si}\mu_e V_{FD}}{ed} \tag{3.2}$$

  In capacitance measurements, the frequency of the sensing sinusoidal signal (from the LCR Meter) is a parameter that becomes more relevant in irradiated devices, where the CV-curve depends on the frequency of that signal. This is due to the dependence of the effective doping density N_{eff} with irradiation (see Figure 2.8 in previous chapter). This phenomenon that occurs when a signal is injected in a device with defects is called the *small signal trapping effect* [91]. When capacitance measurement results are presented, the frequency at which the measurements have been made should always be specified for later comparisons.

To measure this curve, the sensor is biased using the same schema than for IV-curves, but in this measurement the sensor is biased and simultaneously a sinusoidal signal is injected through the probe to measure the phase. Therefore the decoupling box used to isolate high voltage and LCR signal is mandatory. The voltage ramp is done in steps of 5 V, and the measured capacitance is recorded for every voltage.

One peculiarity of this measurement is that in order to get the sensor capacitance value, one must measure the capacitance of the circuit excluding the sensor, to subtract it. To do this we set all the needed cabling, but sensors and probes disconnected from each other and we take a measurement, known as measurement *"in open circuit"*.

Once the capacitance dependence versus the bias voltage is measured, the magnitude $1/C^2$ versus the applied voltage is plotted (see section 2.1.3) and following equation 2.13, the full depletion voltage (V_{FD}) is estimated. The procedure to obtain the V_{FD} is fitting a line separately to both behaviors. In Figure 3.4, an example of this measurement is shown. The intersection of both lines is consider the V_{FD}. In practice, the operation voltage V_{op} is taken always at least 50% higher than the intersection between both lines to ensure that the device is operating fully depleted.

- Coupling Capacitance

  The *coupling capacitance* refers to that capacitance between strip implant and the AC pads, and it requires a specific test structure, called TS-CAP and shown in Figure 3.5. The specific test structure consists of 26 strips (only implant) connected directly to the bias ring without

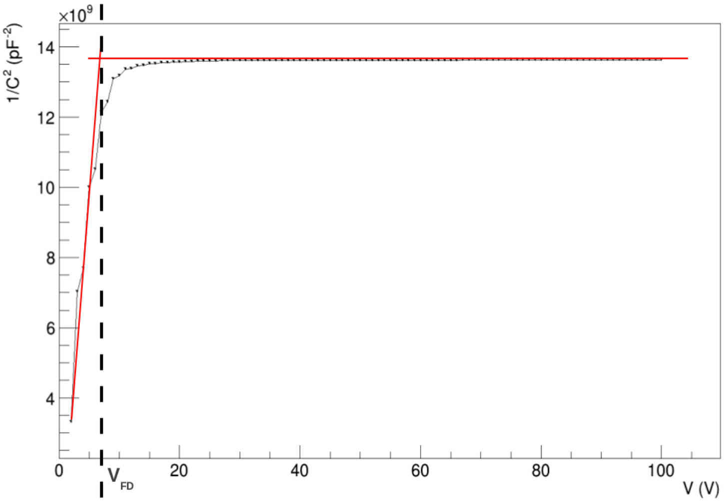

Figure 3.4: *Measurement of the 1/C^2 dependence with the bias voltage. In this case, the V_{FD} is around 7 V and the operating voltage will be higher than 10 V.*

a polysilicon resistor. Each strip can be read out by its AC pad that is placed on one end of the strips. The dielectric structure is the same as that of the sensor itself. Measuring a CV-curve we measure the capacitance between pad and the bias ring directly connected to the implants, therefore the dielectric thickness between them. This dielectric is formed by the same passivation layers material, usually SiO_2 and Si_3N_4 and this measurement allows to know if there are pin-holes or shorts between implant and aluminum contacts producing undesired signal leaks.

In DC coupled devices this measurement and test structure don't exist (see section 1.2), because they don't have this dielectric structure.

The CMS specifications of the coupling capacitance are 1.2 pF·cm $^{-1}$ · µm^{-1} per implanted strip width.

- Flatband Voltage

  Another common test structure is a *Metal-Oxide-semiconductor* (MOS) structure. The MOS structure contains the same SiO_2 layer than the thick interstrip layer and is the one used to measure the *flatband voltage* V_{fb} and the oxide capacitance of the SiO_2 in between strips.

  Keeping the gate to ground and applying a voltage to the backplane (see

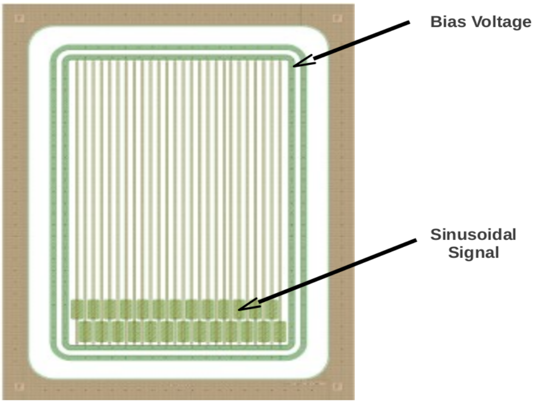

Figure 3.5: *TSCAP structure layout. 26 strips connected directly to the bias ring without a polysilicon resistor and with an AC pad in every strip to read them out.*

Figure 3.6), there are three possibilities:

- **Accumulation** ($V_{gate} > V_{fb}$): Accumulation of free electrons under the gate. The only measured capacitance is the oxide capacitance.
- **Depletion** ($V_{gate} \leq V_{fb}$): Increasing the voltage, the semiconductor region under the gate depletes of free electrons. The capacitance decreases until there are no more free charges in the bulk. In the ideal case it happens when $V_{fb} = 0$. The V_{fb} measurement allows to know the trapped positive charges in the oxide: the farther V_{fb} is from zero, the more trapped charges there are in the oxide layer.
- **Inversion** ($V_{gate} << V_{fb}$): holes accumulate under the gate.

Measuring a CV-curve, therefore the oxide capacitance, we are able to assess the dioxide thickness using again equations 3.1 and 3.2. The flatband voltage measures the trapped positive charges in the oxide. The flatband voltage corresponds to the voltage that, when applied to the gate electrode, yields a flat energy band in the semiconductor.

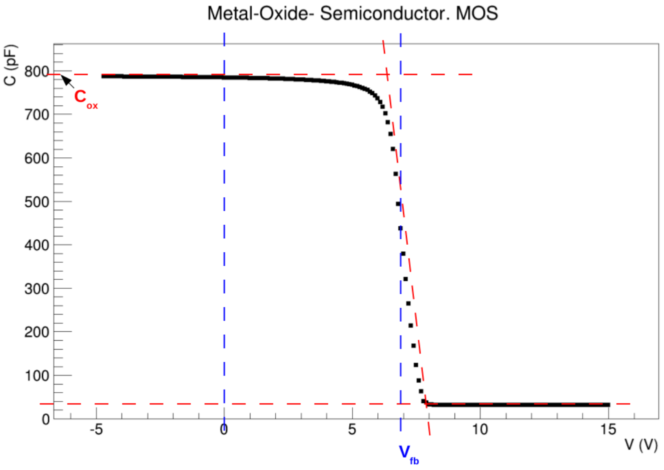

Figure 3.6: *CV curve for a MOS structure, where the empirical calculation of* C_{ox} *and* V_{fb} *are illustrated.*

The measurement of the flatband voltage is a measurement of the quality of the oxide layer between the silicon bulk and the read-out metal.

- Interstrip Capacitance

  A high *interstrip capacitance* C_{int} increases the noise, decreasing the signal to noise ratio and the final detector resolution. This measurement is made in another test structure called CAP-TS-AC (see Figure 3.7) and requires of several probes to connect all the needed pads properly. It is measured biasing the structure to the *operation voltage* V_{op} using the backplane and the bias ring (1 probe), the sinusoidal signal is into the AC pad of the central strip, keeping the nearest two neighbors grounded through their respective AC pads (3 probes).

  The test structure includes two sets of three strips surrounding the tested ones shorted and grounded. In this measurement the guard ring was not biased because of the limited number of probes -4 probes- in the probe station.

  The desired value for C$_{int}$ is as small as possible, and in practice a desirable value is in the rage between 0.5-1.5 pF/cm. This measurement

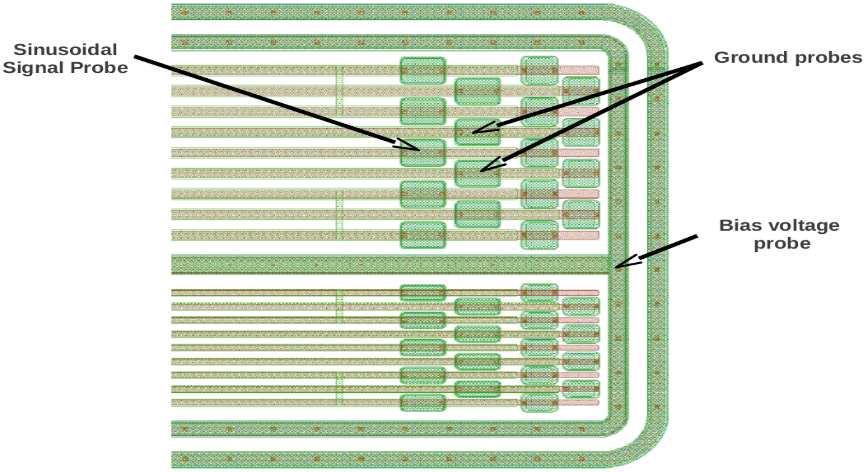

Figure 3.7: *Zoom of one extreme of the CAP-TS-AC structure layout, where there are three central strips to perform the measurement and two sets of three strips shorted and grounded. The CV curve measurements are done through the pads. It includes two different geometries of strips.*

requires a sinusoidal signal with a frequency of 1 MHz.

- Interstrip Resistance

  The *interstrip resistance* R_{int} is measured in a test structure called CAP-TS-DC, which is very similar to CAP-TS-AC but without polysilicon (bias) resistors (see Figure 3.8). The strips are isolated from the bias ring and the p^+ implant is directly connected to the metal via. As for the C_{int} measurement, the R_{int} is measured between one strip and its neighbors which are grounded.

  To measure resistance, an IV-curve is measured and its slope is fitted by a line following *Ohm's law.* The central strip is set to a potential and the neighbors to ground, performing a voltage ramp we get the resistance value from the fitted slope. The device is also biased to deplete the area closer to the implants and reproduce the real operational conditions. R_{int} should be higher than 1 GΩ to ensure a good performance of the sensor.

- Resistances: Bias, implant and metal

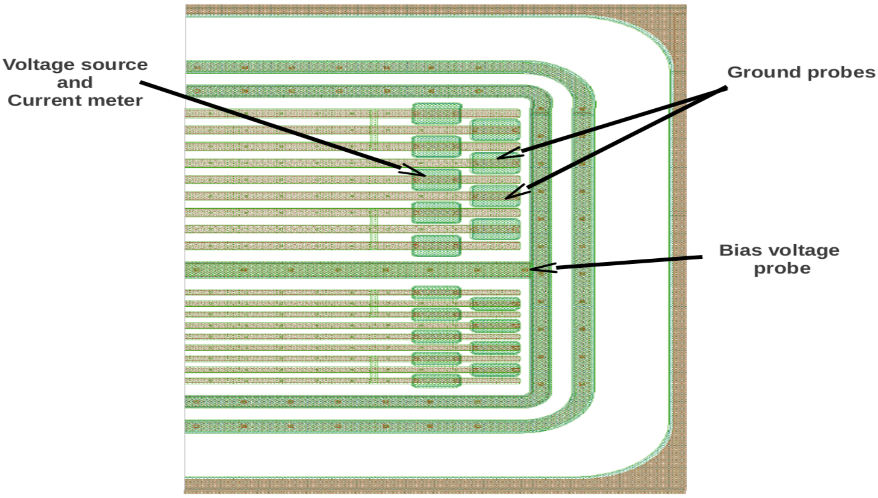

Figure 3.8: *Zoom of one extreme of the CAP-TS-DC structure layout, where there are three central strips to perform the measurement and two sets of three strips shorted and grounded. The IV curve measurements are done through the pads. It includes two different geometries of strips.*

In a strip sensor there are several resistive materials to characterize. These structures are bias, implant and metal resistances. There is a dedicated structure for this purpose, called *sheet*, which includes the three structures with one pad each to measure IV curves and determine the resistance values. There are different lengths and widths to compare results (see Figure 3.9). In the case of 2D position-sensitive strip detectors, instead of metal, a polysilicon strip is used as electrode. Some extra resistance measurements have been done in these detectors to know the real resistance of the electrode.

The electrical characterization is the first step after a sensor production. The described procedure is the one used for strip detectors. Pixel detectors, which are quite simpler structures, are characterized measuring IV and CV curves in diodes and sensors.

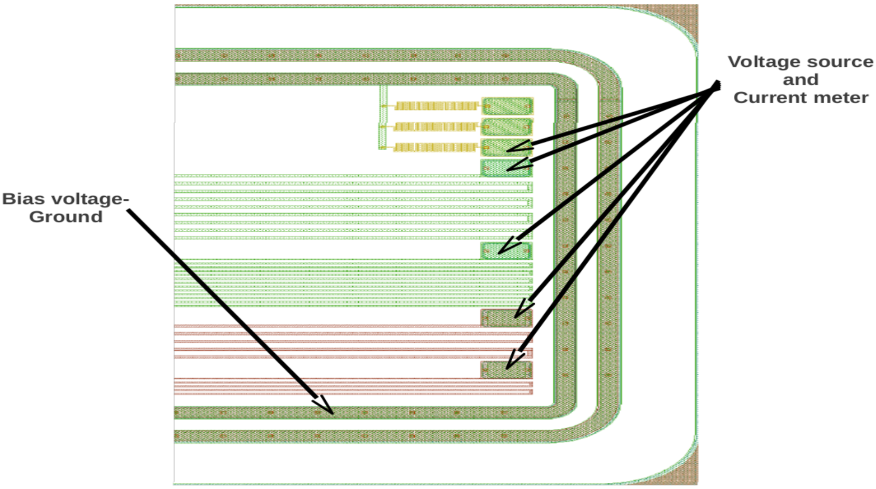

Figure 3.9: *Zoom of one extreme of a sheet structure. Different materials and geometries are distinguishable, except for the three polysilicon resistors (bias resistors), which have the same geometry.*

3.2 Laser characterization

We used an infrared laser beam to characterize the sensor response. This laser wavelength was chosen because it traverses the full sensor thickness, therefore it is the most similar case to a real Minimum Ionizing Particle (MIP) going through the complete sensor thickness. In addition, using a laser beam the input signal in the sensor is well known thanks to a photodiode that it measures the signal intensity. Actually, a laser beam is used to have a high signal in the detector (output) that can facilitate specific studies. Another advantage of measuring with a laser is that we don't need to wait to accumulate statistics as is the case with MIPs.

To characterize the charge division produced along a resistive electrode made of polysilicon in microstrip sensors this technique was used. The laboratory test-stand allows to scan the detector surface with very high accuracy and it was placed at a clean room (class 5.5 according to the ISO 14644) in the IFCA facilities ensuring stable temperature and humidity conditions.

3.2.1 Setup description

Figure 3.10 shows a photo of the setup. This setup allows to move the laser along the sensor surface and in the direction perpendicular to that plane. It has a three axes stage with displacement accuracy better than 10 µm (3 Adept Python Linear Modules, L18 - L12 - L08).

The laser is a QPHOTONICS [92] pulsed distributed-feedback diode operated in a constant optical power mode and thermally controlled by a *Standford Laser Controller* [93]. The laser output is send into a monomode optical fiber and using an inline fiber optic splitter from Schäfter + Kirchhoff [94], the laser beam is divided in two beams going through two different fiber outputs. One of the fiber outputs goes to a reference photodiode (2 GHz bandwidth) and is monitored in a digital scope allowing the study of the laser stability and to know the beam conditions for each measurement. The other fiber output is carried until it illuminates the sensor after passing through a collimator and a microfocusing optical head [94]. The laser wavelength is centered at 1080 nm, the laser rise time measured in the scope coming from the reference photodiode is 2ns, and the beam profile has a Gaussian shape with $\sigma = 5$ µm.

3.2.2 Test-stand optimization

Working with laser beams requires some considerations. The main ones are to focus properly the laser beam in the sensor surface and to align properly every device with respect to each other. The procedure was as follows:

- Mechanical alignment of the setup. As is visible in Figure 3.10 every component was set on an optical table, in such a way that every element is easily fixed and aligned. IN addition, the setup is protected from any external vibration.

- Focusing the beam spot. A focused beam spot has the peculiarity that, outside of the focus point, the beam grows quickly (see Figure 3.11). To focus the beam on the sensor's surface we bias the sensor and aim the beam at the center of a metal pad. A laser of λ =1060 nm cannot penetrate the pad, and a signal is read only if the beam area exceed that of the pad. The sensor is readout by the *ALIBAVA* system [95] and

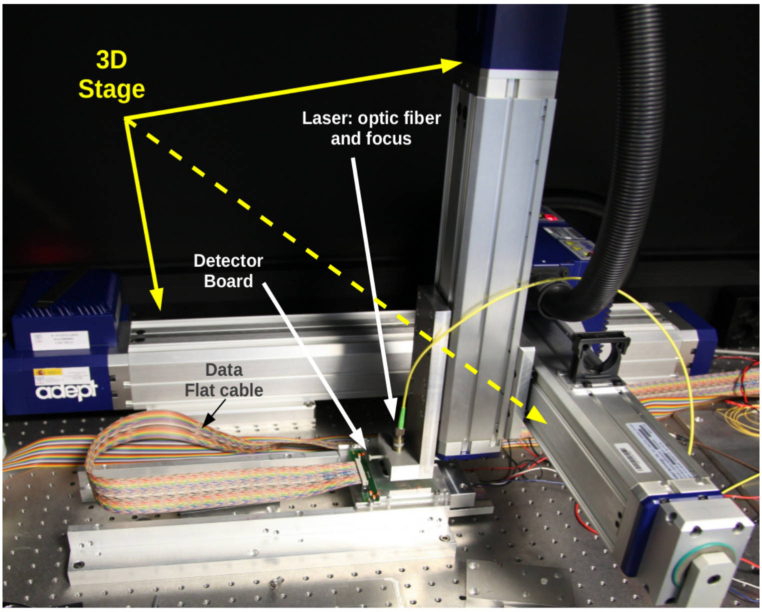

Figure 3.10: *Photography of the laser test-stand at IFCA laboratory. The optic fiber carrying the laser beam, stage and sensor board are visible.*

we can see the sensor response to the laser hit on the online monitor. We move the laser perpendicularly to the sensor (Z-axis of the stage) until we lose the signal. At this point the beam area is inside the pad's area. Moving in the sensor plane (XY- axis of the stage) we can find the pad limits and calculate its center. Once the beam is centered in the metal pad, the laser focus is moved up and down looking for the position between the two where we start seeing a signal (Positions 1 and 4 in 3.11).

- Beam alignment in XY-plane. The pad center marks the edge of the metal strip. The stage is moved following the strip direction and with the help of the monitored signal, we look for the pad at the opposite extreme of the strip. Once we consider that we are aligned, we check the alignment moving the beam to the strip center (using only the 3-axis stage coordinates) and from there to the neighbors by pitch units. If we are not able to move strip to strip just moving the laser by changing the stage coordinates all previous steps are repeated until we reach the

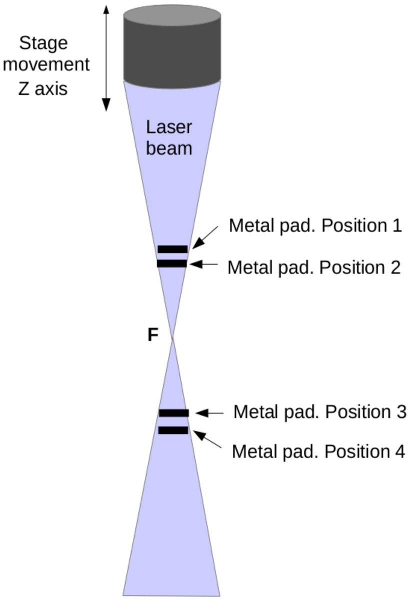

Figure 3.11: *Laser beam focusing strategy. Focusing the beam spot looking for the points where we start seeing a signal (positions 1 and 4) we assess the middle point to determine the focus position. Between positions 2 and 3 there is no signal because the pad area is bigger than the beam section on it.*

proper alignment.

- Laser power. To optimize the laser power, we tuned the laser drivers and we used inside inline optical fiber attenuators [94].

Once the test-stand is properly optimized and fixed, several scans over different strip detector surfaces are carried out.

3.3 Characterization with a radio-active source

The signal-to-noise ratio is measured using a radioactive source. A commonly used radioactive source is ^{90}Sr for several reasons explained below.

Strontium-90 as Source of ionizing radiation. Strontium-90 decays to Yttrium-90 which β-decays to Zirconium-90, which is stable. The end point energy (which is equal to the energy difference between the initial and final states in β-decays) of ^{90}Sr is 0.546 MeV and for ^{90}Y it is 2.28 MeV. Strontium can be considered a pure electron emitter. In Figure 3.12 the energy spectrum for the Yttrium beta decay is shown.

The response of a silicon detector to a ^{90}Sr is considered similar to the response to a Minimum Ionizing Particle (MIP). A MIP is a charged particle which loses the minimum energy by ionization in a medium. This situation occurs when the kinetic energy of a particle is at least twice its rest mass. For example, electrons (or protons) can be considered as minimum ionizing particles when their kinetic energy is greater than 1 MeV (or 2 GeV) [96].

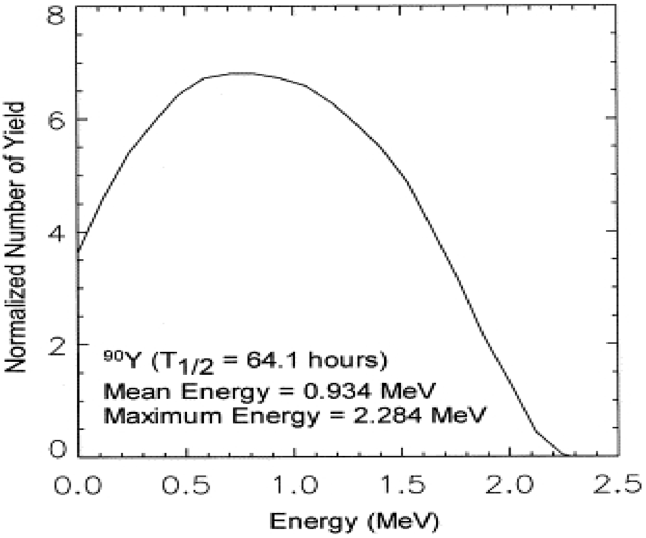

Figure 3.12: *Beta decay energy spectrum for Yttrium-90. Source [97].*

The absorption of the beta electron is described by the Bethe-Bloch process. Figure 3.13 shows the graph of electron absorption in silicon. Electrons pass through the silicon sensor depositing some energy according to the Bethe-Bloch expression and penetrate in a scintillator placed behind the detector. The only electrons that will trigger the photomultiplier (PMT), are those that traverse the detector and deposit enough energy in the scintillator to exceed the PMT threshold.

The charge collection efficiency of a detector can be measured by means of a ^{90}Sr radioactive source. This measurement is performed at different voltages to estimate the full depletion voltage measuring the charge collection efficiency.

Two different setups for a characterization with a radioactive source were used depending on the tested sensor:

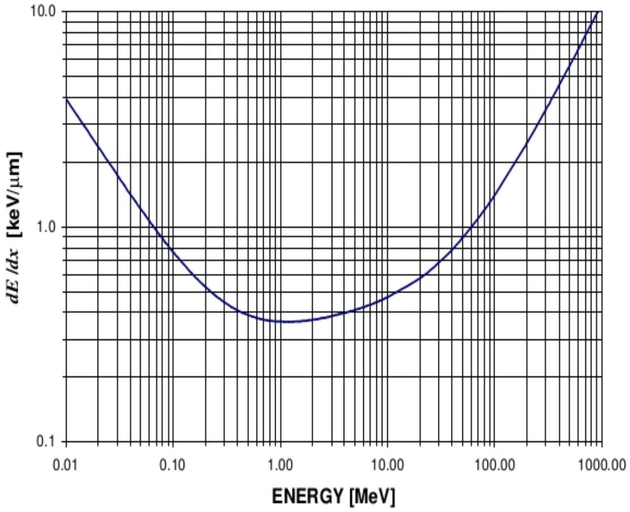

Figure 3.13: *Bethe-Bloch graph for beta electron absorption in silicon. Source [98].*

- One setup was used to characterize the signal to noise ratio of the 2D-position sensitive strips detectors at IFCA. The setup is the same as the one used in the laser characterization (Figure 3.10) but instead of having the laser head attached to the 3-axis stage, it was a mechanical support holding the ^{90}Sr radioactive source. A scintillator with a photomultiplier under the sensor board was used as trigger. These measurements were made at room temperature, given the fact that the sensors were unirradiated.

- A different setup was used to characterize pixel sensors. This characterization was developed at the *Laboratory for Particle Physic* in the *Paul Sherrer Institut, PSI* [99]. The test setup consists of a ^{90}Sr radioactive source with an activity of 3.7 MBq on top of a PCB board carrying the device under test (see Figure 3.14). For triggering, a plastic scintillator readout with a photomultiplier is used. All the components are inside a thermally isolated and light-tight box filled with nitrogen gas. The

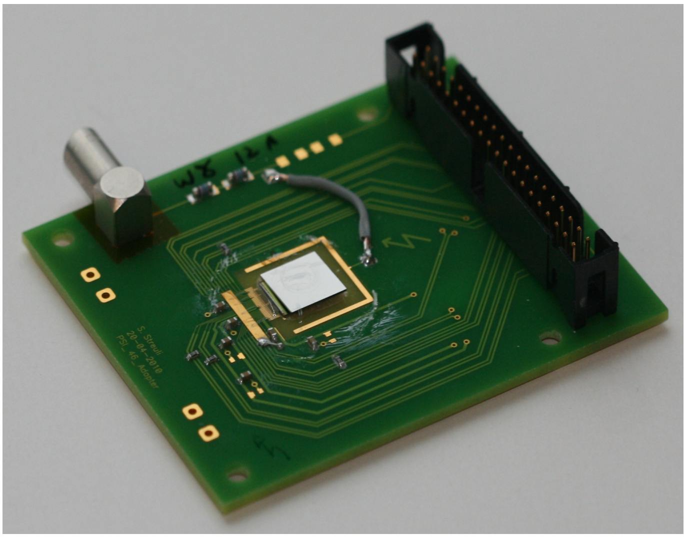

Figure 3.14: *PCB sensor board with a 3D pixel sensor set on top of it. A cover is glued surrounding the sensor and as support for the* ^{90}Sr *source.*

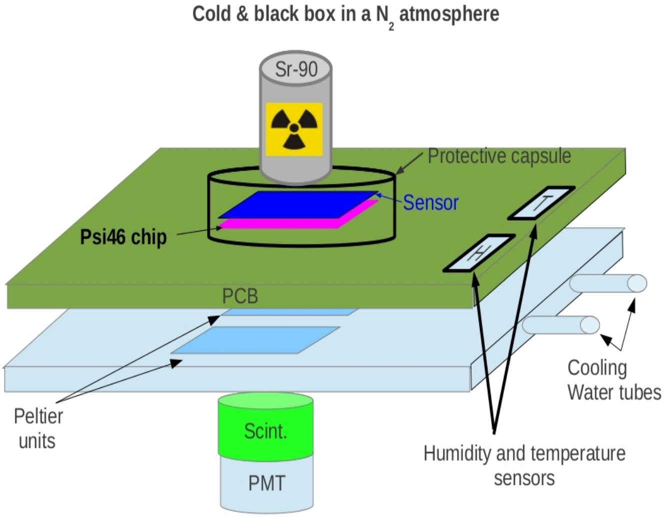

Figure 3.15: *Test-stand for a radio-active source characterization at PSI laboratory.*

calibration temperature and humidity are measured by two sensors in contact with the detector PCB board (PT-100 [100] and HIH-4000 [101]). Figure 3.15 shows the experimental arrangement.

The procedure followed to measure irradiated 3D-pixel detectors was first to set the detector in the box and wait until temperature and humidity were the desired and constant, typically at ∼ −15°C and keeping the humidity always below 20%. Once these conditions are reached and the system is stabilized we started the readout chip calibration an the data taking process.

3.4 Test Beam Characterization

For 3D pixel detectors a characterization in a particle beam was done. In a test beam, detectors under more realistic operation conditions can be tested. This characterization was done at the DESY test beam facilities [102] and with the support of the CMS DESY Group [103].

3.4.1 DESY Facilities

In the DESY test beam facilities, the measurements were done at *line 21* with a beam of positrons of momentum ∼ 6 GeV. For an optimal test beam characterization several factors have to be considered: telescope, device under test (DUT), beam conditions, timing and alignment.

- The telescope belongs to a series of telescopes developed within the *Advanced European Infrastructures for Detectors at Accelerators collaboration (AIDA)* [104]. It is the DATURA telescope and it is a Mimosa-based Pixel Telescope (see Figure 3.16) [105]. It is composed of 6 planes of MIMOSA26 sensors [106], it has precise and flexible mechanics and central DAQ components (Trigger Logic Unit, TLU [107]). The telescope position resolution can reach 4.2 µm in the best beam and telescope conditions (energy, scattering and distance between planes).

  The TLU produces triggers after receiving the coincidence signals coming from four different finger scintillators readout by photomultipliers. Two of them are crossed in front and the other two at the back of the telescope with respect to the beam incidence. The overlap area between the four scintillators is ∼ 1 cm^2.

  In terms of operation of the telescope, the MIMOSA26 readout is continuous, free of dead time and needs an integration time per frame of

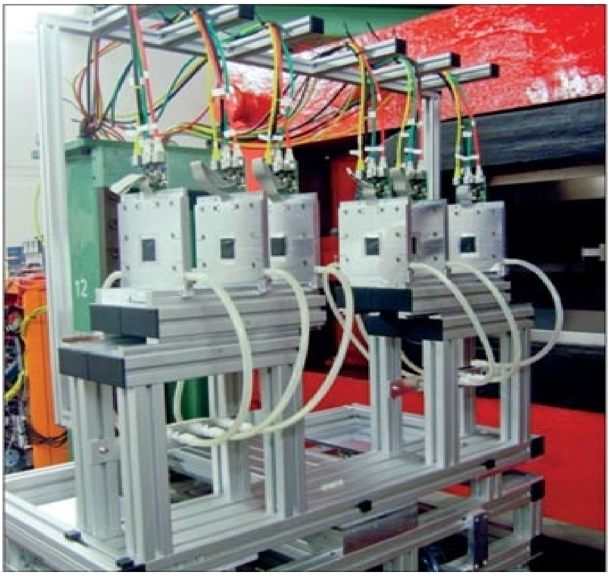

Figure 3.16: *AIDA telescope at the DESY line 21. Sourced from [105].*

$\sim$ 115 µs. The telescope is mounted on a movable support (x-y stage with step motors, remotely controlled). A NIM trigger logic is inside the interlock beam area, and mirrored in the control hut. The telescope uses a CAEN power supply [108] and a HP trigger delay and level adapter (NIM to TTL) [109] in the control hut facilitate the handling of the test stand.

- DESYII beam and timing

  DESYII is the electron/positron synchrotron that provided the particle beam. It has a 80 ms cycle (12.5 Hz) and bunches are separated by 0.977 µs (1.024 MHz). The device under test (DUT) readout electronics includes a FPGA that provides a time stamp for each event by counting 40 MHz clock cycles. Time between bunches takes 39.067 DUT clocks.

  There are two problems from the point of view of synchronization between the test beam setup and the beam itself. One is the fact that the FPGA clock is not synchronized to DESYII and the other one is that the phase of the beam with respect to the clock is not fixed. These reasons make necessary a delay unit to take data synchronously (“on time”). This data taking delay has to be adjusted between runs to sample the signal at the optimal moment.

Another point to take into account is that the MIMOSA chips suffer from pile-up as a consequence of their long readout time ($\sim 115\mu s$). The solution for this requires the use of a second pixel sensor as timing reference situated behind the telescope and scintillator planes. This reference sensor has the same timing as the DUT. If a trigger has associated a hit in every plane of the telescope, DUT and reference sensor, this pile-up effect is suppressed.

- Device under test
  The device under test is a 3D-pixel sensor situated in the middle of the telescope letting three MIMOSA layers in front and three behind it. The setup includes a support to fix the sensor board and the test board (see Figure 3.17) with an isolation cold box surrounding the sensor. This cold box includes a tube and two *Peltier units*. A refrigerant liquid coming out from a chiller is circulated through the tube and the Peltiers are biased until we read the desired temperature in a Pt-100 placed close to the sensor board. The minimum temperature reached at the beam line test stand was ~ -15°C. This temperature is very similar to the reachable temperature in a real experiment.

- Reference pixel sensor
  As already explained, a reference pixel detector is needed to avoid those events with telescope pile up. In our measurements the reference device was a standard planar sensor with a digital read out chip. This sensor is commonly used as reference by the DESY CMS pixel group.

- Alignment
  Once the DUT is properly aligned mechanically, the following steps are to align the setup with the particle beam. First, looking for the maximal trigger rate coming out from the scintillator photomultipliers and second processing the DUT data online and checking if the beam profile is visible in the pixel hit map (see an example in Figure 3.18). Once all these quick tests have a satisfactory result, a full preliminary analysis including reference sensor, telescope and a standard DUT is developed. To align

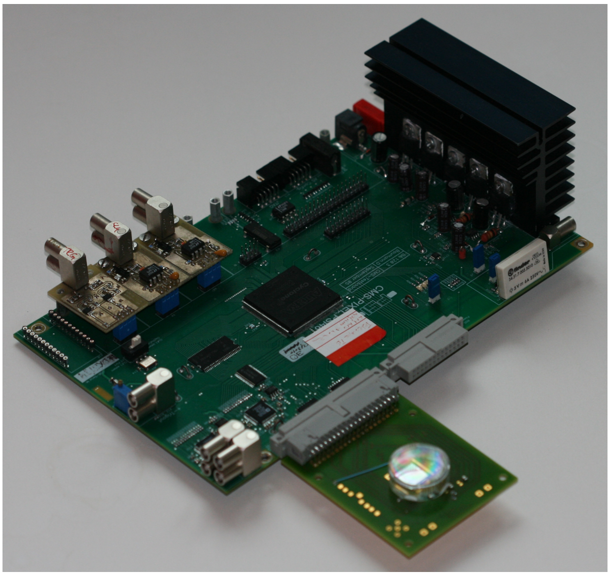

Figure 3.17: *Photography of a sensor board plug into the test board. A plastic cover over the sensor to protect it is also visible.*

the full setup, it is necessary to use a standard sensor as DUT. We consider standard an unirradiated and planar pixel sensor previously tested in the laboratory.

- Data taking
  When the setup is aligned, the data taking process starts taking into account that the delay between beam and setup has to be re-adjusted between runs.

3.5 Irradiation Facilities

In this work, results on the characterization of irradiated 3D-pixel sensors are included. For this purpose an irradiation campaign was developed irradiating diodes, strips and pixel sensors all of them manufactured with the 3D-technology. In this work only results concerning pixel detectors are included. The irradiation campaign consisted of several particle fluences of neutral and charged hadrons (neutrons and protons).

As discussed previously, 3D-technology becomes promising in experiments

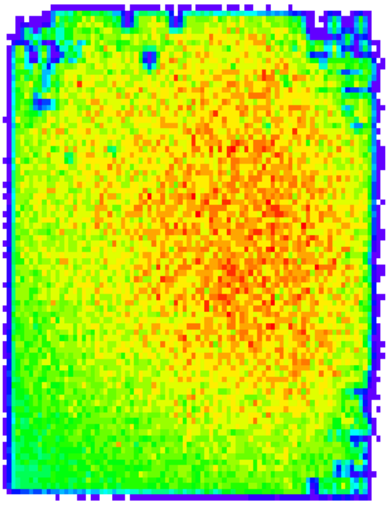

Figure 3.18: *Beam profile visible on an unirradiated 3D-pixel detector during a test beam at DESY facilities.*

where the expected radiation fluences are very high.

- Neutron irradiation facility
  The neutron irradiation facility used is the Reactor Center at *Jozef Stefan Institute* [110]. It is a TRIGA Mark II research reactor. Depending on the reactor power, the particle flux (neutrons) varies between $2 \cdot 10^9$n cm^{-2} s^{-1} and $2 \cdot 10^{12}$n cm^{-2} s^{-1} with a continuous energy spectrum.

- Proton irradiation facility
  The proton irradiation facility used is the cyclotron in Karlsruhe Institute of Technology, KIT [111]. The machine accelerates H$^-$. The two electrons are stripped at a foil and half a meter from the exit window a thermally and electrically insulated box is placed, which holds the samples. The proton energy is $\sim$ 23 MeV at the samples position. The beam spot has a diameter of a few millimeters and the samples have to be scanned. Therefore the box is mounted on a controlled XY-stage. One of the advantages of these installations is that samples are kept cold within a N_2 atmosphere (~ -30°C) during the irradiation process. This is specially important for annealing studies. In neutron irradiation fa-

cilities, typically reactors, the temperature during irradiation is not well known.

Chapter 4

Novel 2D position sensitive microstrip sensors

Semiconductor sensors are often used as two dimensional position sensitive detectors. Some examples are the double-sided microstrip detectors or the pixel detectors. Double-sided microstrip detectors collect electrons and holes, resulting in different pulse shapes that complicate the signal readouts [66], while pixel detectors require a complex readout system with a large number of electronic channels to have both coordinates with enough spatial resolution.

In this chapter a new sensor in presented. It is a semiconductor microstrip detector designed in such a way that it is sensitive to the two coordinates of the ionizing event position in the sensor.

A standard microstrip sensor is only sensitive to one coordinate, which is given by the position of the impact in the direction perpendicular to the strips. Due to capacitive charge sharing [112], a hit induces a signal in different strips. The position of the hit is determined by the charge weighted center of gravity of these strips. The digital resolution in the position measurement (σ) is given in terms of the pitch (p) or distance between strips as $\sigma = p/\sqrt{12}$. A description of standard strip detector performance was given in Chapter 2.

The new sensors introduced here replace the metallic electrodes with resistive electrodes (see Figure 4.1). Polycrystalline silicon is used as resistive material, and the hit position along the strip length is determined from the signal attenuation along the resistive electrode strip.

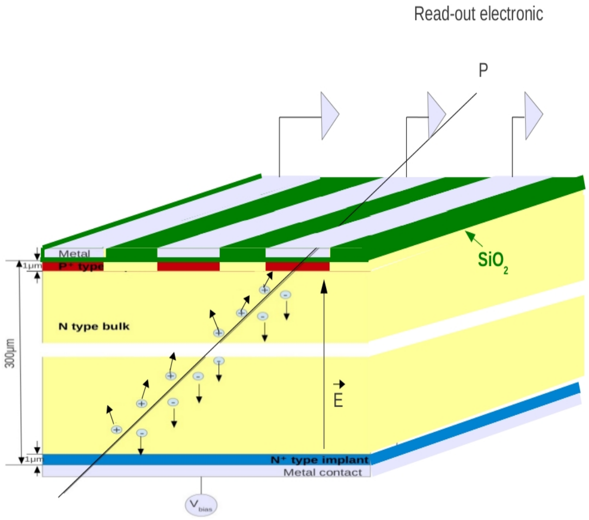

Figure 4.1: *Basic structure of a standard strip detector p-on-n type.*

Two different sensor designs have been manufactured at Instituto de Microelectrónica de Barcelona - Centro Nacional de Microelectrónica (IMB-CNM) [87]. This chapter presents the sensors description and the electrical characterization results. Once the devices are electrically characterized, a dedicated study on the charge division along the electrode was done using a near infrared laser.

Every new device requires a specific noise study, specially when it includes new resistive components that can affect the signal to noise ratio. The signal to noise ratio is studied with a ^{90}Sr radioactive source.

Finally, some alternative configurations using the same resistive charge division concept are presented. At the end of the chapter, a summary of the results, as well as some guidelines to continue this work are provided.

4.1 Resistive charge division in microstrip detectors

4.1.1 Resistive charge division

The resistive charge division method has been frequently used in gaseous detectors with resistive anodes [58, 113–115] and studied for silicon pad detectors [116], but until now it was not implemented in silicon strip detectors.

The basic characteristics of the charge division concept for resistive electrodes was first formulated by Radeka [58] who concludes that the position resolution is determined only by the electrode capacitance and not by the electrode resistance, assuming a readout electronics with the optimal shaping time.

Recently, the use of the charge-division method in very long microstrip sensors -several tens of centimeters- has been proposed as a possible tracking technology for the ILC [11]. Along this application line, the behavior of a detector equivalent RC network implemented on a PC board [117] was used for the benchmarking of a SPICE electronic circuit emulation [118]. The PC board was stuffed with discrete components with electrical specifications matching the main electrical parameters of such long microstrip detectors. The simulation, supported by the RC network measurements, confirmed the overall validity of the Radeka formulation on resistive charge-division.

4.1.2 Description of the prototypes

Several wafers were processed at IMB-CNM. Each wafer includes four different microstrip sensors, one of which is a strip sensor with resistive electrodes (2D position-sensitive sensor) and different test structures to characterize electrically the production (see Figure 4.2). Two different 2D position-sensitive sensor prototypes were produced with different electrode resistivities in order to study their possible influence in the sensor performance. Each sensor has 384 p^+ strips (20μm wide and 2 cm long) with a pitch of 80 μm on a 285 μm thick n-type substrate.

The new microstrip sensor has the same structure of a standard sensor with the same geometry but with resistive instead of metallic (Aluminum) electrodes which are readout from the two electrode ends (instead of just one end as in the case of standard microstrip sensors).

In Figure 4.3 a schematic sensor top view and lateral cross section along one strip are shown. The resistive electrodes that collect the signal are represented in yellow and are made of a thin layer of highly doped polycrystalline silicon, and in blue are represented the readout contacts and the bias ring, both made of Aluminum. In Figure 4.3b, the decoupling structure (silicon dioxide layer in grey) between the resistive electrode and the detector diode

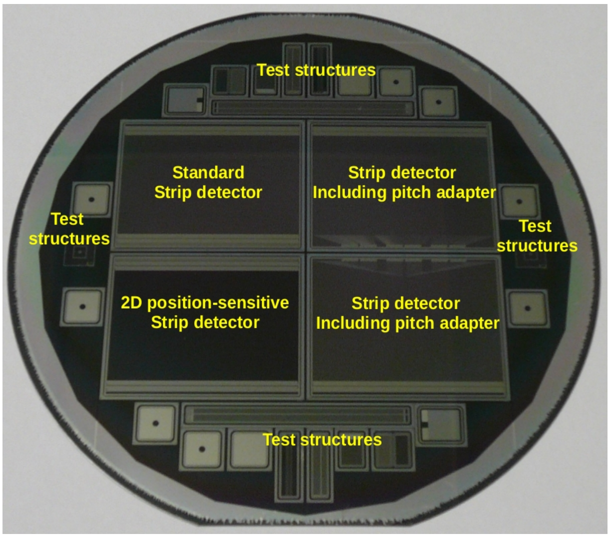

Figure 4.2: *Picture of one produced wafer. The 2D position-sensitive strip detector is on the left-bottom corner of the wafer.*

junction (p-implant in pink, n-bulk in white) is shown. The ohmic contact is shown in green at the backplane of the sensor.
The field of application of this device expands beyond tracking for the nuclear or particle physics, reaching other areas as laser based position sensitive devices, heavy ion physics, beam monitoring in medical applications, etc.

4.1.3 Effect of the resistive electrodes on the detector response

In a conventional microstrip detector the metallic contacts of the strips extend over most of the length of the implants and each strip is connected to a single read-out channel. When an ionizing particle crosses the detector, the propagation of the induced signal along the coupling electrode does not suffer a significant attenuation, i.e., the signal amplitude does not depend on the particle hit point along the electrode direction in a sensible way. When using a resistive electrode instead of a metal, the signal undergoes a significant attenuation during its propagation along the electrode direction. The longer the propagation length is, the larger the signal attenuation becomes. By comparing the recorded signal amplitude at both ends of the coupling electrode one can derive the particle hit point along the electrode direction. In

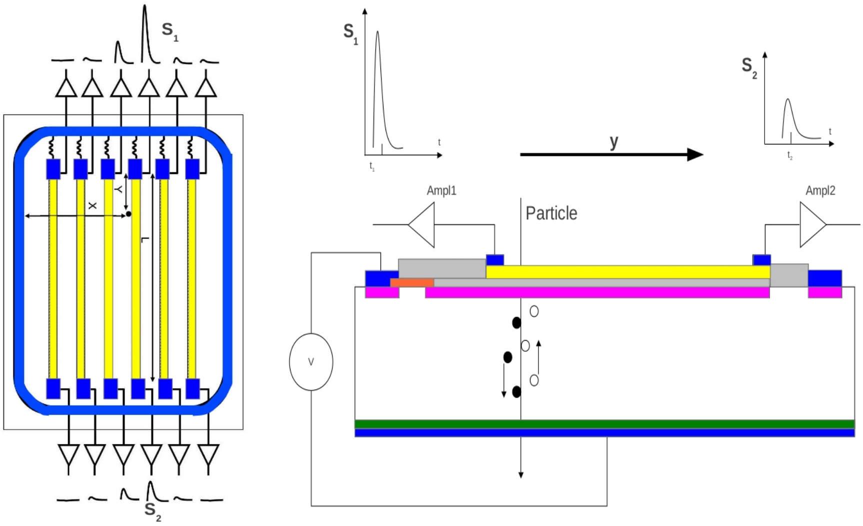

(a) (b)

Figure 4.3: *Novel 2D position-sensitive microstrip sensor. (a) Schematic top view of the novel detector and (b) lateral cross section (not to scale). In blue are represented metallic contacts and in yellow are the resistive electrodes visible in both pictures (see detailed description in text).*

this way a conventional manufactured microstrip sensor can provide the two-dimensional coordinates of the particle hit point; the transversal coordinate derived thanks to the usual electrode segmentation and the longitudinal coordinate determined by comparing the signal amplitude at both ends of the electrode.

The resistive electrode behaves as a diffusive RC line, in which a current pulse undergoes not only an amplitude attenuation but also an increase of its rise time the further it travels. Using a readout electronics characterized by a short rising time compared to the RC constant of the line translates into a non constant signal ballistic deficit. Increasing the electrode resistance also increases the readout serial noise contribution. Both the ballistic deficit and the serial noise can be reduced increasing the shaper peaking time; however, a longer peaking time increases the parallel readout noise contribution. In reference [58], Radeka derived the optimal peaking time for a resistive charge division configuration, under the assumption of high electrode resistance compared to the amplifiers impedance and long amplifier peaking time compared to input signal rise times. He concluded that the position resolution achieved with the resistive charge division method should be independent of the electrode resistance, depending only on detector capacitance and signal amplitude.

Under these assumptions, we expect a linear dependence between the longitudinal coordinate of the particle position and the fractional signal amplitude read from one side of the strip. Following Figure 4.3 notation with A_1 and A_2 the amplitudes of S_1 and S_2 respectively and L is the strip length, the analytical expression to determine the coordinate along the strip (y-coordinate) is given by equation 4.1.

$$y = L \cdot \frac{A_2}{A_1 + A_2} \tag{4.1}$$

4.2 Electrical characterization

The first step after a sensor production is the electrical characterization to know the real parameter values and specifications. To know how is the diode structure, IV and CV curves are measured.

In Figure 4.4 the IV curves are shown in (a). The breakdown voltage is above 300 V for the sensor with less resistive electrodes and above 350 V in case of the sensor with more resistive electrodes. In (b) the 1/C^2 versus voltage curve shows that the $V_{FD} \sim 20V$. In our measurements, an operating voltage of 50 V was used to bias the detector ensuring a maximal depleted volume.

It should be emphasized that the IV-curves give information about the bulk purity and the difference observed in breakdown voltage is not related to the electrodes resistance but to the silicon wafer quality. This is shown in Figure 4.5, where IV curves corresponding to two diodes from different wafers are shown. The current is higher in the wafer that includes the sensors with lower resistance in the electrodes causing a faster sensor breakdown.

Unlike for sensors, no breakdown is observed in diodes. This is because the diode's volume is smaller and because a sensor has a segmented structure that increases the number of field lines in smaller areas (strips), facilitating the multiplication effect which causes the breakdown.

Some other parameters have been obtained from the electrical characterization. They are summarized for each sensor in Table 4.1. All values agree

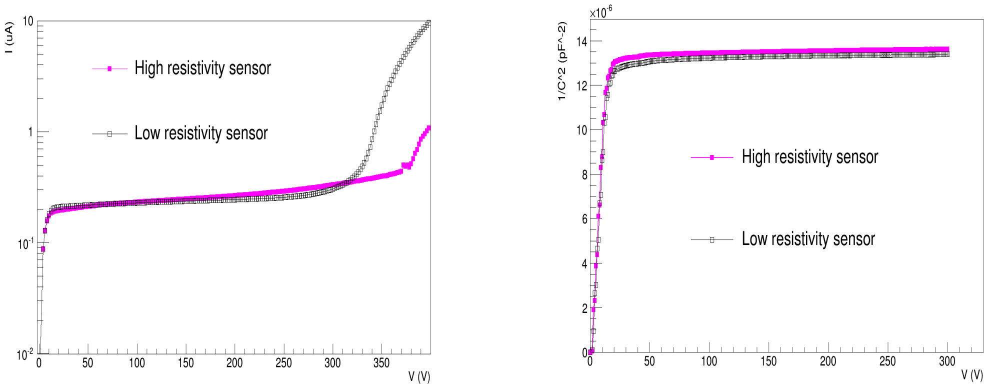

(a)

(b)

Figure 4.4: *2D-position sensitive sensor graphs showing the diode structure performance in the two devices under study. In (a) IV-curves are shown, while (b) shows the $1/C^2$ vs V curve to estimate the full depletion voltage.*

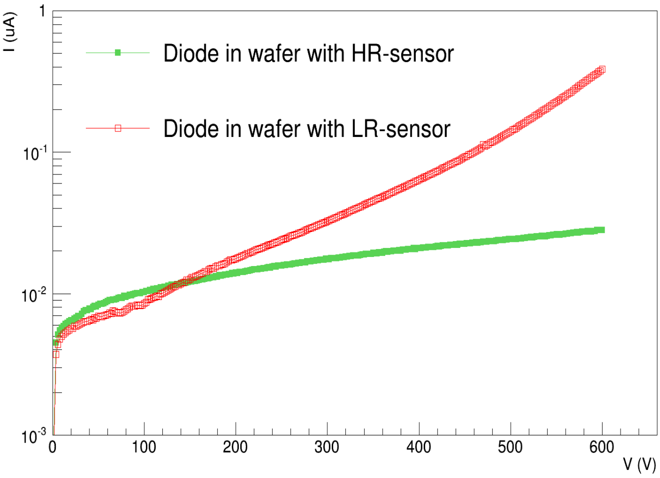

Figure 4.5: *IV curves for diodes in the same wafer and closest to the sensors under study.*

wrll with the designed parameters.

$R_{electrode}$	V_{FD}(V)	V_{bd}(V)	R_{bias} (MΩ)	R_{int}	C_{int} (pF/cm)	C_{AC} (pF/cm)
2.8 Ω/µm	20	∼ 300	4	>GΩ	0.46	189
12.2 Ω/µm	20	∼ 400	2.41	>GΩ	0.46	189

Table 4.1: *Microstrip detector parameters. Electrode resistance ($R_{electrode}$), full depletion voltage (V_{FD}), breakdown voltage (V_{bd}), bias resistor (R_{bias}), interstrip resistance (R_{int}), capacitance (C_{int}) and coupling capacitance (C_{AC}).*

4.3 Laser Characterization

4.3.1 Readout electronics

For our study, no dedicated analog signal processing electronics was built and therefore the front-end filtering of the signal was non-optimal; no effort was made to optimize the shaper peaking time accordingly with the detector time characteristic, i.e., the time characteristic of the RC propagation line equivalent to the detector strip. We used the Alibava daq [95] system developed within the framework of the CERN RD50 collaboration. The analog front-end of the ALIBAVA system is based on the Beetle readout chip [119] used for the microstrip sensor readout of the silicon tracking subsystem of the LHCb experiment at LHC; consequently, the analog front-end shaper peaking time of the Alivaba system is set around 25 ns. Figure 4.6 shows a photo of one of the detectors mounted on the Alibava daughter board.

4.3.2 Model and simulation of the detector

A SPICE model of the detector and the readout electronics have been developed to study the possible effect of the non-optimal shaping time on the linearity of the position dependence ons ignal amplitude (equation 4.1). A simulated current pulse was injected at different points along the strip length and its response was studied. The model was built starting from reference [120] using standard components from the AnalogLib library of Virtuoso Spectre by Cadence [121]. Five consecutive strips have been modeled composed from 80 different unit cells, each one corresponds to a section of 250 µm of the strip length. The unit cell is formed by different capacitances and resistors that represent the main electrical characteristics of the device. R_{sub} and C_{sub} describe the substrate, R_{int} and C_{int} the interstrip parameters, C_{AC} the coupling

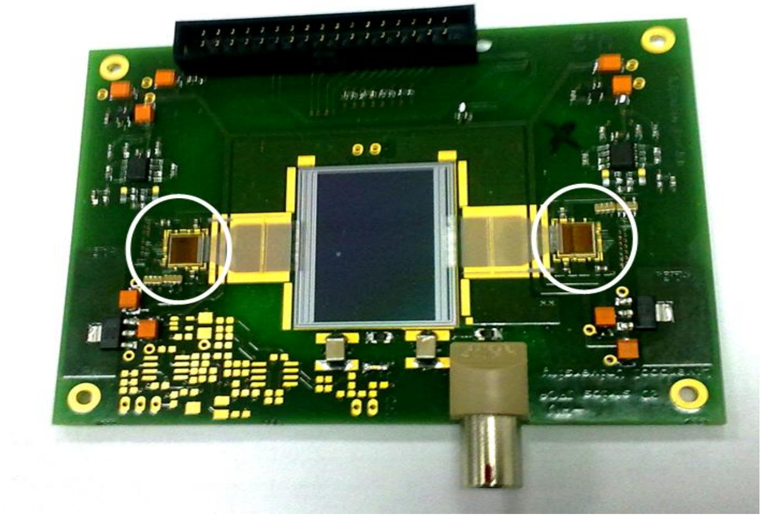

Figure 4.6: *Photo of one of the detectors mounted on the Alibava daughter board, the two Beetle chips are indicated with white circles. Each one reads out the same 128 consecutive strips providing double-sided readout.*

capacitance and finally, the implant and electrode resistances are represented by R_{imp} and R_{el}, respectively.

Figure 4.7 shows the schema of a unit cell. Five different strips can be distinguished. The values of the circuital elements have been determined from the ones measured during the electrical characterization of the detectors over full depletion (V_{bias} = 50 V) and of the test structures to reproduce as close as possible the sensor behavior.

The model of the readout electronics connected to the ends of each strip emulates a generic charge sensitive preamplifier followed by a CR-RC filter whose peaking time matches the Beetle chip peaking time ($\sim$ 25 ns). A schema of the readout chain is shown in Figure 4.8. Once the sensor and the readout chain are modeled, the input signal has to be modeled as well.

In Figure 4.9, the shape of the simulated input signal along the strip length is shown. It has a rise time of 2 ns (similar to the laser pulse rise time) and a total integrated charge of 4 fC.

In the simulation, the signal was injected in different nodes along the implant line (see Figure 4.7) on the central strip in 2 mm steps. The signal that arrives into the preamplifier entrance was recorded for every injection point

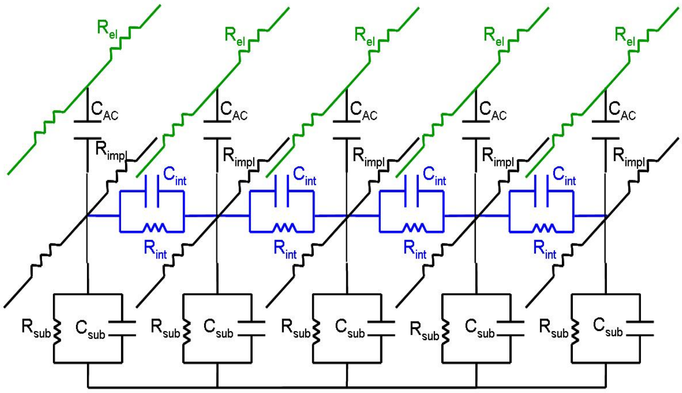

Figure 4.7: *Schematic of one of the 80 cells used to model the detector. One cell represents 250* µ*m of all the five strips together. Al the components representation is clarified in the text.*

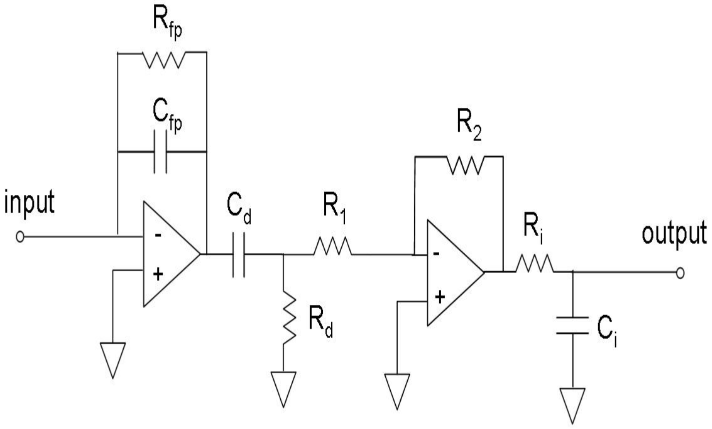

Figure 4.8: *Schematic of the modeled front-end. The parameter values were chosen in order to have a* $\tau_p \sim$ *25 ns.*

and for both prototypes. Results are presented in Figure 4.10.

The linear dependence of the position along the strip on the fractional

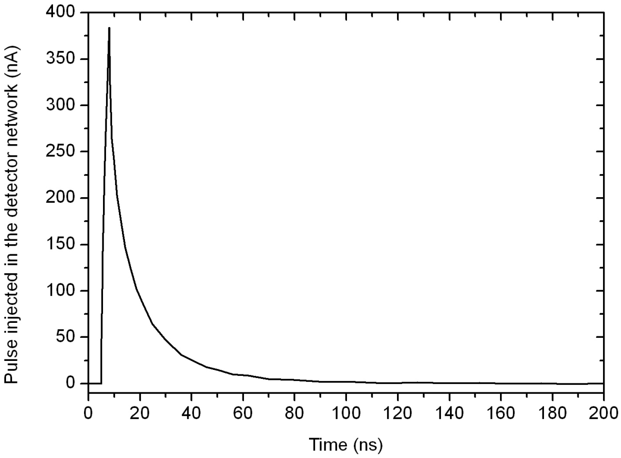

Figure 4.9: *Simulated signal input.*

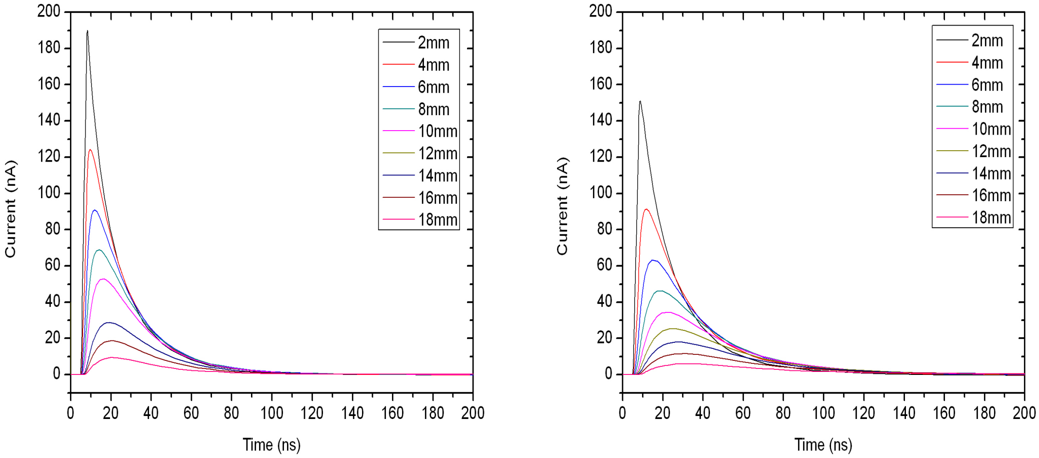

(a)

(b)

Figure 4.10: *Attenuation of the signal read at the entrance of the preamplifier. Results are shown for different positions of the pulse generator along the strip for* $R/l = 2.8\Omega/\mu m$ *(a) and* $R/l = 12.2\Omega/\mu m$ *(b).*

signal amplitude is clearly seen in figure 4.11. According to equation 4.1, with A_1 and A_2 the amplitudes read at the first and the last cells of the

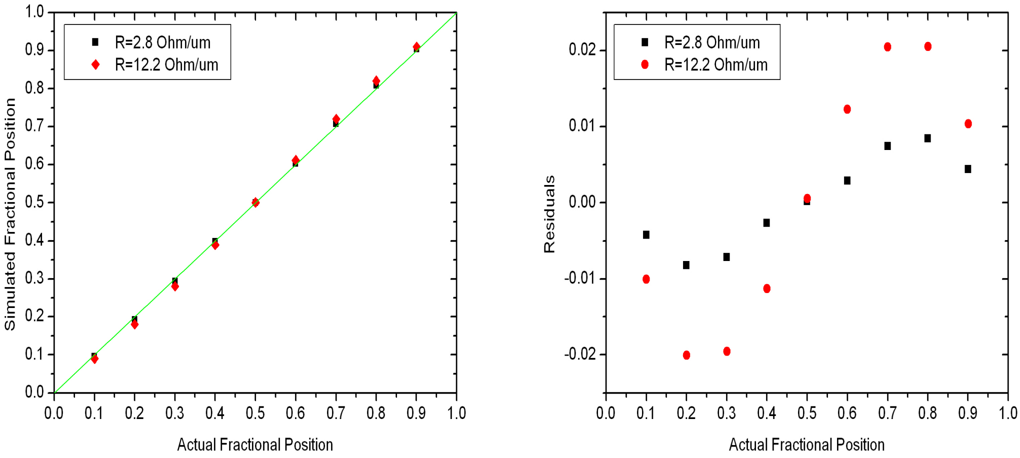

(a) (b)

Figure 4.11: *(a) Simulated fractional position against the actual one (given by the micrometric stage) for both values of electrode resistivity. Values are compared with the linear prediction (green line). (b) The residuals plot shows how as higher electrode resistivity more separation from the linear behavior in the sensor response is obtained.*

strip respectively, the derived fractional position ($\frac{A_2}{A_1+A_2}$) versus the injection fractional position ($\frac{y}{L}$) is shown in Figure 4.11 (a). The data related to the more resistive prototype reveal a clear separation (lager residuals spread in Figure 4.11) from the ideal values due to the ballistic deficit which increases with the distance covered by the signal from the point of generation.

It is worth to note also that in the case of the low resistivity prototype, even for the more attenuated pulse, the rise time is around 10 ns, nearly 40% of the beetle peaking time, and therefore the effect of the ballistic deficit in this sensor is highly suppressed.

4.3.3 Laser Measurements

The laser measurements consisted of a longitudinal scan along a polysilicon electrode for each sensor. The polycrystalline silicon that forms the electrodes is transparent to the infrared light, so that allows to test the signal division in the strip.

The analysis of the recorded data was done by modifications of the source

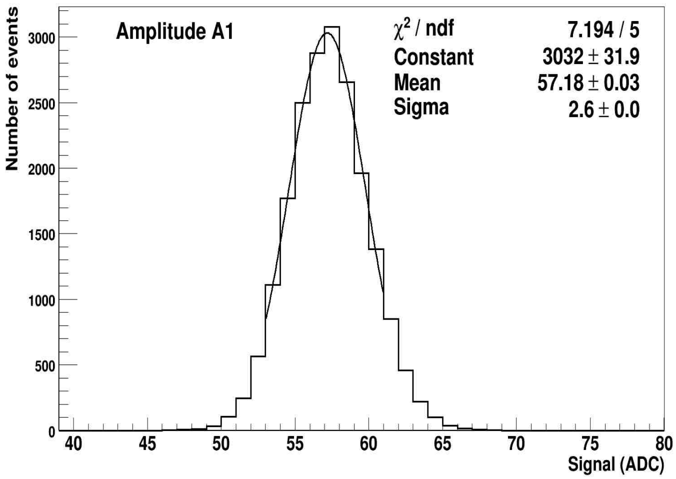

Figure 4.12: *An example of the Gaussian distribution of the sensor signal measured at each point. A point is for a position and a sampling time.*

code supplied by the Alibava system, which is based in ROOT [122].

The Alibava DAQ system does not allow to record the whole shape of the analog signal. On the other hand it allows to reconstruct it thanks to a particular feature that permits to chage the value of the dealy between the trigger time (synchronous with the laser pulse) and the acquisition time (specifying the instant at which the shaper output is sampled) [123]. Setting different delays in steps of 5 ns from 0 to 130 ns the pulse shape can be reconstructed. We recorded 20000 events for each time delay and found the amplitude of their distributions by fitting a Gaussian function to the peak region. In Figure 4.12 one example of one measurement is shown; for every beam position, 26 measurements of 20000 events were taken, one for each sampling time.

The reconstruction of the pulse shape for every scan position is shown in Figure 4.13. In this case we show only results for S1, for S2 the behavior is the same but opposite (signal is growing in amplitude and decreasing in rise-time).

To show clearer the effect of the electrode resistivity on the pulse peaking time, Figure 4.14 shows the peaking time increment as a function of hit position along the strip. In case of the less resistive electrode the increment is about 10 ns, while in the prototype with higher resistivity electrodes the

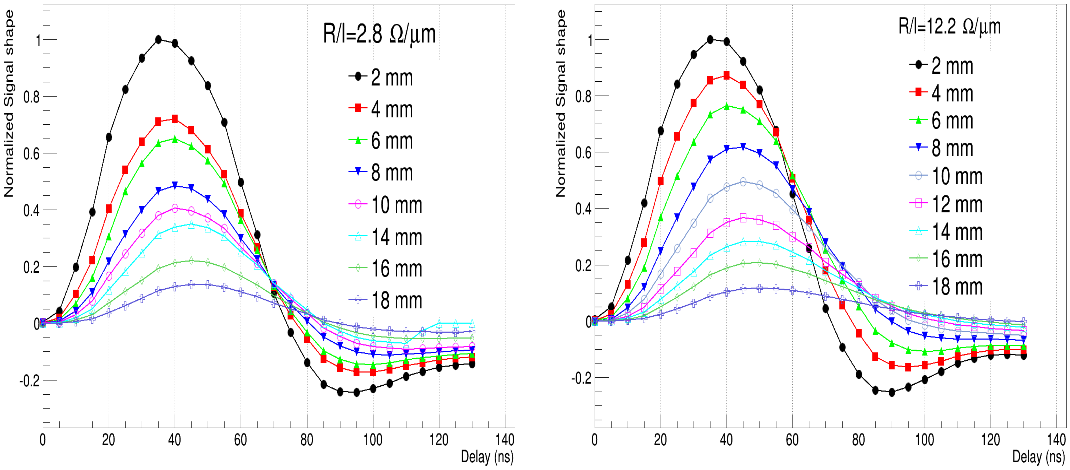

(a) (b)

Figure 4.13: *Reconstructed pulse shapes -normalized to the maximum- along the strip length where the signal attenuation is clearly visible as well as the increasing peaking time. (a) Prototype with R/l= 2.8 Ω/µm and (b) Prototype with R/l = 12.2 Ω/µm.*

increment is about of 15 ns. This is expected from the fact that the larger the attenuation, the larger the rise time and ballistic deficit.

In order to reproduce the results obtained from the simulation, the amplitudes of the reconstructed pulses (see Figure 4.13) have been accurately extrapolated by fitting a Gaussian function to the peak region. Mean and sigma values have been used for the calculation of the fractional position defined by equation 4.1.

Figure 4.15 shows, for both sensors, the measured fractional position of the laser spot against the position given by the displacement of the micrometric stage. The comparison with the ideal linear behavior given by equation 4.1 is shown as well as the comparison with the simulation. We observe the degradation of the linearity of the detector response due to the systematic error introduced by the non-constant ballistic deficit: the higher the electrode resistivity, the larger discrepancy between data and expected values. At this stage, before any noise considerations (it has been considerably averaged out in experimental analysis), the simulation and the experimental data show a

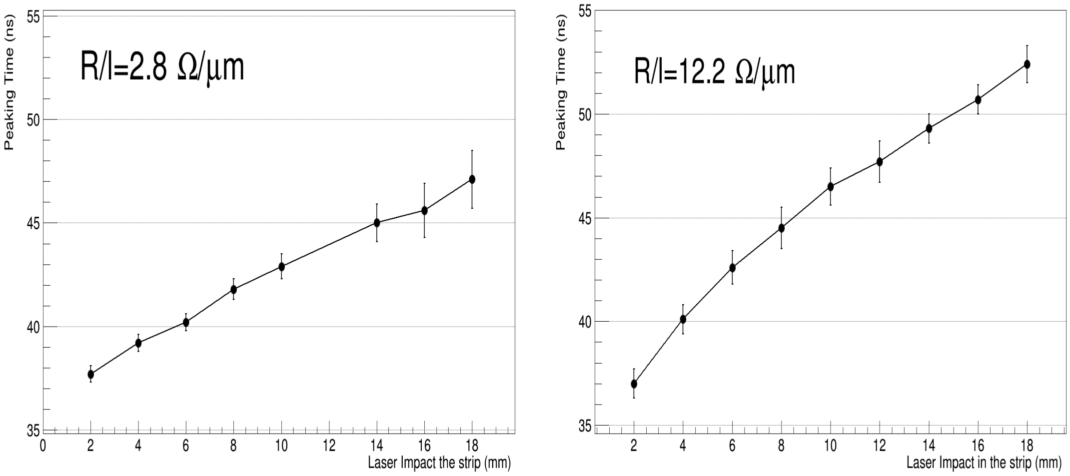

(a) (b)

Figure 4.14: *Peaking time displacement with position. (a) Prototype with R/l= 2.8 Ω/µm and (b) Prototype with R/l = 12.2 Ω/µm.*

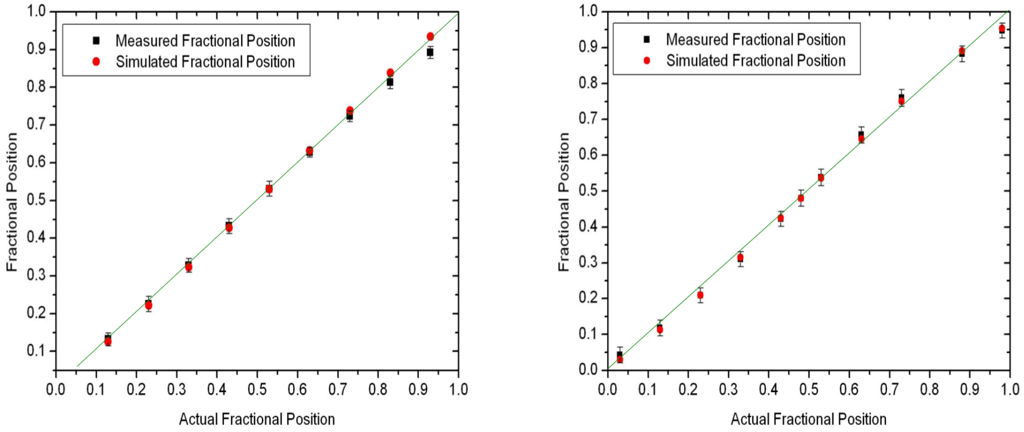

(a) (b)

Figure 4.15: *Experimental results compared with the simulation and the linear case (green line) for both prototypes: (a) R/l= 2.8 Ω/µm and (b) R/l = 12.2 Ω/µm.*

similar systematic behavior.

To show the non-constant ballistic deficit effect more clearly, in Figure 4.16

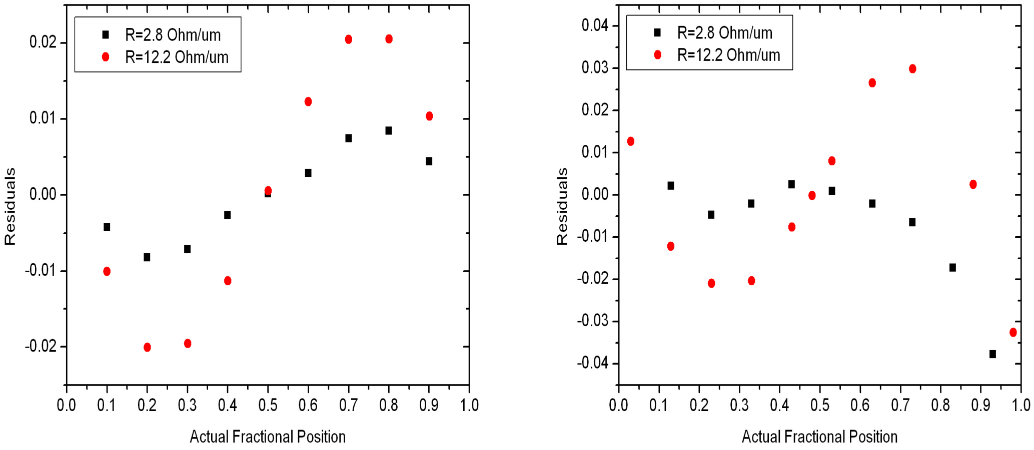

(a) (b)

Figure 4.16: *Residuals obtained from (a) simulated and (b) experimental results for both prototypes.*

the residuals obtained from the experimental and simulated measurements are shown. The sensor with more resistive electrodes show a behavior similar to the one obtained from the simulation, but for the sensor with less resistive electrodes, the residuals differ more from the simulation for larger values of fractional position. This is due to an experimental error that generated a slight progressive misalignment between the stage scanning direction and the electrode.

Simulation and experimental results are in very good agreement showing a similar systematic behavior, confirming that the electrical simulation of the devices is able to reproduce properly the systematic errors due to a non-optimal shaping time. This tools allow to change the electrode resistivity in the simulation in order to optimize the sensor performance.

4.4 Noise sources and its contribution to the position resolution

In this section a summary of the different noise contributions is given.

In these prototypes, each microstrip is readout at both ends independently by a different Beetle chip. As in a standard silicon sensor, each readout channel has a charge sensitive amplifier followed by a shaping stage. The value of the noise for the prototypes under study depends both on the sensor itself and on the signal processing electronics. The most important noise sources are:

- *Amplifier noise* σ_a from the input transistor of the amplifier. This noise varies with the amplifier's input transistor. The most relevant point for this discussion is the fact that this error is *uncorrelated* between the two ends of the sensor's strips because each end has its own amplifier.
- *Thermal noise* σ_R from the resistive electrode. This noise is originated by current thermal fluctuations in the electrode, and is expected to be *anti-correlated* between the two ends of the sensor.
- *Shot noise* produced by the statistical fluctuation of the sensor's leakage current. Due to the external origin of this noise contribution -in the silicon bulk- the noise must be fully correlated between the two ends of the sensor.

Another noise source are the laser intensity fluctuations σ_L among the 20000 pulses recorded at each given scanning position when carrying out the laser-based characterization of the sensor prototypes. This noise is not an intrinsic noise to the detector but is also evaluated in this section given the fact that is has an effect on the fractional position resolution. Its contribution is fully correlated at the strips ends.

4.4.1 Position error estimation

The correlations between the noise contributions affect the position uncertainty, and in this section, this effect is studied in detail.

Given the following definition of position, where A_1 and A_2 are the signal amplitudes at the two ends of the strips:

$$x = \frac{A_2}{(A_1 + A_2)} L \tag{4.2}$$

by error propagation, the following expression for the position uncertainty σ_x is derived, where its explicit dependence with position x, noise amplitude and correlation are shown:

$$\sigma_x^2 = \frac{1}{(A_1 + A_2)^2}[(L-x)^2\sigma_{A2}^2 - 2x(L-x)\rho\sigma_{A1}\sigma_{A2} + x^2\sigma_{A1}^2] \tag{4.3}$$

Using equation 4.3 we can investigate the effect of three different correlation scenarios:

- Fully anti-correlated ($\rho = -1$), caused by the thermal noise contribution.
- Fully correlated ($\rho = +1$), for the laser intensity fluctuations and shot noise.
- Uncorrelated ($\rho = 0$), due to the amplifier noise.

Thermal noise. For this type of noise due to the electrode resistivity, the noise inputs at each end of the electrode have the same magnitude but opposite sign, that is:

$$\Delta A_1 = -\Delta A_2 \ ; \ \sigma_{A1} = \sigma_{A2} \equiv \sigma_A \ ; \ \rho = -1 \tag{4.4}$$

Therefore according to equation 4.3 the thermal noise effect on the position resolution σ_x is independent of the position and it is fixed by the signal to noise ratio as it is given by the following expression:

$$(\sigma_x^{Therm})^2 = \frac{1}{(A_1 + A_2)^2}[(L-x)\sigma_A + x\sigma_A]^2 = \frac{L^2\sigma_A^2}{(A_1 + A_2)^2} \tag{4.5}$$

Amplifier noise. As has been said before this noise is associated to the input transistor of the amplifier, therefore it is uncorrelated and not necessarily of equal magnitude although one should expect that when using similar electronics at both ends the amplifier noises are similar. Under this assumption the position resolution parameters are:

$$\sigma_{A1} \simeq \sigma_{A2} \ ; \ \rho = 0 \tag{4.6}$$

Plugging this into equation 4.3, one obtains:

$$(\sigma_x^{Amp})^2 = \frac{1}{(A_1 + A_2)^2}[(L - x)^2\sigma_{A2}^2 + x^2\sigma_{A1}^2], \tag{4.7}$$

a contribution to the position resolution that depends quadratically on the distance. If we assume that $\sigma_{A1} \simeq \sigma_{A2} \equiv \sigma_A$ we obtain a symmetric quadratic dependence:

$$(\sigma_x^{Amp})^2 = \frac{L^2\sigma_A^2}{(A_1 + A_2)^2}(1 - 2\frac{x}{L} + 2\frac{x^2}{L^2}) \tag{4.8}$$

Thus the position error induced by the amplifier noise is a square root of two larger at the ends of the strip than at the center of the strip. Amplifier noise depends on the impinging point: the farther the signal to the amplifier, the higher the noise contribution.

Intensity fluctuation of laser pulses. This contribution is fully correlated, it comes from an external source and its noise parameters are given by equation 4.11:

$$\sigma_{A1}^{Laser} = \beta A1 \ ; \ \sigma_{A2}^{Laser} = \beta A2 \ ; \ \rho = 1 \tag{4.9}$$

where β is a positive constant which characterizes the laser stability. Applying these parameters to equation 4.3, equation 4.10 is obtained, where it is shown that the laser intensity fluctuation does not have any contribution to the position measurement uncertainty:

$$(\sigma_x^{Laser})^2 = \frac{\beta^2}{(A_1 + A_2)^2}[(L - x)A_2 - xA_1]^2 = \beta^2[(L - x)x - x(L - x)]^2 = 0 \tag{4.10}$$

Shot noise. The statistical fluctuations of the leakage current is the cause of this noise contribution. As in the case of the laser, this noise has to be fully correlated if we assume that both ends are sensitive to the same increase or decrease of the leakage current. Under this assumption we consider the following resolution parameters:

$$\frac{\sigma_{A1}}{\sigma_{A2}} = 1 \ ; \rho = 1 \tag{4.11}$$

Applying these parameters to equation 4.3 we obtain:

$$(\sigma_x^{Shot})^2 \ = \frac{1}{(A_1 + A_2)^2}[(L - x)\sigma_{A2} - x\sigma_{A1}]^2 \ = \frac{\sigma_{A1}^2}{(A_1 + A_2)^2}(L - 2x)^2 \tag{4.12}$$

Thus, as in the case of the amplifier noise, the shot noise introduces a quadratic dependence with the position, in this particular case being zero at the center of the electrode and maximal at the edges.

4.4.2 Measured noise in prototypes

In this section, only results for the prototype with higher resistivity are presented. In this prototype characterization no alignment problems were detected along the longitudinal laser scan.

Taking into account the previous study, the following contributions are expected:

- Amplifier and shot noise contributions have a quadratic dependence.
- Thermal noise contributes with a constant value.

Measuring the noise directly in the detector without a laser beam hitting on it, the pedestal distribution was extracted. In Figure 4.17 distributions for both strip readouts are shown. The noise, defined as the width of the pedestal, have values of 1.83 and 1.8 ADC counts for A_1 and A_2 readout channels for the same strip. In Figure 4.18, the correlation plot between A_1 and A_2 noise is shown. The value of the correlation factor (ρ) is 0.03, which means that the uncorrelated noise contribution (from the amplifier) dominates in the total noise value.

To evaluate the noise contribution with laser presence and its dependence with the hit position, the width of the distribution of the signals along the longitudinal scan are studied, and results are shown in Figure 4.19. The further the laser spot is moved from the A_1 readout end, the further the noise

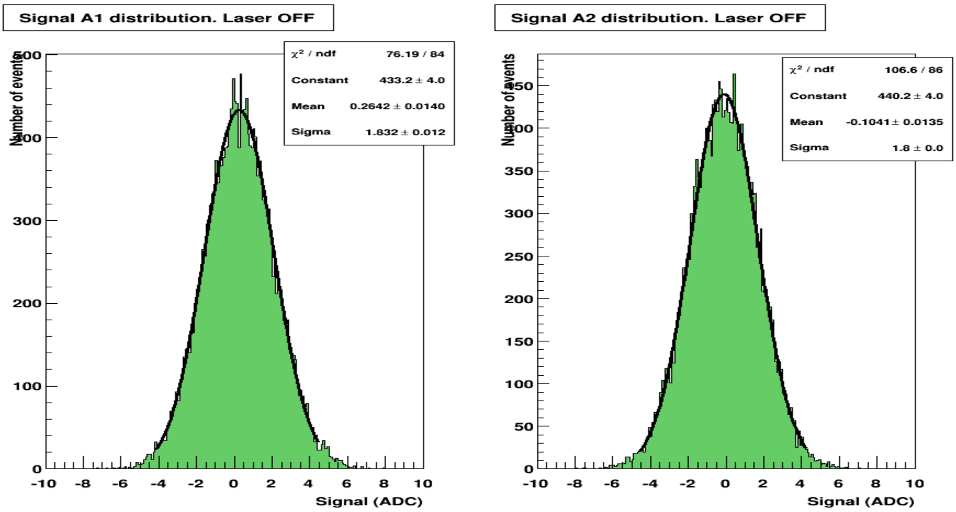

Figure 4.17: *Raw distributions of pedestals for A_1 and A_2.*

is reduced. The laser contribution to the noise decreases linearly as $\frac{x}{L}$ increases, until the other noise components -amplifier, shot and thermal- start becoming relevant and the noise value saturates to the minimal value that was obtained from the pedestal distribution $\sim$ 1.8 ADCs. Therefore, the mean values for the spatial resolution obtained with a laser beam is around 1.1 % of the total strip length (1.2 % in case of the low resistivity electrodes detector).

The study of the correlations shows that the dominant noise source is the amplifier noise. This explains the similarity between spatial resolutions for the two prototypes (with a factor 4 difference between electrodes resistivity, but with the same capacitive components). To improve the spatial resolution, one must decrease the input capacitance into the amplifier (or reduce the amplifier noise). The main capacitance component in the amplifier input is the interstrip capacitance, which depends on strip-width/pitch ratio. If those parameters are changed, it must be done taking into account its effects on the full depletion voltage and on the spatial resolution in the transverse coordinate.

Another important parameter is the shaper time constant that is proportional to the detector time constant and hence to the rise time of the pulse that travels along the electrode. Therefore, the shaper time must also be taken into account in order to avoid the ballistic deficit.

From the point of view of the detector performance, the best results will be achievable choosing the electrode resistance in such a way that the detector time constant is kept small and making the the total capacitance of the detector as small as possible, while keeping the other characteristics of the device unchanged as much as possible.

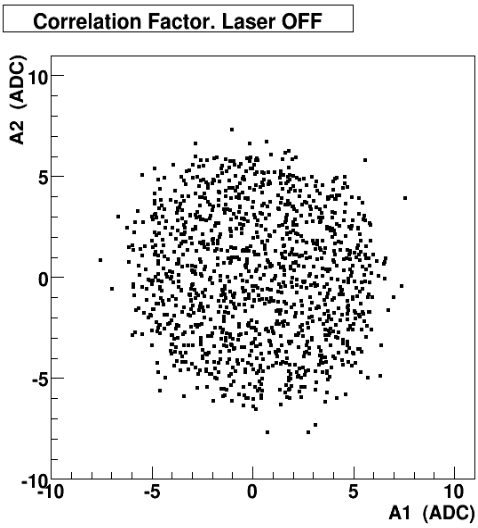

Figure 4.18: *Raw pedestal data for both signals* A_1 *and* A_2*. Correlation parameter* ρ*= 0.03.*

The change in the relative contribution of each of the noise components is shown in the dependence of the correlation coefficient with the laser scan position. Figure 4.20 shows how the correlated noise contribution increases in the strip center (laser fluctuations and shot noise).

Estimation of the measured position error The position measurement error was estimated in two different ways:

- In a direct way. Considering the width of the distribution of the variable x/L (defined as in equation 4.2) measured from the 20000 laser pulses at every scan position as the position error.
- In an indirect way. Using equation 4.3, propagating the uncertainty on the measurement of the signal amplitudes and including the measured correlation factor for each scanning point.

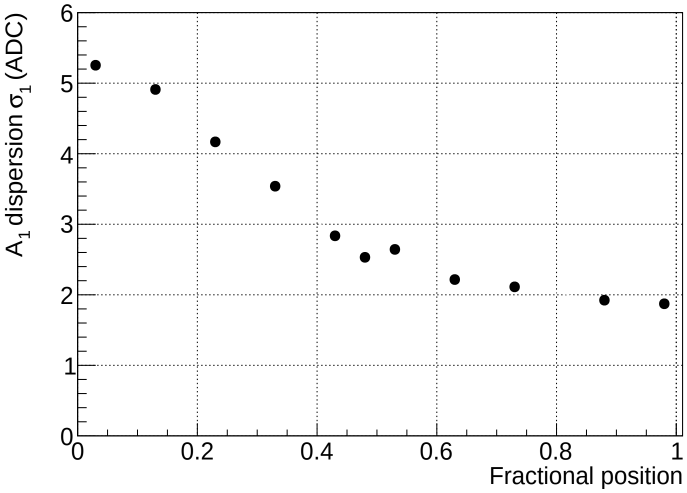

Figure 4.19: *Noise values for the A_1 signal along the strip scanning points.*

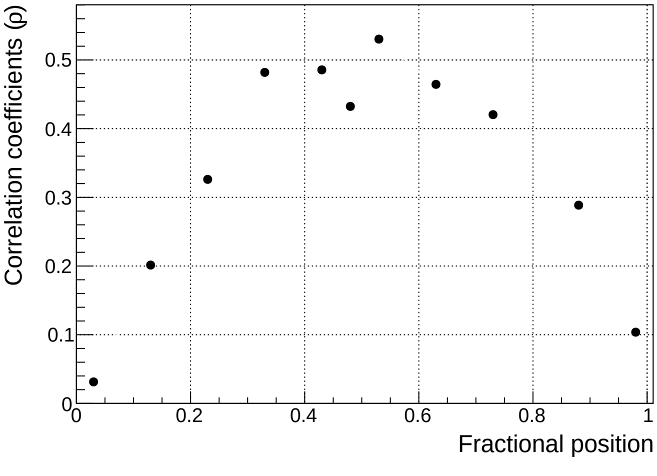

Figure 4.20: *Correlation coefficients ρ at the different scan points.*

Results obtained in both ways are presented in Figure 4.21. As expected, a minimum of the error around the center of the electrode is observed while the maximal error is given for those measurements near the strip ends. As a consistency test, the error estimated using both methods have almost identical values.

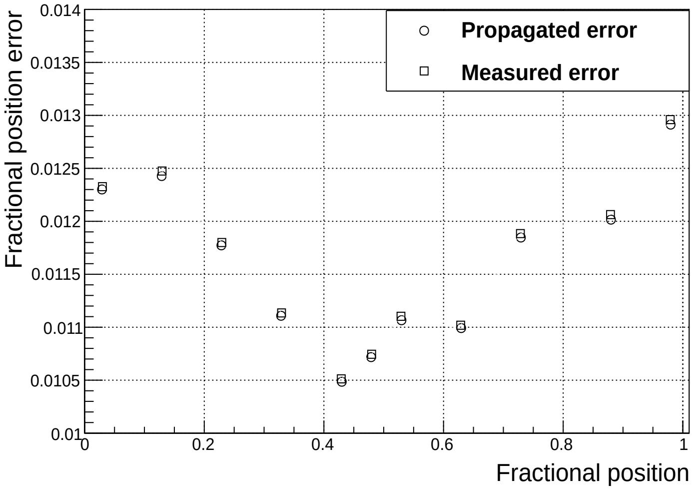

Figure 4.21: *Fractional position measurement error at each scanning point.*

4.5 Signal to noise evaluation

To evaluate the signal to noise ratio (S/N) in 2D position-sensitive sensors, they have been tested under a ^{90}Sr radioactive source. In Figure 4.22 the obtained signal to noise ratio distribution for the prototype that has lower electrode resistivity is shown. We can see that the most provable value for the Landau function fit is around 12, which is quite smaller than the expected in standard sensors (~ 20). This is due mainly to the ballistic deficit; amplitude attenuation and increasing of the rise time along its way to the readout pad, both effects cause that the sampling time does not match with the pulse peaking time. In terms of the detector design, to decrease the noise as much as possible, the interstrip capacitance has to be reduced while keeping a proper sensor performance.

4.6 Prototypes with integrated signal routing lines

In the framework of the International Linear Collider Experiments, the Silicon Detector experiment (SiD) design implements long ladders of strip detectors [124]. Silicon microstrip sensors are connected end-to-end ending up into a very long microstrip sensor. In this detector structure becomes very difficult

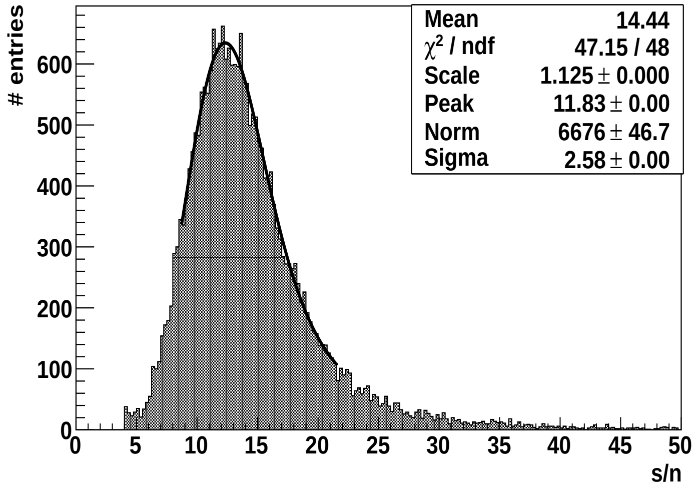

Figure 4.22: *Signal to noise distribution in a 2D position-sensitive sensor.*

V_{FD}(V)	V_{bd}(V)	R_{bias}	R_{int}	C_{int} (pF/cm)	C_{AC} (pF/cm)	R_{el} (Ω/µm)
40	> 400	1.31 MΩ	>GΩ	0.6	173	20

Table 4.2: *Measured electrical parameters of the detector prototype.*

to get two dimensions coordinates information. A possible solution is using resistive electrodes and reading out the signal at both strip ends.

A prototype with integrated signal routing lines was designed and fabricated. In this way, the signals from both strip ends are readout in the same sensor end allowing clustering algorithms in the readout chip. The sensor consists of 34 p^+ strips (20 µm wide and 1.4 cm long) with a pitch of 160 µm on a 285 µm thick n-type substrate. The electrode's resistance in this prototype is of R/l= 20 Ω/µm (another sensor was manufactured with the same layout but with a strip width of 40 µm. This sensor did not work after the detector module manufacturing). A metallic via (Aluminum) is used to drive the signal from one end of the strip to the opposite end of the detector (see Figure 4.23); therefore, all the contact pads are in the same area of the detector allowing both ends to be readout by one single ASIC.

The sensor was also electrically characterized and the main parameters are listed in table 4.2.

The prototype was benchmarked against an electrical simulation (see sec-

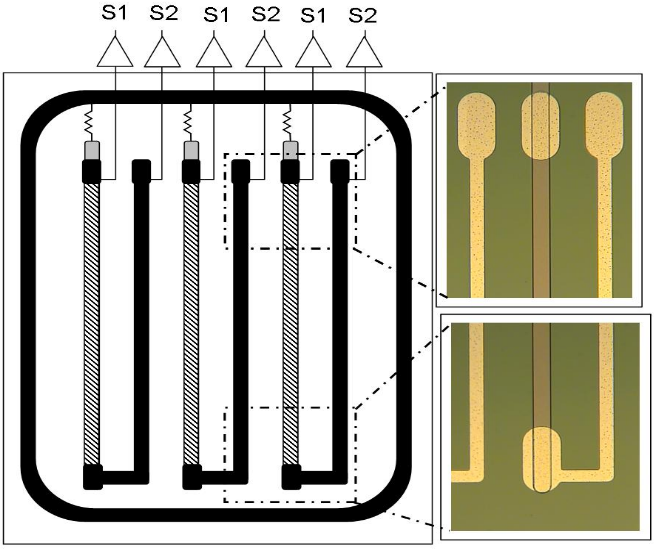

Figure 4.23: *Left: Schematic top view of the new prototype. Black colors reefer to aluminum structures and striped areas are the resistive electrodes on the strips. The strip implant pitch is 160 μm while the readout pitch is 80 μm due to the Aluminum vias. Right: Two detailed photographs of the two ends of one strip.*

C_{int} (fF)	C_{AC} (pF)	C_{sub} (fF)	R_{sub} (GΩ)	R_{imp} (Ω)	R_{int} (GΩ)	R_{el} (Ω)
24	3.43	16.6	20000	800	15	2500

Table 4.3: *List of values used in the simulation of the sensor's equivalent circuit.*

tion 4.3.2) of the equivalent circuit using as input the parameters obtained after the electrical characterization. The values shown in table 4.3 are given by cell (2.5 mm length and in case of strip parameters considering 20 μm wide).

The aluminum routing lines were not included in the simulation. One would expect that the possible disagreement between the measurements and the simulation may be originated by the effect of the routing lines.

The experimental procedure followed with this new sensor was the same described in section 4.3.3, scanning longitudinally the strip with the laser spot in 2mm steps, reconstructing the pulse shape at the output of the front-end electronics for each position and calculating the fractional position given by the signal amplitudes. Figure 4.24 shows a photo of the Alibava daughter

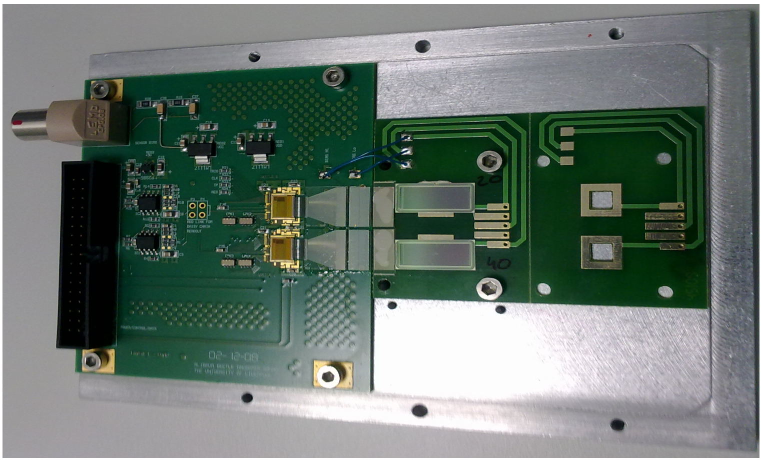

Figure 4.24: *Alibava Daughter board reading two prototypes including the Aluminum routing, each one connected to a single Beetle readout chip. Two pitch adapters and Beetle readout chips are visible.*

board with two of these prototypes, each one connected to a single readout chip.

Figure 4.25 (a) shows the schematic of the measurement in a point (close to the middle) and (b) the obtained results. When we impact in the middle of the central strip we should not have signal in $S2_L$ but we can see clearly that we have an induced signal on it. We can ensure that it is not a direct signal, because in that case, a similar signal would be readout in $S1_L$.

In Figure 4.26 the measured fractional position is shown together with the simulated results. The ballistic effect is again present (deviation from the linearity), but also a clear discrepancy between experimental and simulated behaviors. Looking at Figure 4.25 and considering that the scan starts in the $S1_C$ end of the strip, the discrepancy between experimental and simulated results can be explained by an excess in $S2_C$ due to the induced signal in the metal guide and caused by a parasitic capacitance between the metal guide and the strip. This effect is more relevant for impacts close to the $S1_C$ readout, where $S2_C$ is expected to be small.

Looking at these results, a good isolation between the strips and metal routing becomes crucial in order to improve the position resolution and to facilitate the signal understanding.

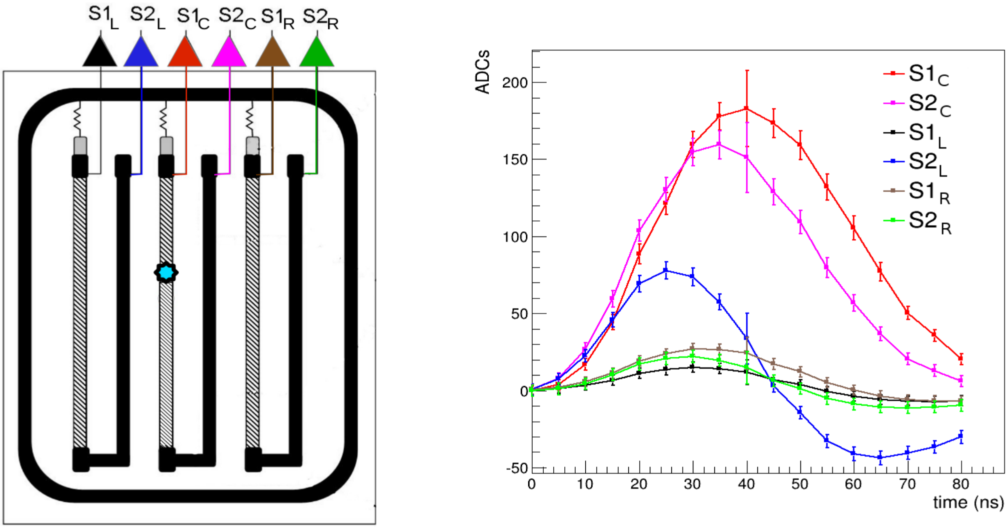

(a)

(b)

Figure 4.25: *Schematic of the measurement and results. (a) shows a three-strip layout and the signal labels, the laser impact is illustrated close to the middle of the strip in light blue. (b) shows the signal shapes where the induced charge in* $S2_L$ *is clearly visible (blue).*

4.7 Study of parasitic couplings

In order to understand and to avoid the parasitic couplings measured in the previously described prototype, a deeper study will be done in new sensors with dedicated layouts. The main objective of this study is to allow the readout of a two dimensional position-sensitive sensor from the same sensor side avoiding the induced signal that can complicate the signal analysis.

New sensors have been fabricated at CNM-IMB, each one including six small 2D position-sensitive sensors. They have an area of 25 x 8 mm^2 (4 devices) and 25 x 6 mm (2 devices), have 34 and 20 strips respectively, with a 160 µm pitch and a length of 2.2 mm. The resistivity of the electrode is given by R/l = 2 Ω/µm, that is slightly less resistivity than previous prototypes. New prototypes main characteristics:

- P-stop. These sensors are n-on-p instead of p-on-n. They require an extra isolation of the n-type electrodes that has been done using the "at all" p-stop technique. This technique consists of the use of a p-type

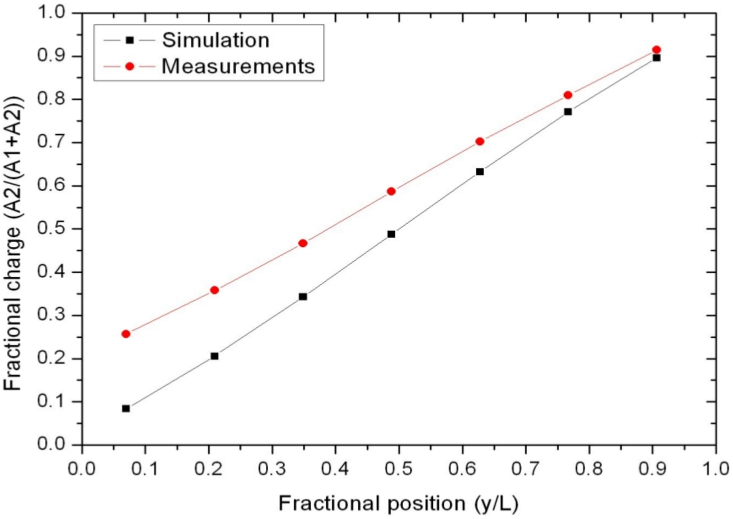

Figure 4.26: *Measured fractional position compared with the simulated one.* A_1 *and* A_2 *are the amplitudes of* S_1 *and* S_2 *respectively. The induced signal on the metal guides contributes to signal S2 generating a shift of the experimental measurement with respect to the simulation.*

silicon *"barrier"* surrounding the electrodes.

- Aluminum grid. An aluminum grid for grounding is included (or not) in the design to facilitate the insulation between electrodes and routing lines. Two devices per wafer have a half of the sensor with the grid and the other half without it.

With these new designs, a detailed characterization with the main objective of the study of the parasitic coupling capacitances will be done shortly. In Figure 4.27 pictures of some of the new designs are included.

4.8 Summary

In this chapter, a 2D position-sensitive semiconductor detector has been presented. Its working principle is based on the resistive charge division method and several prototypes have been fabricated using standard AC coupled technology.

The implementation of resistive electrodes allows to extract information on the longitudinal coordinate of an ionizing event.

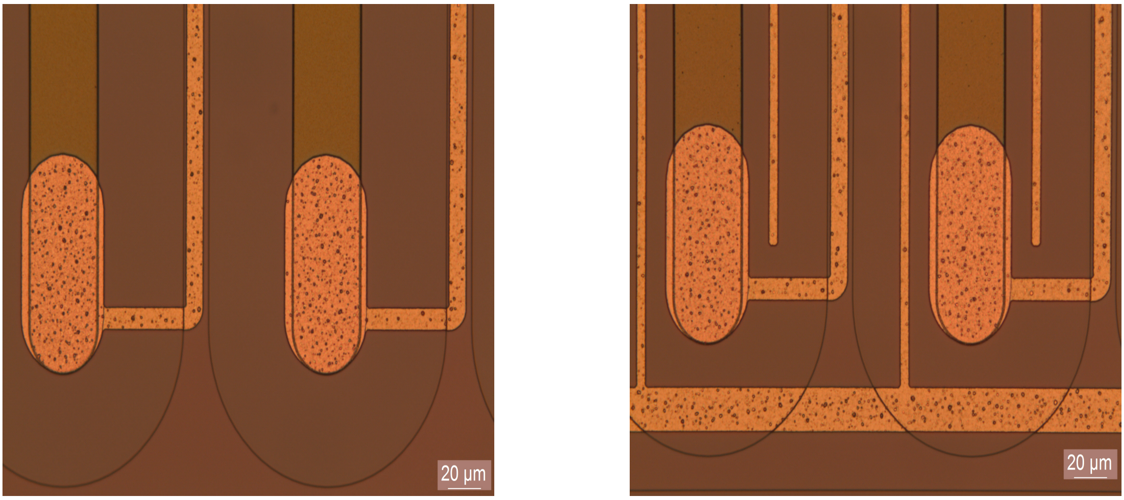

(a) (b)

Figure 4.27: *Pictures of some details of the new designs. (a) In this sample, the p-stop is visible together with the routing line. (b) The same device than in (a) but with an Aluminum grid.*

The performance of two different prototypes with strip lengths of 20 mm, width of 20 µm and different linear resistances of the electrodes: R/l = 2.8 Ω/µm and R/l = 12.2 Ω/µm were studied. The electrical simulations of the detector and front-end electronics are able to reproduce experimental results in reconstructing the fractional position of the signal generation point. This validates the simulation as an adequate tool for future sensor designs.

The sensor performance characterization was done scanning the strip surface with a near infra-red laser. Results show that the position resolution along the longitudinal coordinate for a signal of about 6 MIPs is 225 µm and 232 µm for the low and high resistive electrode sensors, respectively. With the comparison between experimental and simulated measurements, we studied in detail the signal propagation effects which are signal attenuation and the peaking time increases. Both effects cause a systematic non constant ballistic deficit when a non optimized front-end electronics is used to read out the signal.

In terms of signal to noise ratio (SNR), the obtained value is about 10, which is a lower value when compared with typical standard sensor values (∼ 20). To improve this SNR several actions can be taken, the electronic circuitry can be optimized to the proper sampling time, the noise can be reduced decreasing the input capacitance to the amplifier and the signal attenuation can be decreased by tuning the electrode resistance.

The possibility of reading out the detector from only one side was also studied integrating an Aluminum routing line to drive the signal. That prototype showed the importance of having a good insulation between implants with respect to the metal routing to reduce parasitic capacitances and signal leaks.

These detectors have been tested with a pion beam (120 GeV) at the CERN SPS beamline H6. The analysis of the test beam data is ongoing in order to make specific studies of their performance as tracker detectors.

In order to optimize the future prototype fabrication several factors have to be taken into account:

- The detector spatial resolution depends on the signal to noise ratio. Tunning the electronic parameters, the SNR will be optimized when the shaper time and detector time constants are proportional.
- Concerning the detector design, several aspects need to be considered. The interstrip capacitance dominates the input capacitance to the preamplifier. The signal attenuation can be tuned by modifying the electrode resistance. Every design change must be done carefully to avoid resolution detriment.

These parameters can be easily tuned thanks to the simulation tool already developed. Typically the electronic parameters are given by the readout electronics. They can be fixed in the simulation and working on the sensor parameters the final design can be optimized until the desired behavior is reached.

Chapter 5

Characterization of 3D pixel detectors for the CMS vertex detector upgrade

In this chapter, the study of 3D pixel detectors for the phase II CMS vertex upgrade is presented. A brief introduction and description of the sensors is given, followed by the electrical characterization results. The used readout electronic is the same as the one presently used by the CMS pixel detectors and is described in detail in this chapter, as well as the interconnection process used to couple it to sensor. Once the sensor and read out chip (ROC) are connected, the performance of the detector can be characterized. In this study, both a radioactive source and a particle beam were used. Finally, the results are discussed and some guidelines to continue this work are given.

5.1 Introduction

In this introduction a brief description of the current CMS vertex detector and the new detector requirements for its phase II upgrade are given.

5.1.1 The CMS vertex detector

The description of the Run I CMS vertex detector was obtained from [125]. The reader is invited to consult this reference for a more detailed information.

The CMS experiment at the LHC has hybrid silicon pixel detectors forming the vertex detector. This detector is an essential component for reconstructing interaction vertices and heavy quark decays in an environment characterized by very intense irradiation field which translate in very high detector occupancy. The detector consists of three barrel layers and two disks at each end of the barrel. The innermost barrel layer is placed 4.3 cm from the beam pipe, second and third layers at 7.2 and 11 cm, respectively. Each layer is composed of modular detector units. Every module is made of segmented silicon sensors with readout chips connected by the bump bonding technique.

Silicon sensors are of type n-on-n processed on a diffusion oxygenated float zone wafer with a thickness of 285 μm; the pixel size is of 100 × 150 μm^2. They include a bias grid and a pixel isolation by p-spray technique. The choice of the sensors was based on previous works [126–131].

The sensor substrate is highly resistive n-type silicon and the frontside of the sensor is n-doped while the backside is p-doped (see Figure 5.1). The pn and ohmic junctions are placed in the backside and frontside, respectively. To suppress the electron accumulation layer on the front side of the sensor (n-on-n), the p-spray technology is used.

The characterization tests showed that sensors have a high enough signal charge ($\sim 14000e^-$) at ~ 600 V after high hadron fluences ($\sim 1 \times 10^{15}\ n_{eq}/cm^2$). These studies also show that collecting electrons, that have higher mobility, facilitate the charge sharing, therefore the Lorentz angles are larger than for holes collection reaching the required spatial resolution.

In Figure 5.2 a photo of four pixel cells is shown. The sensor surface structure is visible, including a bias structure and p-spray. Every pixel has a bias dot that consists of a circular n-implant isolated from the pixel implant by a small gap. They are connected through an Aluminum line and routed forming a bias grid that provides a bias connection to all pixel cells. This structure facilitates the electrical characterization of the sensor, the sensor can be biased by punch-through and IV curves are measured before the sensor

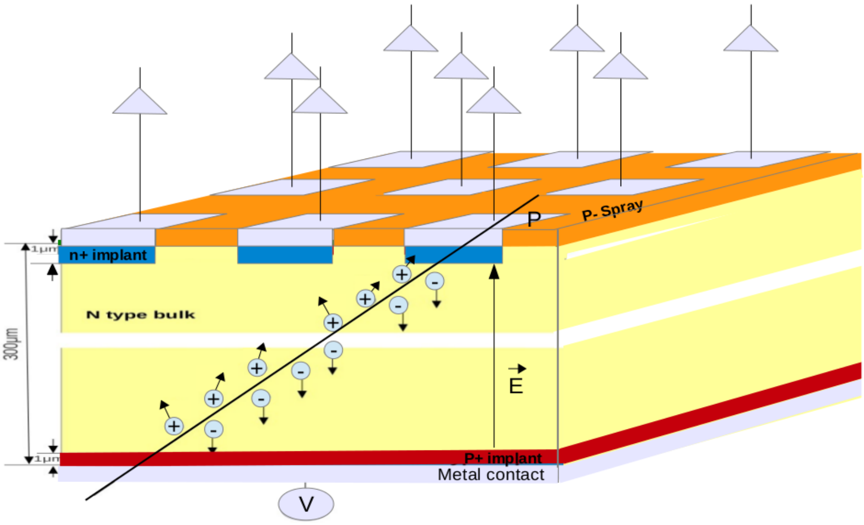

Figure 5.1: *n-on-n pixel sensor structure. The ohmic junction is segmented, grounded and readout while the junction is at the bottom of the device.*

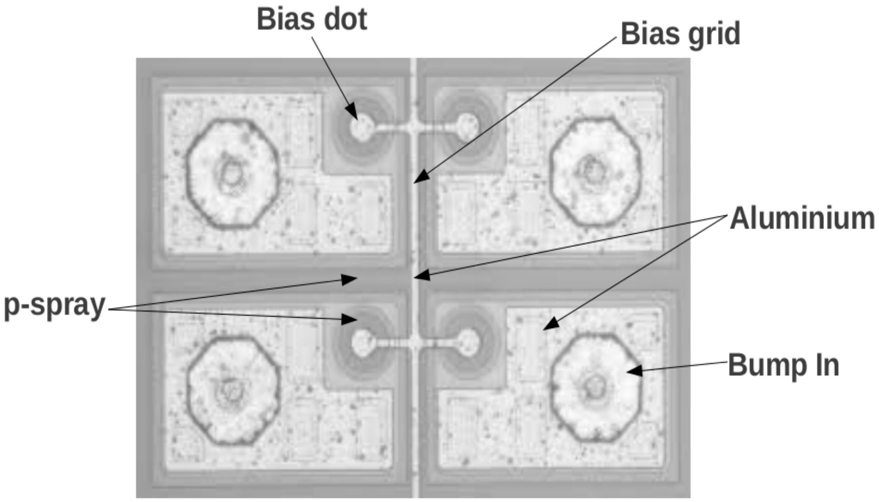

Figure 5.2: *Photo of four pixel cells from the CMS barrel vertex detector [125].*

flip-chip.

To guarantee the homogeneity of material properties, all wafers for the production of barrel sensors come from the same silicon ingot. And to improve the post radiation behavior the wafers undergo an oxygen diffusion process as recommended by the ROSE collaboration [76], resulting in the so-called DOFZ-material.

5.1.2 The vertex Phase II upgrade

The High Luminosity Large Hadron Collider (HL-LHC) is a possible upgrade of the current accelerator (LHC) for which, the luminosity will increase considerably reaching a total integrated luminosity of 3000 fb^{-1} at the end of the running period and the instantaneous luminosity will be of $5{\times}10^{34}\text{cm}^{-2}{\cdot}\text{s}^{-1}$. In this high luminosity scenario, the hadron fluences at the innermost layers of the CMS vertex detector are expected to reach values up to 2×10^{16} n_{eq} $/\text{cm}^2$. Under these hostile conditions, silicon-based vertex detectors will suffer severely from radiation damage, displaying: increase of the leakage current, change in effective doping concentration of the bulk and reduction of charge collection efficiency (see chapter 2).

By reducing the charge carriers collection distance, the probability for getting trapped in one of the radiation-induced defects decreases, as well as the voltage needed to fully deplete the device. In current planar technologies the collection distance is given by the sensor thickness, the drawback of thinner sensors is that the collected charge is reduced as well.

To improve the charge collection efficiency (CCE), one alternative technology are the so-called 3D sensors. These sensors have cylindrical vertical electrodes that penetrate into the detector bulk [73]. Electrons and holes, moving parallel to the sensor surface, are then collected at opposite biased cylindrical electrodes. Minimum drift time and depletion voltage are determined by the electrode spacing. Depending on the electrodes pitch the charge carriers generated by ionizing radiation can be collected within a time smaller than the trapping time of the radiation-induced defects [132].

Studies comparing standard microstrip detectors fabricated in p-type material and 3D strips detectors made in the same type of silicon material [57] have shown the advantage of 3D detectors for fluences up to $2{\cdot}10^{15}\text{n}_{eq}/\text{cm}^2$. In this chapter the results of the characterization of 3D double-sided and double-type pixel detectors before and after irradiation up to $5 \cdot 10^{15}\text{n}_{eq}/\text{cm}^2$ are presented.

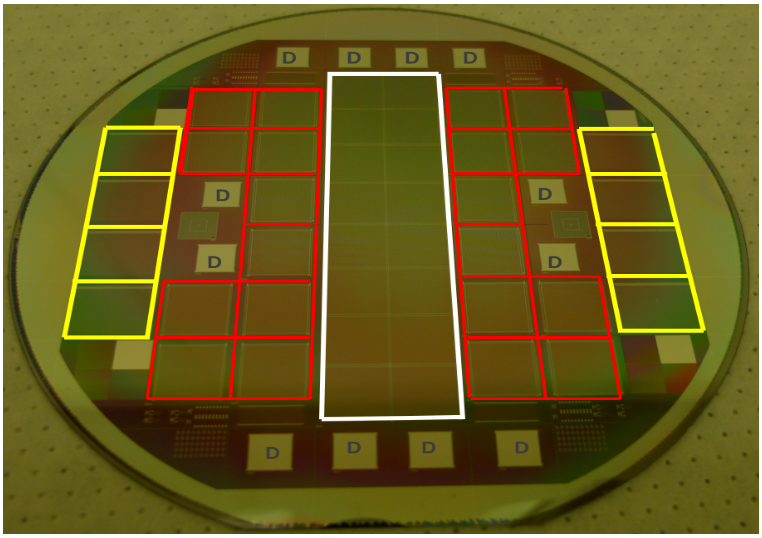

Figure 5.3: *Photo of one of the produced wafers. The multi-chip module is marked in white, in red are the twenty single chips and in yellow the strips detectors. The pad detectors are marked with the letter D.*

5.2 Description of the devices

The studied sensors were manufactured at the Centro Nacional de Microelectrónica de Barcelona (IMB-CNM). Out of the six wafers of the production batch, five were 285 µm thick and one 230 µm thick. In addition, the n-on-p 3D pixel devices in one of the thick wafers were manufactured with a polysilicon resistance grid to compare the electric characterization of the devices biased either through the resistors grid (resistor biasing) or the guard ring (punch-through biasing).

In the wafer layout (see Figure 5.3) several devices were included: one 3D multi-chip module, with a matrix of 8×2 single sensors; twenty 3D single chip sensors, with different geometries; eight 3D strip detectors; and twelve 3D pad detectors. The multi-chip module has the same layout as the current CMS planar pixel module.

A basic pixel cell in n-on-p technology (Figure 5.6) consists of one n-type vertical electrode with a diameter of 10 µm, surrounded by a p-stop insulation ring of internal and external diameters 10 and 15 µm respectively. On the backside, 10 µm diameter p-type 3D electrodes, creating the ohmic contacts,

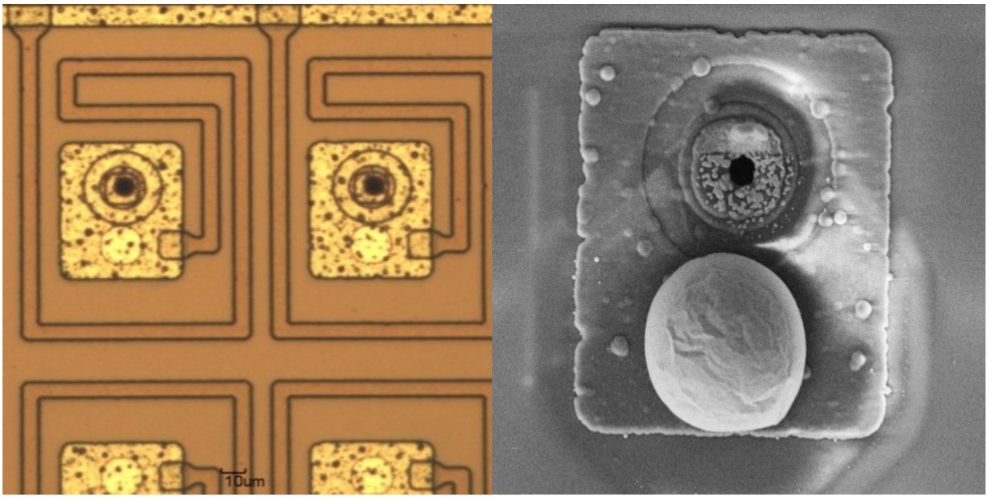

Figure 5.4: *Left: Photo of a sensor pixel cells where the metal pad on top of the n-column, polysilicon resistor routing, passivation opening a and metal line are visible. The ohmic columns (p+ doped) are on the backside and they are not visible from the front side. Right: SEM picture of one pixel cell, where the Indium ball on top of the metal pad is shown. The n-doped column with the p-stop surrounding is also visible.*

are arranged surrounding the n+ electrode. The pixel layout matches the PSI46 chip layout [133], which is the readout ASIC technology chip used in the current CMS vertex detector.

A picture of the pixel cell including the polysilicon resistor routing and a scanning electron microscope picture after the bump reflow process for one pixel cell without polysilicon grid are shown in Fig.5.4. The shiny circle on the metal pad is the passivation opening for the bump metalization.

This particular set of wafers includes two different ohmic column patterns. We refer to them as *dense* and *sparse* patterns. To clarify the difference between the two different pixel cells, Figure 5.5 shows a sketch of the pixel cells. The pixel unit cell in the dense pattern has two extra p-columns (ohmic columns). In this work, the performance differences between the two different sensor patterns are studied in terms of the detector efficiency. Two different guard ring configurations (one ring or two) are implemented.

The fabrication technique used is the proposed double-sided double type 3D detectors [134] and is shown in Figs. 5.6 and 5.7. Sensors are fabricated in a double-type configuration, with columns of one doping type etched from the

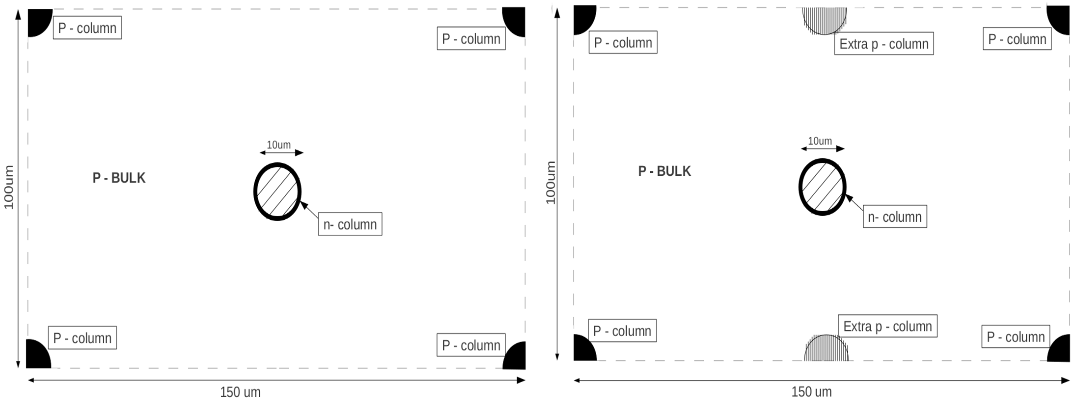

(a) (b)

Figure 5.5: *Diagrams of the two different p-column patterns. Sparse (a) and dense (b). Every column has 10 μm diameter.*

front side of the device, and the other type etched from the back side. Neither set of columns passes through the full thickness of the silicon substrate.

Figure 5.8 shows a schematic of the main fabrication process steps of double-sided 3D silicon detectors. Sensors have been fabricated in $< 100 >$ p-type silicon from Topsil manufacturer and have a resistivity in the range 10 - 30 k$\Omega \cdot$ cm. The double sided structure is similar to a conventional 3D detector [135], but requires a simpler fabrication process because the difficulty of doping the two different kinds of holes on the same side is avoided. The photolithographic steps needed to define the electrode contacts are only necessary on the top surface. The ohmic columns on the bottom surface do not require any patterning since all the p-columns are shorted together. This allows to apply the high voltage bias to the back surface of the detector by simple wire bonding, avoiding complicated rerouting for read out electronics. Every p-columns are shorted at the bottom, therefore is not necessary to bias them through the top side of the sensor. Figure 5.7 shows a cross section of the cylindrical electrodes, some structures created during the fabrication process are visible (p-stop, boron diffusion and polysilicon layers).

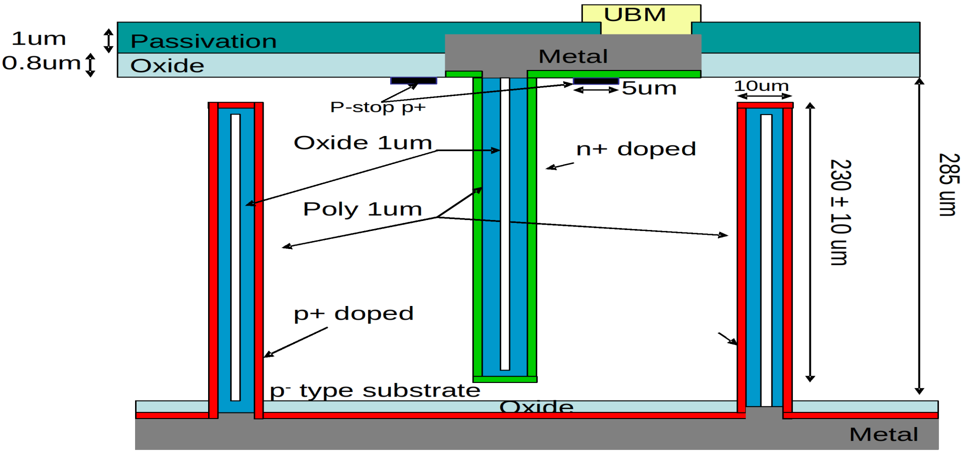

Figure 5.6: *Schematic of a 3D double sided detector. The n-doped columns (green) go into the bulk from the top side while the p-columns (red) go from the bottom. In blue we can see the polysilicon used to ensure a homogeneous dopant diffusion.*

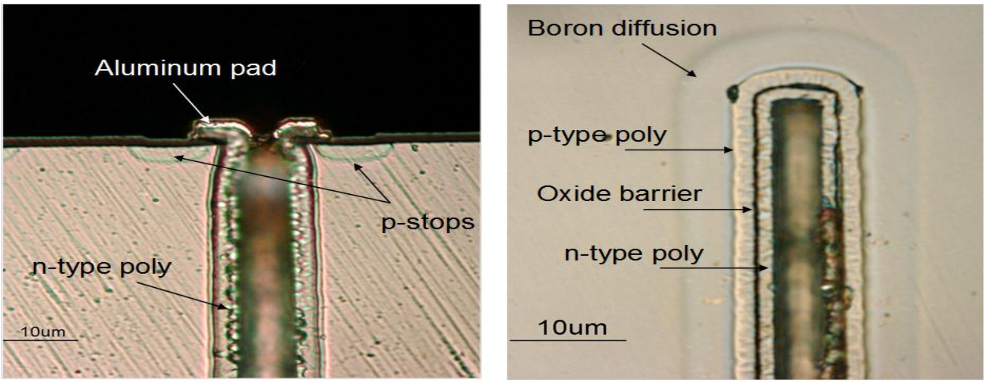

Figure 5.7: *Microscope pictures of 3D pixel sensors. Left: n-column in p-type silicon bulk, the p-stop implantation and polysilicon layer for diffusion are visible. Right: p-columns (ohmic junction) where the Boron diffusion and the two polysilicon layers separated by an oxide barrier can be appreciated.*

5.3 Electrical characterization

Sensors from six wafers have been electrically characterized (methods were described in chapter 3). Sensor nomenclature, quantity and descriptions are listed in table 5.1.

Exhaustive measurements of IV curves have been carried out in all pixel devices for each wafer. The results show an homogeneous behavior for all

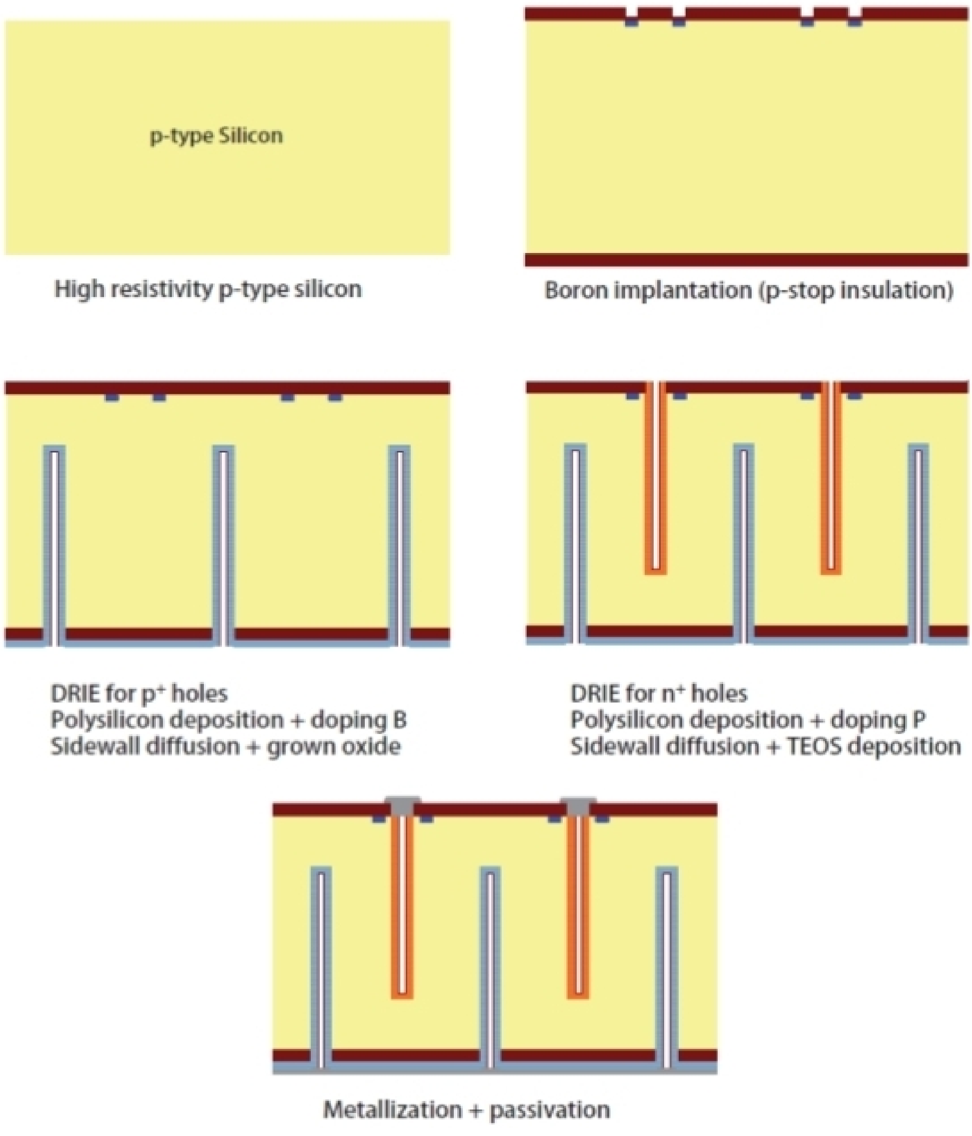

Figure 5.8: *Schematic of the fabrication process of double-sided 3D silicon detectors. The first step is the p-stop implantation, then the polysilicon deposition plus the Boron diffusion create the ohmic contacts and an oxide barrier is grown. The same process is followed to create the junction columns but diffusing Phosphorus instead of Boron. The last step is to metalize and passivate both sensor sides.*

devices in the same wafer. Leakage current values are below 100 nA in four wafers (67% of sensors), while two wafers show higher current values reaching

Device name	Qty	Description
MC	1	Multi-chip module (8×2 detectors) with sparse columns pattern and 1 guard ring
SC 11	5	Single chip detector with sparse columns pattern and 1 guard ring
SC 12	5	Single chip detector with sparse columns pattern and 2 guard rings
SC 22	5	Single chip detector with dense columns pattern and 2 guard rings
SC 21	5	Single chip detector with dense columns pattern and 1 guard ring
3D strip	8	Strip detector
3D pads	12	Pad detector

Table 5.1: *Name, quantity and description of the devices included in each wafer.*

in the worst cases more than 100 µA. Fig. 5.9 shows an example of IV curves for four single-chip and one multi-chip sensor on wafer 6. Letter B indicates the sensor position in the wafer (wafer center in this case). Differences between devices in the same wafer are below 100 nA and as expected the multi-chip (sixteen single-chips) has higher leakage current.

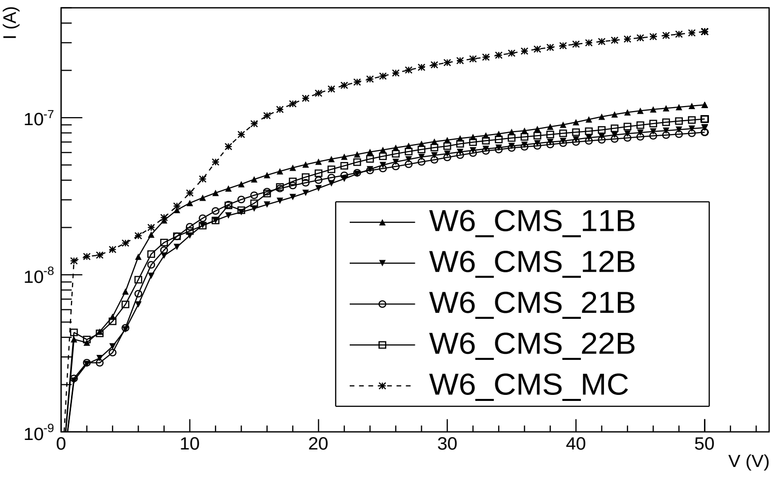

Figure 5.9: *Current voltage characteristics of the sensors in one wafer (wafer 6) 285 µm thick, 4 single chips and 1 multi-chip (8×2).*

One of the aims of the electrical characterization was to assess the advantages and drawbacks of integrating a polysilicon resistor grid in the pixel sensor design. This resistive biasing grid allows the full depletion of the sensor without the need of bonding it to the read-out ASIC. This enables easier electrical testing and qualification of the sensor before it is bonded, one of the most expensive and time consuming part of the fabrication of a pixel module. We have measured the current-voltage (IV) characteristic with two different biasing configurations: through the bias ring and by means of the guard ring (punch-through biasing). The results are presented in Fig. 5.10, for one sensor. No relevant differences are found, biasing the sensor through the polysilicon resistor grid or by punch-through. Another important result shown in this figure is that no breakdown is observed below 200 V, which guarantees full depletion after high irradiation fluences.

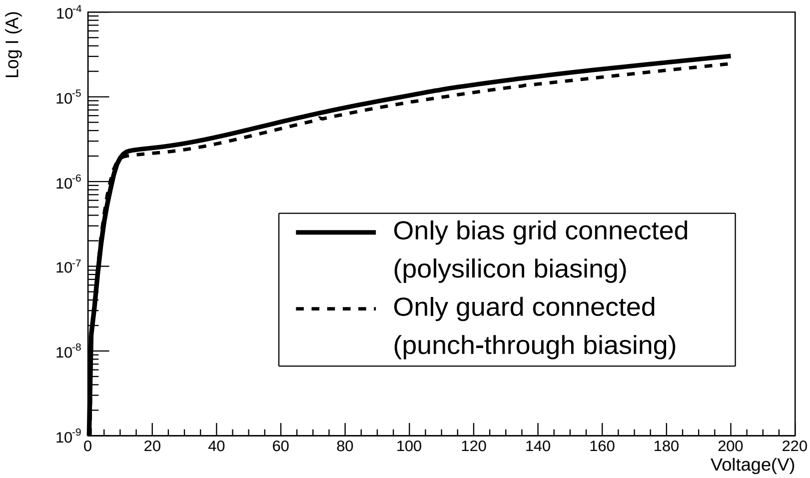

Figure 5.10: *Current voltage characteristics of one sensor. The continuous line shows the measurement biasing through the polysilicon grid. The dashed line shows the measurement biasing by punch-through.*

The capacitance-voltage (CV) characteristic was determined using an LCR meter and an auxiliary circuit for decoupling the high voltage bias and the input signal to the LCR meter. The frequency of the AC signal to measure the CV curves was fixed at 10 kHz and the amplitude at 100 mV. From these curves, the value of the full depletion voltage (V_{fd}) of the 3D pad sensors was

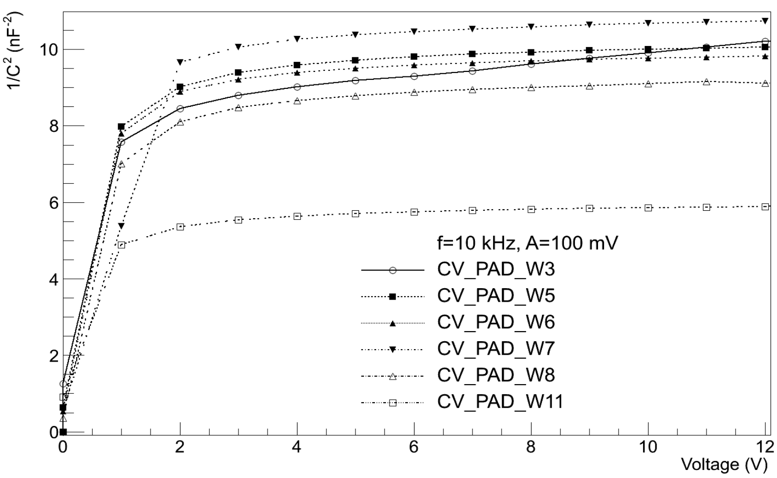

Figure 5.11: *1/C^2 voltage characteristics of 3D pad detectors from every wafer. Wafer 11 (W11) is 230 µm thick while the others are 285µm thick. V_{fd}=1.5 V in pads and V_{fd}= 9 V in sensors.*

extracted by the standard algorithm of finding the intersection point between the two straight lines fitting the ramp-up and plateau sections of the 1/C^2 curve which is shown in Fig. 5.11. The depletion voltage extracted from the 3D pad detectors has been used to analytically determine the depletion voltage of the single-chip and multi-chip sensors using the expression for a true coaxial electrode given by Equation 5.1 [74, 136], where r_1 and r_2 are the electrode column outer radius and the distance between p+ and n+ doped columns, respectively. N is the impurity density in the bulk, q is the electronic charge, and ϵ is the dielectric constant of silicon. Using these parameters and the measured 3D pad depletion voltage as inputs, the assessed full depletion voltage for the pixel detectors is 9 V. A working voltage of 20V has been chosen to ensure that the sensor is fully depleted.

$$V_{fd} = \frac{Nq}{2\epsilon}\left[r_1^2 Ln\frac{r_2}{r_1} - \frac{1}{2}\left(r_2^2 - r_1^2\right)\right] \tag{5.1}$$

The sensors' leakage current stability has also been studied. To make this measurement, sensors have been biased at 30 V for one hour recording the

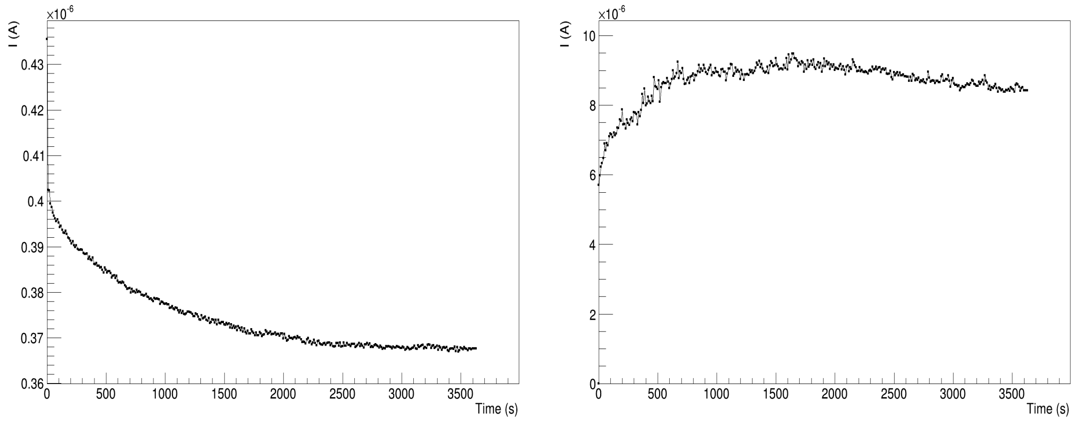

(a) (b)

Figure 5.12: *Stability measurement for two sensors. Single chip sensor (a) and multi-chip module (b). A multi-chip module is formed by 16 single chips, therefore the current value for a multi-chip module is about twenty times higher.*

leakage current. Figure 5.12 shows the leakage current for a single chip and a multi-chip module during an hour. The difference in the current values is due to the sensor size, a multi-chip module is formed by sixteen single chips.

5.4 Readout Chip. PSI46

The readout chip used to test the 3D-pixel samples was the current CMS pixel readout chip. In this section a brief summary extracted from the references [133, 137–141] is given with the purpose of setting the basis for the complete understanding of the detector performance. The CMS pixel chip was developed in the radiation hard DMILL technology [142] and is organized in 26 double columns (52 columns) and 80 rows (see Figure 5.13). The chip integrates 1.3 million transistors in an area of 7.9 × 9.8 mm. Three different blocks can be distinguished in Figure 5.13, the interface area including DACs and supply pads, the double column periphery which controls readout (data buffer) and trigger validation within double columns (time stamp buffer) and the Pixel Unit Cell (PUC) array (4160 PUCs in one single chip).

Figure shows 5.14 a schematic of a PUC. Two parts are well distinguished:

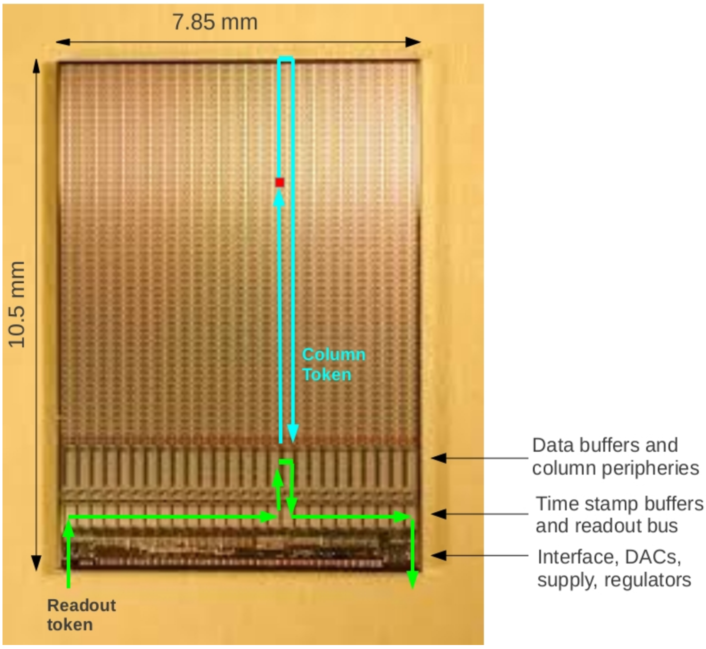

Figure 5.13: *PSI46 readout chip for the CMS pixel detector. Source: [133]. A readout token looks for a column with a hit and reads it out through a column token.*

on the top is represented the analog part and on the bottom the digital part of the circuitry. The sensor signal goes through the bump into a preamplifier and a shaper (the same circuit is used when a calibration signal is sent). A programmable current source at the input compensates for the detector leakage current. The zero suppression is done by a comparator that also sets a global threshold for all units. To compensate for possible local transistor mismatches, each pixel includes a 4 bit DAC to trim the threshold. Once the signal is over the threshold it is stored in a sample/hold circuit. Every double-column output are connected to a hard-wired OR column which notifies the column periphery of any hit in the double-column. The periphery synchronize the arrival of hits by the present bunch crossing counter (stored in a time-stamp buffer). The hit pattern for this bunch-crossing is frozen and the data transfer to the data buffer starts (column drain) by a fast column token. The hits pixel is inactive until the information is transfered while pixels without hit are skipped by the column token.

The signal is then sent to the periphery together with the row address.

Finally, the readout token passes on, taking the pixel address and the signal. The time needed to scan a column depends on the number of hits in the same double column ($t \leq 50\text{ns} + (50\text{ns} \times$ number of hits). The signal is sampled after a fixed time delay controlled globally in each ROC. The peaking time depends on the pulse height and varies from pixel to pixel, the relative error due to a non-perfect sampling time has been measured in [138] and is bellow 2.5 % and 1% in low and high signals, respectively.

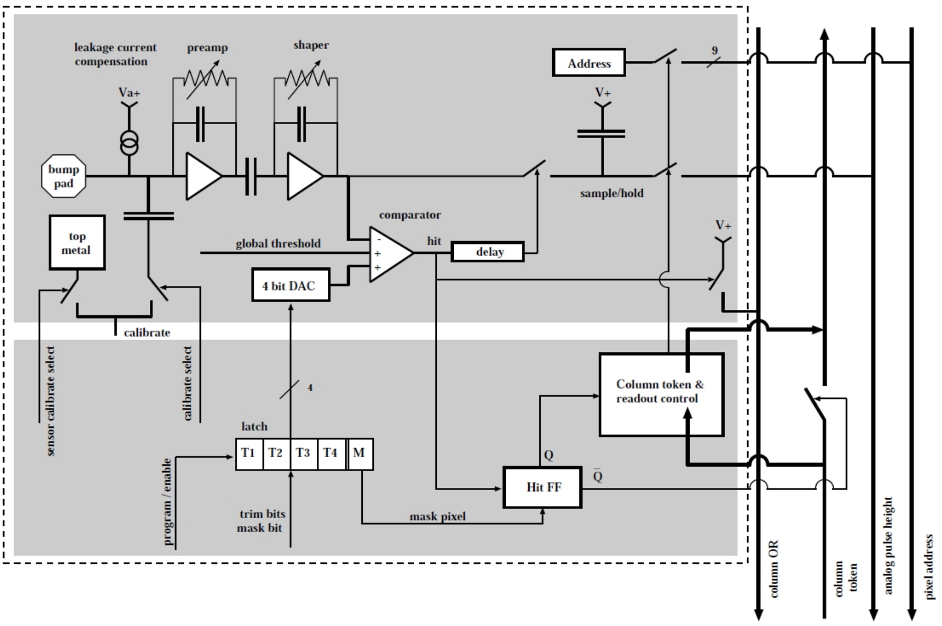

Figure 5.14: *Schematic of a pixel unit cell [138].*

The transfer of hit information from the pixels to the storage buffers is controlled by the column periphery. When a hit associated to a time stamp is given, periphery associates any later hit with another bunch crossing. It can be one active column drain and up to two pending allowed. Any other hits outside of these are lost.

The PSI46 readout chip has an analog readout scheme running at 40 MHz. The pixel address is coded into six voltage discrete levels and readout in five clock cycles: two for the column ID, three for the row ID and and extra clock cycle is need to readout the analog pulse height. In Figure 5.15, the analog readout sequence is shown. The first three values (first three clock cycles) compose the chip header and are the ultra black (large negative signal), black (zero signal) and last DAC value. Then five signals codify the unit cell address, and finally the analog pulse height followed by a black level that is a chip trailer member.

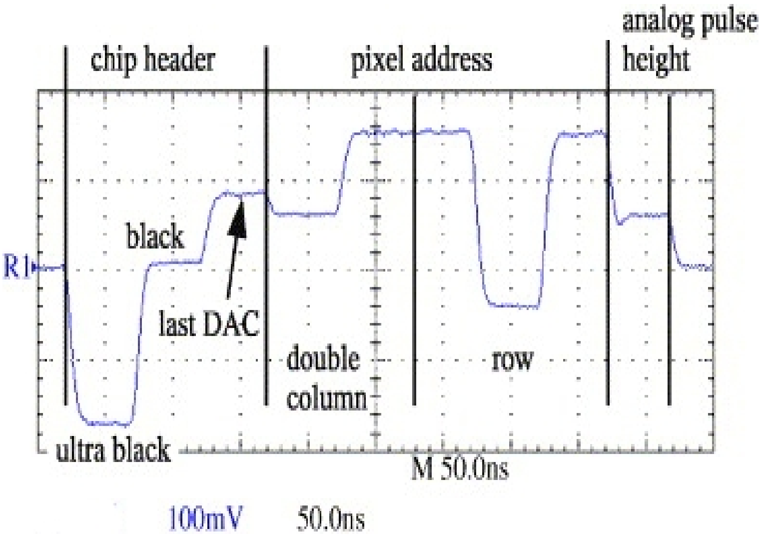

Figure 5.15: *Readout sequence of a PSI46 ROC [138].*

A requirement for the right performance of a ROC is that the voltage levels used to codify the pixel address are well distinguished between themselves. In Figure 5.16 the result obtained during a data taking run for a ROC in the laboratory is shown. The measured distribution of the address levels for a ROC has to be clearly separated to allow an easy reconstruction of the pixel address.

There are several test that are performed to evaluate the ROC functionality. The test procedure are described in detail in reference [139]. We will show later in section 5.6 the results obtained in the ROC qualification when the 3D pixel sensors were connected to the ROC.

5.5 Interconnection process

The interconnection process between sensor and read out chip, consisting of bump bonding and flip-chip, was done at the Paul Sherrer Institute (PSI)

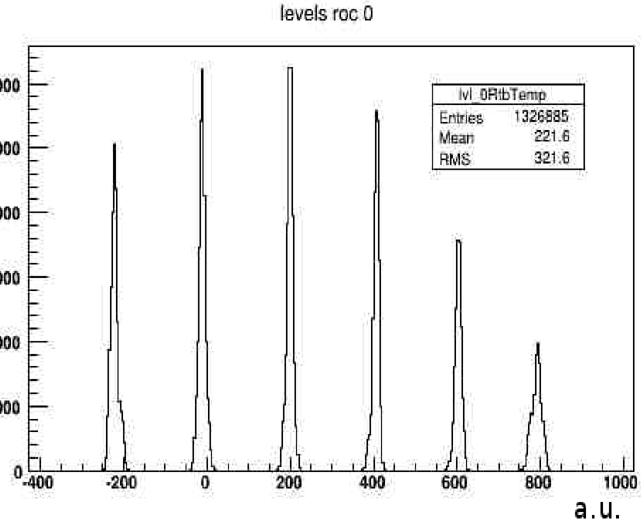

Figure 5.16: *Histogram of the sampled address levels of a ROC during a data taking at the PSI laboratory in arbitrary units.*

bonding laboratory. The procedure is described in [29] and consists of an Indium bump bond process developed at PSI as part of the R&D for the CMS-pixel detector. Figure 1.7 in section 1.2.1 shows a scheme of the process. The first step is the under bump metalization (UBM) and consists on the deposition of three metal layers on top of the sensor. Through a wet lift-off process, the metalization remains only on top of the passivation opening in the metal pad. Then the Indium is evaporated and deposited on top of the metalization. Following again a wet lift-off process it ends up in an octagonal metallic wafer on top of every bump pad. All the previously described processes are done in each wafer. After that, sensors are diced.

To form the Indium (contact) balls, devices are heated until the Indium is molten and, by surface tension, spherical balls are created. This process is the so-called *reflow*. Figure 5.17 shows two scanning electron microscope pictures of the Indium wafer and Indium ball in 3D pixel sensors. Some of the different structures in the implant columns are visible in both pictures (column perforation, implant, p-stop and metalization).

The readout chip also needs an Indium layer to facilitate the adhesion between sensor and ROC. Once the sensors have the contact balls, the chip has to be set on top of it correctly aligned. This process is the *flip-chip*.

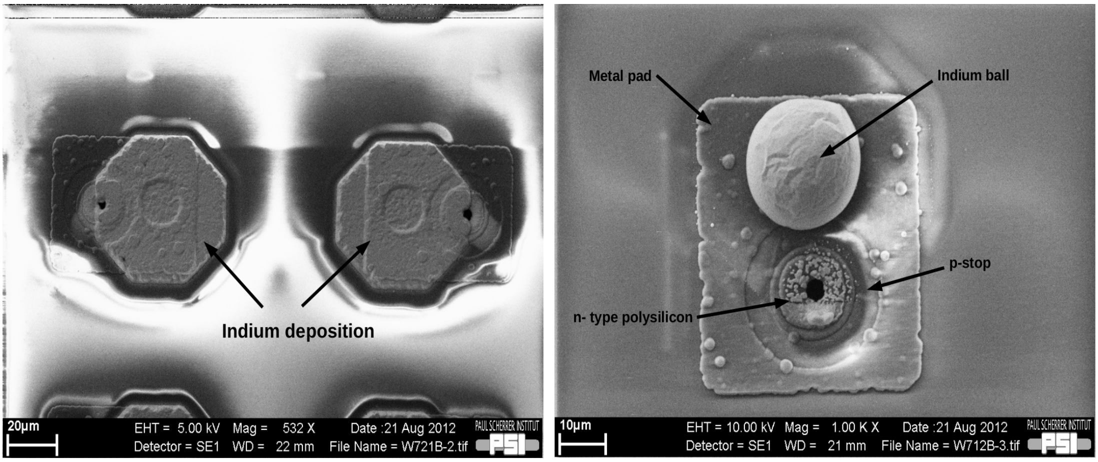

(a) (b)

Figure 5.17: *Scanning electron microscope pictures of indium bumps (a) before and after (b) reflow in 3D pixel sensors. The bumps pitch is of 100* μ*m and the reflowed bumps diameter is of 20* μ*m.*

This is done by a PSI home-made automatic bump-bonding machine. This machine features a moving table, a pick and place tool, a probe card and a microscope. The microscope is used to set the reference coordinates to the machine. It uses reference alignment marks from the sensor and a pattern recognition algorithm. The pick and place tool takes a ROC, also properly aligned following the same strategy as for the sensor, tests it in a probe card and pushes it on top of the sensor with a force of 30 N and holds it for a minute. If a chip does not pass the electrical test, it is refused and a new one is taken. After the correct placement of the chip and sensor a *second reflow* is needed to obtain a stable mechanical connection. This second reflow corrects possible small misalignments thanks to the surface tension forces.

After the second reflow process in 3D pixels, some inhomogeneities were observed. In Figure 5.18(a), a sensor area after the first reflow is shown. We can see that some of the Indium balls are not spherical shaped, but they have a “banana shape” produced by Indium adhesion to the sensor surface inhomogeneities. Figure 5.18(b) shows another micro-photograph with the state of the Indium balls after the ROC chip is flip-chiped on top of the sensor and removed. The chip pad marks on the contact balls are visible, showing that the contact was correctly made. Therefore we concluded that these inhomogeneities in the bumps should not affect the sensor-ROC connection.

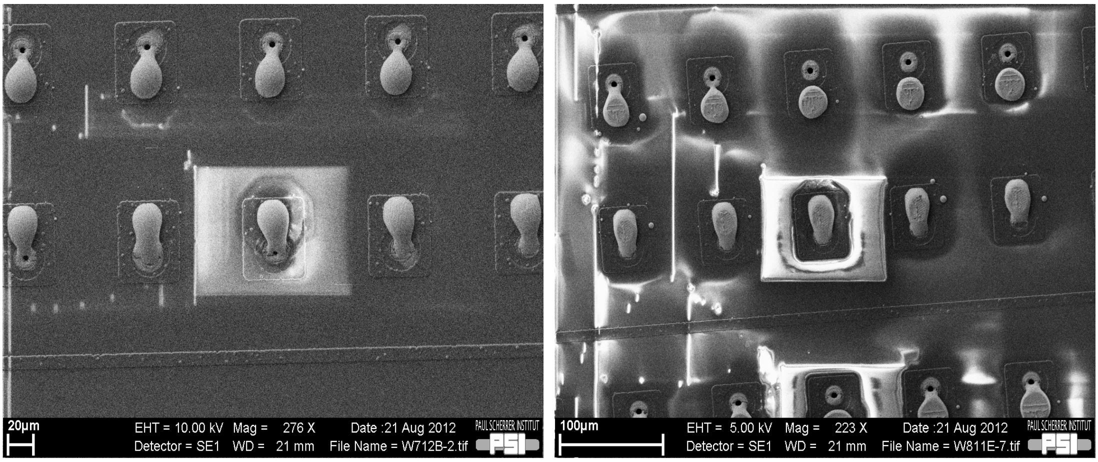

(a) (b)

Figure 5.18: *Scanning electron microscopic pictures of indium bumps. (a) A image before the flip chip showing that some residual Indium joined to the columns creating "banana shapes" instead of spheres. (b) Sensor after flip chip, after the ROC was hold against the sensor and removed in order to see the chip pad marks in the indium balls. They are visible in every bump indicating that chip and sensor contacted properly.*

5.5.1 Bump bonding test in 3D pixel sensors

The bump bonding test showed some peculiarities of 3D pixel sensors that are explained in detail in this section.

The Bump bonding test. The method used is called the *modified external calibration.* In the ROC a possibility to send a calibrate signal through the sensor is implemented (see reference [133] and Figure 5.19). In principle, this functionality allows the identification of missing bumps by measuring pixel thresholds. Two different measurements are done with the same calibration signal:

- Closing the switch2, the calibration signal reach a pad on the ROC surface. The signal induces a charge in the sensor that when the bump is connected will reach the front end. If the bump is bad connected or

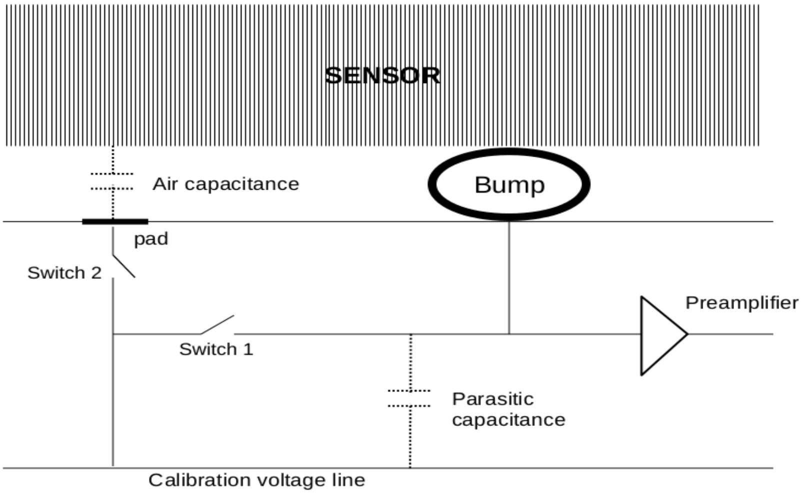

Figure 5.19: *Schematic of the relevant components for the bump bonding test.*

missing, the signal will reach the front end by traversing again the air gap (Vcal procedure).

- Keeping both switches open, the signal could reach the pre-amplifier by crosstalk (parasitic capacitance or xtalk procedure).

A threshold measurement is done by both procedures. When there is a bad bump contact, both threshold will be very similar, while when the bump is connected, both threshold values will be different at least by five DAC units. This procedure was validated after testing detectors where some bumps were removed on purpose. In this section, we see a good agreement between the bump bonding test results and the hit occupancy maps obtained in 3D samples with a radioactive source.

Typically, in planar sensors bump bonding was always successful (99 % bump yield). However, in 3D sensors we had lower bump yields. In Figure 5.20 (a) and (b) we show the result after the bump bonding test . When the difference between the threshold using Vcal and xtalk procedure is zero, the bump is missing. Another test (see 5.20 (c) and (d)) shows the sensor response to a radioactive source, particularly the hit occupancy map, that in spite of the need of a different setup is a result that confirms the bump bonding test result.

In addition to the missing bumps, we can see a “columns pattern” in the bump-bonding test results that it doesn’t affect the signal itself, where the pattern is not visible (Figures 5.20 (c) and (d)). This pattern could be due to the observed ”banana shape” after the first reflow during the interconnection process. These ”bananas” appeared with a similar pattern. In Figure 5.20 (c) there are some areas with more hits (red area in the middle of the sensor and two more to the right). Those areas correspond to holes on the PCB between the sensor and the photomultiplier that provides the triggers.

After these results, we realized that the internal stress in the sensors caused a strong sensor bowing during the second reflow, breaking the connection between sensor and ROC. By mistake, in this particular sensor production the passivation layers, which were usually deposited in both sides of the wafers, were deposited only in one of the sensor sides, increasing considerably the stress suffered by the sensors.

To partially solve this problem, a weight was placed on top of the sensor - ROC “sandwich” during the second reflow. With this rudimentary method, we managed to have better hit maps. Figure 5.21 shows the hit map of two sensors where this technique was applied. We can see how the bump bonding map improved comparing against results shown in Figure 5.20. In Figure 5.21, the PCB holes are not visible because the data were taken with a random trigger instead of with the photomultiplier triggers. In this way, we can observe the full sensor area not being limited by the scintillator size.

5.6 ROC calibration

Every ROC needs to be configured individually to cope with ASIC manufacturing non-uniformity. This section will summarize the configuration procedure fully detailed in [137, 139, 143, 144]. The behavior variation between pixels in a ROC is relatively small, the found values for one pixel cell are, usually, valid also for all other pixels in the same ROC. Every ROC has 26 DAC parameters programmable for the ASIC configuration. The parameters that need to be adjusted are those relative to the current consumption of the chip, calibration signal’s amplitude and sampling point and the comparator threshold. The

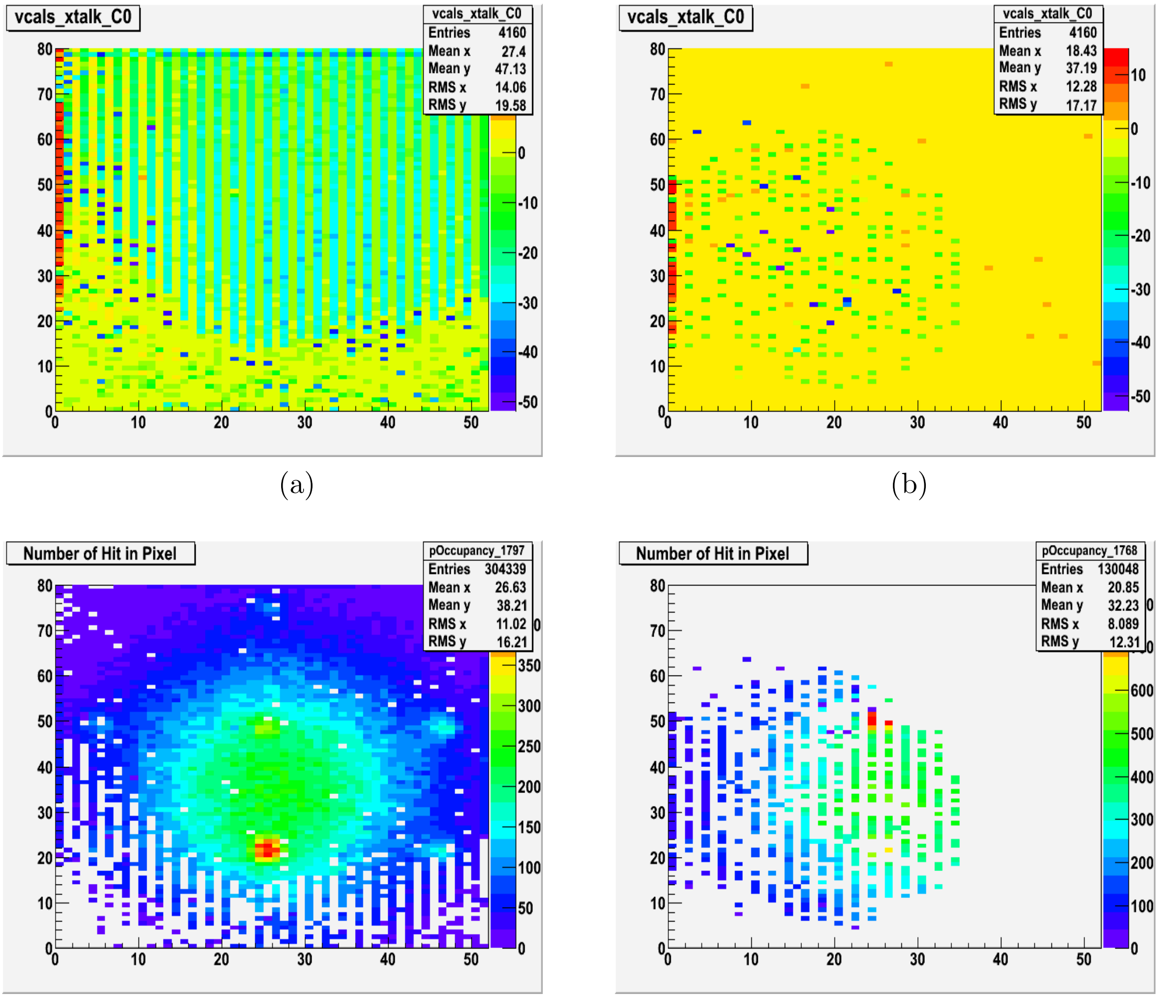

(a) (b)

(c) (d)

Figure 5.20: *Bump-bonding test result for two different sensors: 11B (a) 22B (b). And the hit occupancy map under a* ^{90}Sr *radioactive source for sensor 11B (c) and 22B (d). We can see a lot of missing bumps in both tests.*

PSI46expert software include specific test to adjust them and the most important are in this text reviewed while the information needed to run this software can be found in the CERN twiki [145]. The test procedure is as follows:

- Analog and digital currents need to be set to values about 24 mA, which is the current consumption needed to operate properly the analog and

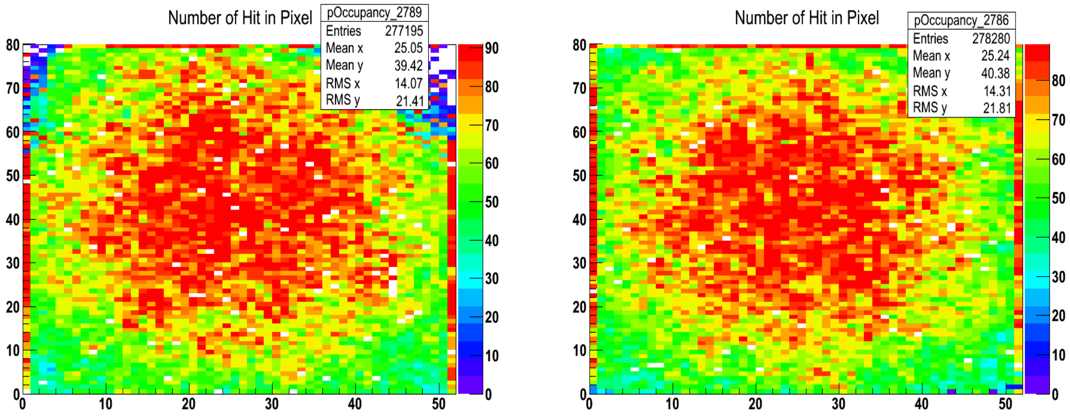

(a)

(b)

Figure 5.21: *Hit occupancy maps for two different sensors after a second reflow performed placing a weight on top of the sensor-readout chip sandwich: 11A (a) 22A (b). Random trigger is used.*

digital parts of the ASIC. To reach those values, the analog and digital voltages have to be adjusted to provide the right power.

- Tornado plot, the *tornado* plot is an efficiency plot. The parameters values used in this test was determined by experimental studies from reference [144]. A calibration signal amplitude of 200 (DAC units) is injected and readout 5 times for every threshold (Vthrc) and delay respect to the trigger (CalDel) values. In Figure 5.22 a tornado plot for one pixel cell of one unirradiated chip already connected to a 3D pixel sensor is shown. The red area shows which are the values for Vthrc and CalDel that have an efficiency of the 100 %. The chosen working values should be as far as possible of the inefficient area and they correspond to the area within the white circle. This area corresponds to a $Vthrc \sim Vthr_min + 50DACs$ and to the middle value for CalDel for this Vthrc.

- Pixel maps, once the threshold and delay values are set, the next step is the pixel map test. It consists on sending a calibrate signal to each pixel unit cell and check that the registered output signal is the expected. In this test the defective pixel cells are identified. In Figure 5.23 the result

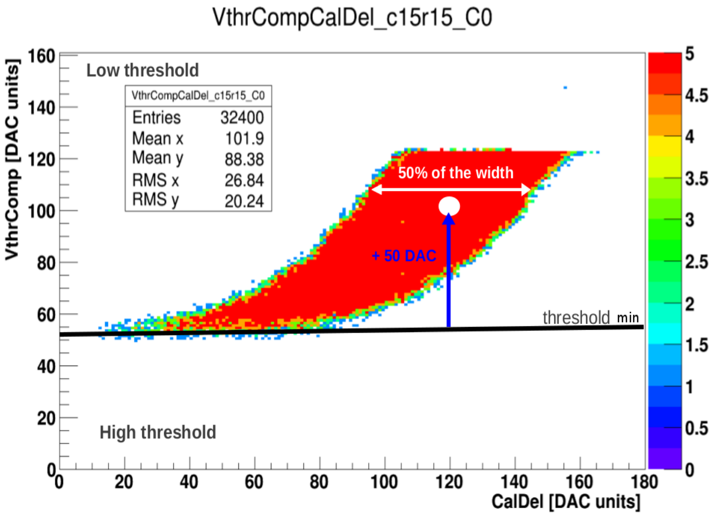

Figure 5.22: *Tornado plot for a pixel unit ROC. The red area shows the values of the DACs parameters, CalDel and Vthrc, where the ROC achieve its maximum efficiency.*

of this test is shown, in this case ten defective pixel cells were identified.

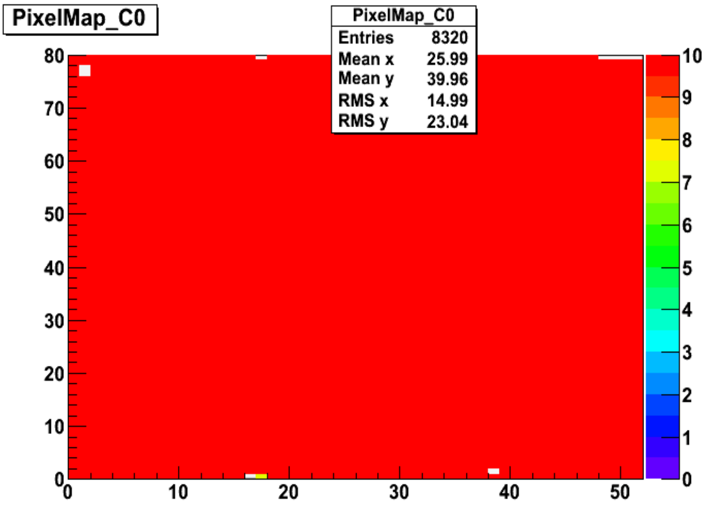

Figure 5.23: *Pixel map for a ROC. The red area shows the working pixel cell units. This particular ROC has 10 defective units.*

- Address level test. The objective of this test is to verify that all the address levels are well distinguishable for all pixels. In Figure 5.16 an example of the result of this test was shown, where the different levels are well defined.

- Trimming and threshold. There are little differences on the threshold settings between pixel cells. To reach the homogeneity on the sensor response, every pixel cell output is tested using the same signal amplitude (calibration signal pulse hight). The threshold value in a ROC is unified by means of four trim bits and the *trimming* test. The four trim bits allow sixteen trim states per pixel unit. The size of the correction is set by the trim voltage.

  Once the trim voltage and the calibration signal are fixed, the algorithm finds the trim bits configuration for every pixel when they start responding for the calibration signal. The calibration signal distributions for a ROC before and after trimming to a threshold value of 45 DACs units are shown in Figure 5.24. After trimming the homogeneity in the sensor response increased by a factor of three.

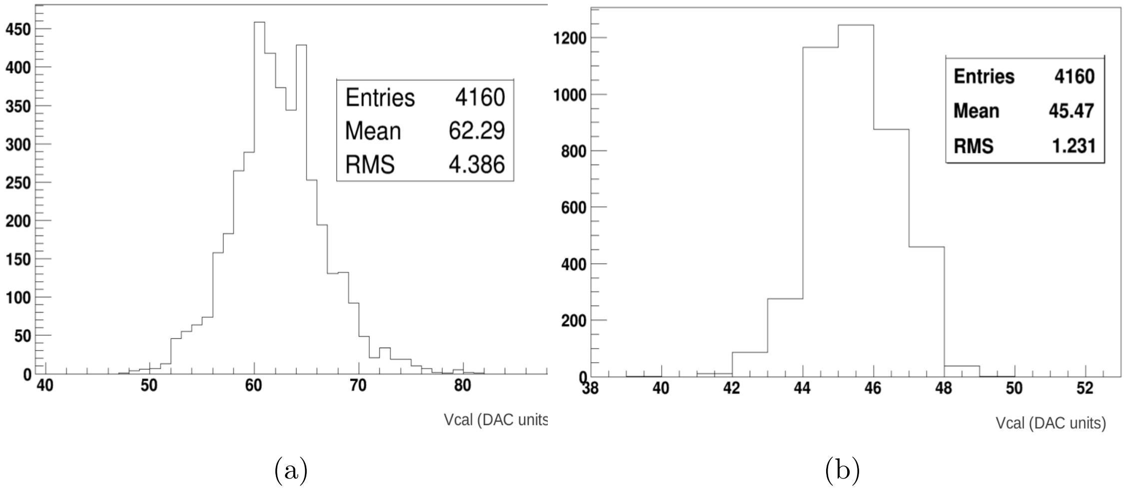

Figure 5.24: *Vcal distribution for a ROC: (a) before and (b) after trimming to a Vcal value of 45.*

- Pulse Height Calibration. This test is required to determine response linearity, the gain and pedestals for each pixel. Both are needed to convert the collected charge (in ADC counts) to electrons. There are two different steps, first conversion of ADC counts into Vcal units (calibration signal amplitude), and second, conversion from Vcal to electrons:

- From ADC counts to Vcal units. This calibration is done via software, it is one of the included tests and is performed injecting various amplitudes of the calibration signal (Vcal) and measuring the resulting signal (ADC). The slope of that relation gives the gain and the offset is the pedestal.
- From Vcal to electrons. This calibration is done using an X-ray source. The primary source is Americium -241 and the secondary are: Mo, Ag and Ba, that produce 4844, 6139 and 8906 e^- in 285 μm thick silicon , measuring the sensor response to their signals in Vcal units, representing them versus electrons and fitting their response to a line. The results show that on average: 1 Vcal corresponds to 66 e^- and there is an offset of -420 e^-. Therefore trimming to a threshold of 45 in Vcal units corresponds to a threshold of 2550 e.

5.6.1 ROC qualification in irradiated samples

Unlike for strip sensors, in the case of pixel sensors the detector irradiation takes place after the interconnection. Therefore, sensor and ROC are irradiated together. ASIC chip components are damaged by radiation and the ROC performance after high particle fluences is degraded. Finding the new DAC parameters becomes non-trivial. It cannot be automatized easily and normally human intervention is needed.

The way to proceed is the same as described before, but irradiated chips need an extra effort to find the working parameters. There is not a standard procedure. Some of the DACs that might need to be changed for irradiated chips are those related to the processing and readout speed. Preamplifier and shaper need to be as fast as possible and the voltage for the digital part V_{dig} needs to be higher.

Highly irradiated chips (3.5×10^{15} n_{eq}/cm^2) responds very slowly to the pixel programming. The pixel maps show a "stripy" behavior. There is a tuned firmware for irradiated chips that delays the calibration signal to emulate the actual situation.

5.7 Radioactive Source Characterization

Once the readout chip is successfully configured a first assessment of the detector assembly is carry out using a ^{90}Sr source. The setup was described in section 3.3 and illustrated in Figure 3.14. In this section, the characterization results from the radioactive source test are shown both for unirradiated and irradiated samples. The main parameter extracted from this test is the dependence of the charge collection efficiency versus radiation.

- **Unirradiated samples.**
  In Figure 5.25, the charge distribution for two 3D pixel sensors is shown, sensors are biased to 20 V. The charge distribution for different cluster sizes are displayed in different colors. Considering that the sensors thickness is 285 ± 15 µm, the expected Most Provably Value (MPV) in the collected charge distribution is of 21660 ± 1140 e^-. The sensors tested have acceptable MPVs within the expected uncertainties. In terms of charge collection we expected to collect more charge in the sensor with a dense pattern because the field is higher, however the observed differences are compatible with the differences between ROC performances, which is estimated to be at least around 15 %.

  Measurements made over twelve sensors confirm that all of them perform as expected for a 285 µm thickness. These results were obtained applying a bias voltage of 20 V.

- **Irradiated samples up to 10^{15} n_{eq}/cm^2.**
  Five irradiated sensors were studied: four pixel sensors irradiated up to a fluence of $1 \cdot 10^{15} n_{eq}/\text{cm}^2$, two of them with protons and the other two with neutrons and one device irradiated with protons up to $5 \cdot 10^{15} n_{eq}/\text{cm}^2$. We did not manage to configure any PSI46 ROC irradiated to the fluence of $1 \cdot 10^{16} n_{eq}/\text{cm}^2$. Note that these chips were not developed to endure a fluence of $1 \cdot 10^{16} n_{eq}/\text{cm}^2$ which is much higher than the fluences at LHC.

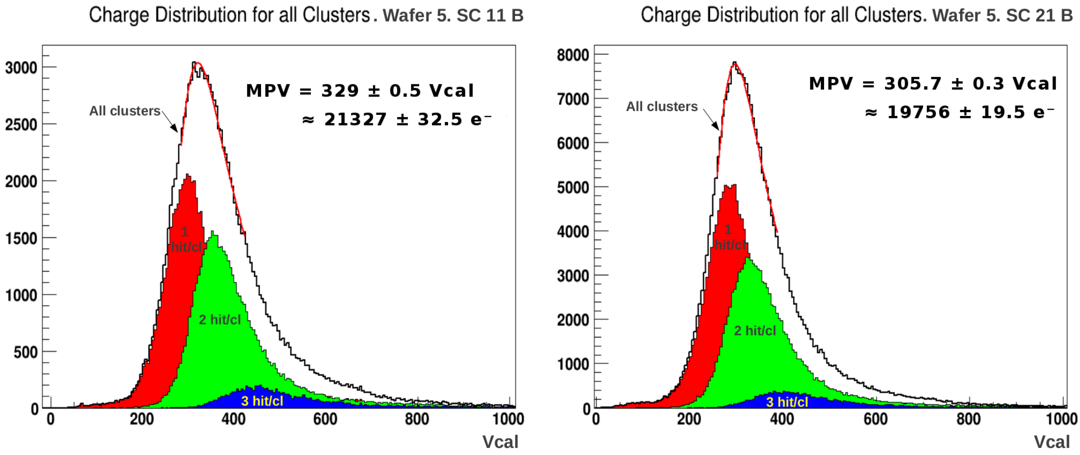

(a) (b)

Figure 5.25: *Cluster charge distribution for the two 3D pixel sensors patterns: (a) sparse and (b) dense. Sensors are biased at 20 V. The different distributions correspond to one (red), two (green), three (blue) hit clusters and the total distribution of clusters (black line). The fit of the peak of the total charge distribution to a landau function shows MPVs of: 329.5 and 305.7 Vcal units, that correspond to 21327 and 19756 electrons respectively.*

Figure 5.26 shows the most probable value of the collected charge of the 5 devices versus the bias voltage. The behavior for irradiated detectors up to $1 \cdot 10^{15} \mathrm{n}_{eq}/\mathrm{cm}^2$ is very similar for different devices and independent of the radiation type. Compared to the MPV of unirradiated devices (see Figure 5.25) the signal is reduced by 30% and V_{fd} increases to around 120 V. The device irradiated to a fluence of $5 \cdot 10^{15} \mathrm{n}_{eq}/\mathrm{cm}^2$ shows a signal reduction of 55% with respect to the unirradiated samples.

To estimate the full depletion voltage in an irradiated 3D sensor we define an effective relative efficiency E_r as the ratio between the number of events with reconstructed clusters and the number of events that produce a trigger in the photomultiplier, therefore those events that start the readout chain.

$$E_r \equiv \frac{Number\ of\ events\ with\ reconstructed\ clusters}{Number\ of\ triggered\ events} \tag{5.2}$$

We then define the depletion voltage as the voltage for which E_r reaches

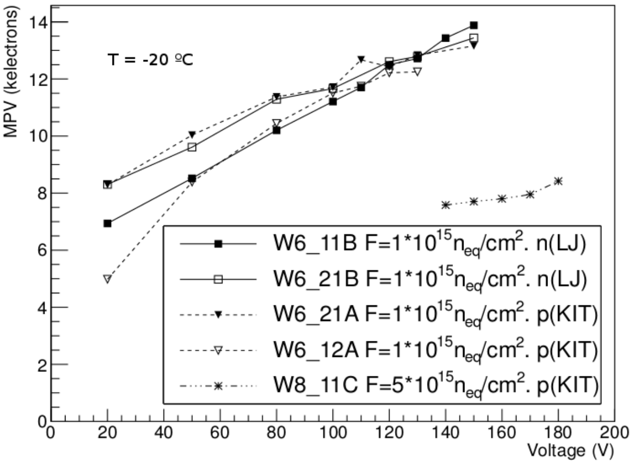

Figure 5.26: *Most Probable Value against bias voltages, four samples irradiated up to* $1 \cdot 10^{15} n_{eq}/cm^2$ *and one up to* $5 \cdot 10^{15} n_{eq}/cm^2$.

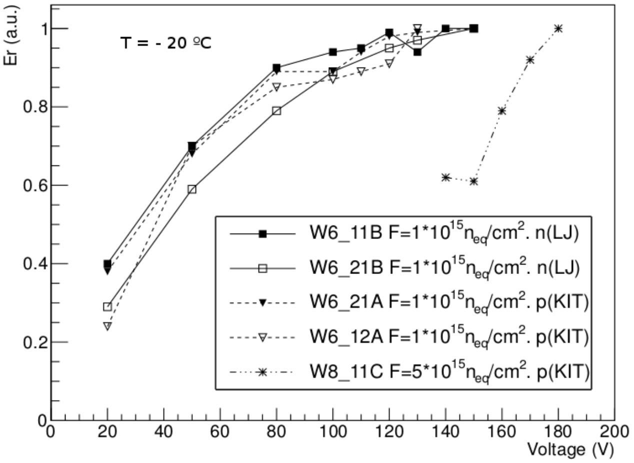

Figure 5.27: *Normalized relative Efficiency,* E_r *against bias voltage, showing a* V_{fd} *=120 V for fluences of* $1 \cdot 10^{15} n_{eq}/cm^2$ *and* V_{fd} *=180 V for fluences of* $5 \cdot 10^{15} n_{eq}/cm^2$.

a plateau. For each device, the absolute value of E$_r$ depends on the bump yield and the relative position between the radioactive source and triggering scintillator; therefore, to compare the different devices, we normalize each E_r curve to its maximum, as shown in Figure 5.27. According to the definition, the depletion voltage is reached at about 100-120 Volts for those samples irradiated to a fluence of $1 \cdot 10^{15}\mathrm{n}_{eq}/\mathrm{cm}^2$.

For the sample irradiated to $5 \cdot 10^{15}\mathrm{n}_{eq}/\mathrm{cm}^2$, the depletion voltage is not well defined. As seen in Figure 5.26, the collected charge most probable value is almost flat for any voltage, slightly increasing at 180 V, which could indicate avalanche effects. In Figure 5.27, the E_r gradient versus the biasing voltage for this sample decreases with the increasing bias voltage. Therefore, we consider the samples irradiated up to $5 \cdot 10^{15}\mathrm{n}_{eq}/\mathrm{cm}^2$ maximally depleted at a bias voltage of about 180 Volts.

5.8 Test Beam characterization

The tests shown in the previous section quantify the radiation hardness of the 3D pixel sensors in terms of depletion voltage and collected charge. In a test beam equipped with a particle's beam tracking system the resolution and efficiency of the Device Under Test (DUT) can be assessed. The test beam setup was described in detail in section 3.4. This section presents the results of these measurements. Sparse and dense pattern detectors have been characterized before and after a neutron irradiation fluence of $1 \cdot 10^{15}\mathrm{n}_{eq}/\mathrm{cm}^2$.

All the results presented here were taken with a particle beam normal to the detector plane. However, in a real experiment perpendicular tracks will be avoided either by bending the particle's trajectories using an external magnetic field or by tilting the sensor planes. Therefore this work shows results for the worst possible orientation for a 3D pixel detector. With this orientation a particle could traverse the sensor through an electrode column. This orientation was chosen in order to study the worst case scenario concerning the detector efficiency.

Detector performance was studied with a MIP's beam in terms of the charge collection. Including tracking information, the charge collection uniformity, the impact point spatial resolution and charge sharing between pixel cells can be studied as well as the sensor efficiency.

Figure 5.28 shows a schematic of the test beam setup. The chosen tracks for the efficiency analysis are those that meet the following criteria: they must have at least one cluster on each of the first three downstream telescope's

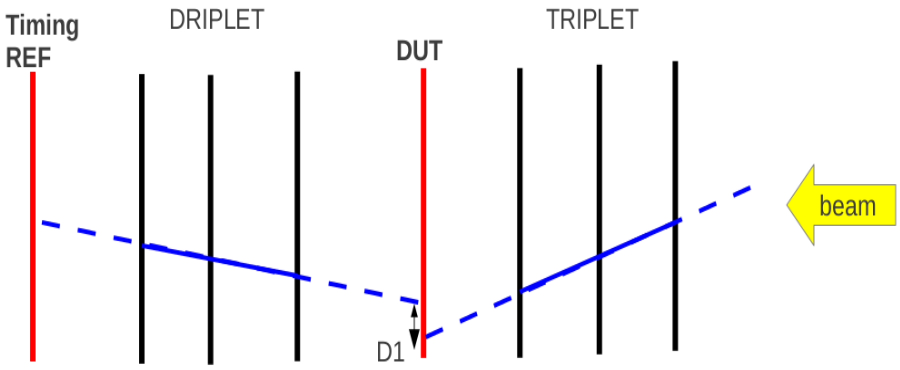

Figure 5.28: *Schematic of the DESY test beam setup. The beam is coming from the right in the schema. The first three layers (with respect to the beam direction) form the so-called triplet, then the DUT is placed before the last three telescope layers (driplet), and at the end is placed the reference sensor for timing. Deviation from a stright line due to multiple scattering is greatly exaggerated for illustration purposes.*

detector layers (triplet) as well as in the last three downstream layers (driplet) and one cluster in the reference sensor. With this set of conditions, we ensure tracks. In addition, another geometrical restriction is imposed: once the triplet and driplet tracks are traced, they are extrapolated to the DUT plane. The distance D1 between intersections of tracks with the DUT plane shouldn't be bigger than 500 µm, ensuring relatively straight tracks.

The reference sensor and the device under test have the same clock, that is not the same for the telescope and the beam. The telescope integration time is 115 µs, and pile-ups were observed depending on the beam conditions. To suppress the telescope pile-ups, the pixel sensor used as timing reference allows the synchronization between the three devices (telescope, DUT and reference plane). In this way only events properly synchronized are taken for the DUT efficiency analysis.

5.8.1 Unirradiated sensors

In this section the results obtained for unirradiated detectors are presented along with a comparative study between sparse and dense ohmic column patterns.

- **Charge distribution**

  Figure 5.29 shows the charge distributions obtained for sensors with both ohmic column patterns. The different values of the Most Probable Value (MPV) cannot be associated to the different patterns because the calibration uncertainties between Read Out Chips (ROC) can reach 15% [146].

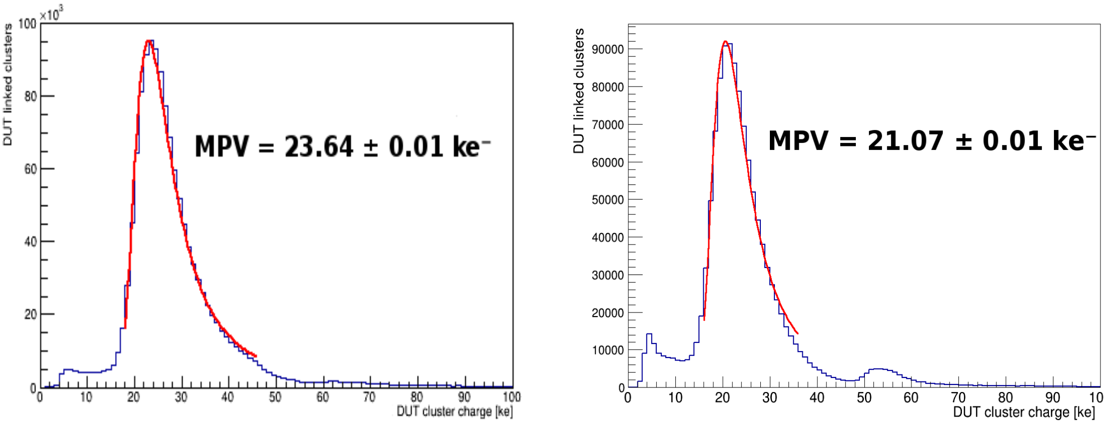

(a) (b)

Figure 5.29: *Cluster charge distribution for the two unirradiated 3D pixel sensor patterns measured in a DESY test beam: (a) sparse and (b) dense. Sensors are biased to a voltage of 20 V. The fit of the peak of the total charge distribution to a landau function shows MPVs of: 23640 and 21240 electrons respectively.*

- **Pixel's charge collection uniformity**

  With respect to the pixel's charge collection uniformity in the detector, the mean value of the cluster's charge collected for every cluster center of gravity coordinates in every group of four pixel cells in a sensor were averaged in order to increase the statistics in this study. Those noisy and bad bump-bonded units were not considered. Results are shown in Figure 5.30. The charge drop, in normal track incidence, in areas near by the electrode columns is about 13 and 14 % for sparse and dense patterns, respectively.

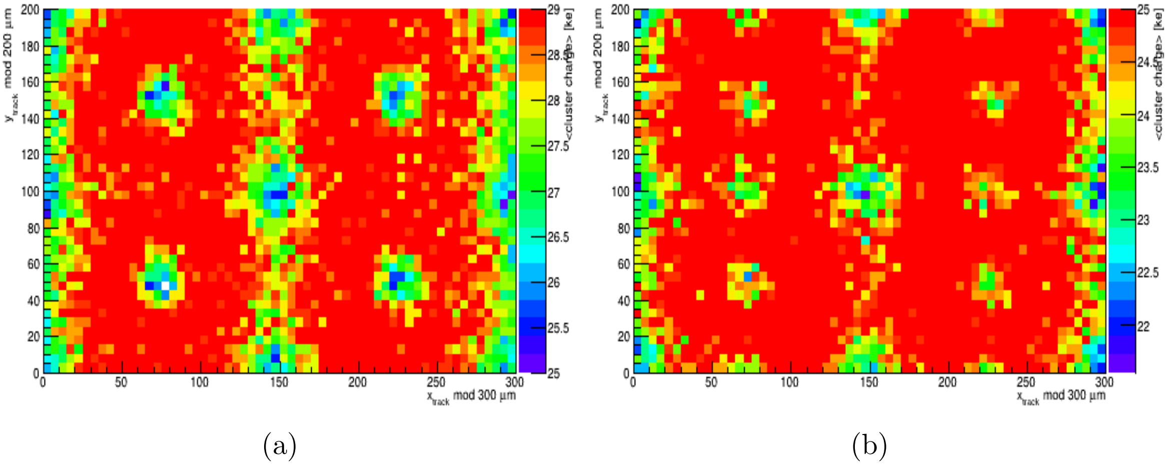

Figure 5.30: *Charge collection uniformity for the two unirradiated 3D pixel sensors patterns measured in a test beam at DESY: (a) sparse and (b) dense. Sensors are biased to a voltage of 20 V. The charge losses in columns are appreciable in both histograms.*

- **Charge sharing**

  Studies of the charge sharing between pixel cells have been done plotting the cluster size for every cluster center of gravity coordinates. Figure 5.31 shows the charge sharing plots obtained by averaging the cluster size for every four pixel cells group in one sensor. The charge sharing, as expected, appears in pixel borders, increasing in the pixel corners where four pixels converge.

- **Resolution**

  The sensor resolution is defined as the difference between the cluster coordinates calculated with the telescope tracks extrapolated on the DUT plane and the coordinates directly measured with the collected data in the DUT. DUT data are limited in resolution by the pixels pitch and the expected resolution values for a binary readout (without charge sharing) is given by 5.3.

  $$\sigma = p/\sqrt{12} \tag{5.3}$$

  However, the obtained results improve the prediction and are shown in

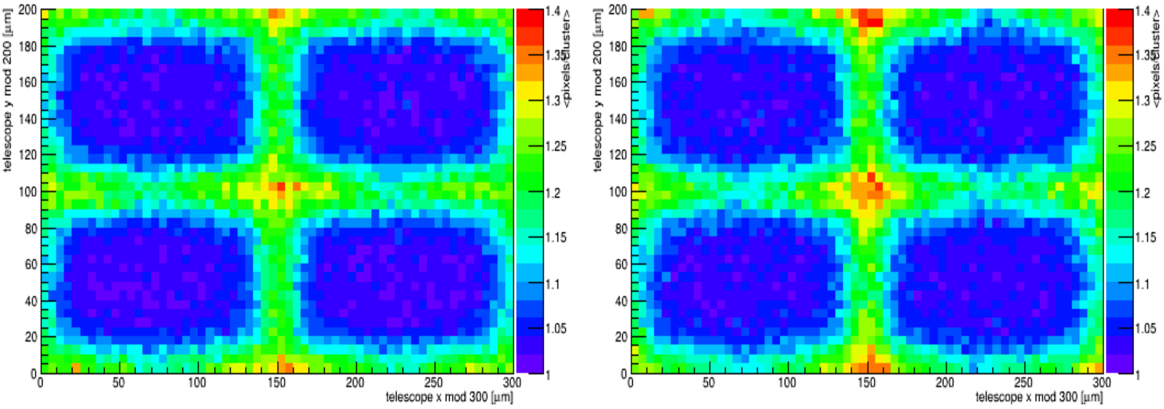

(a) (b)

Figure 5.31: *Charge sharing map for the two unirradiated 3D pixel sensor patterns measured in a DESY test beam: (a) sparse and (b) dense. Sensors are biased to a voltage of 20 V. The charge sharing takes place at the pixel cell borders.*

Figure 5.32 where the values are the average resolutions along the two detector coordinates. Following equation 5.3 and taking into account that the X and Y pitches are 150 and 100 μm, the expected resolution are 43.3 and 28.9 μm respectively. We improve slightly the expected values of about 26 μm and 37 μm respectively, probably due to the analog readout and the charge sharing between pixel cells. The charge sharing allows to estimate the center of gravity of the cluster with higher accuracy than with a binary readout. In Figure 5.32, we can also see some sensor areas that have worse resolution, due to some missing bumps in the sensor, that were not masked in this plot, where the full sensor is considered.

- **Efficiency Studies**

  The efficiency maps for both sensors are shown in Figure 5.33. To estimate the efficiency we calculate the ratio between the DUT hits with track and the total number of tracks that fulfill the previous requirements. We can see that while the ohmic columns are clearly visible in

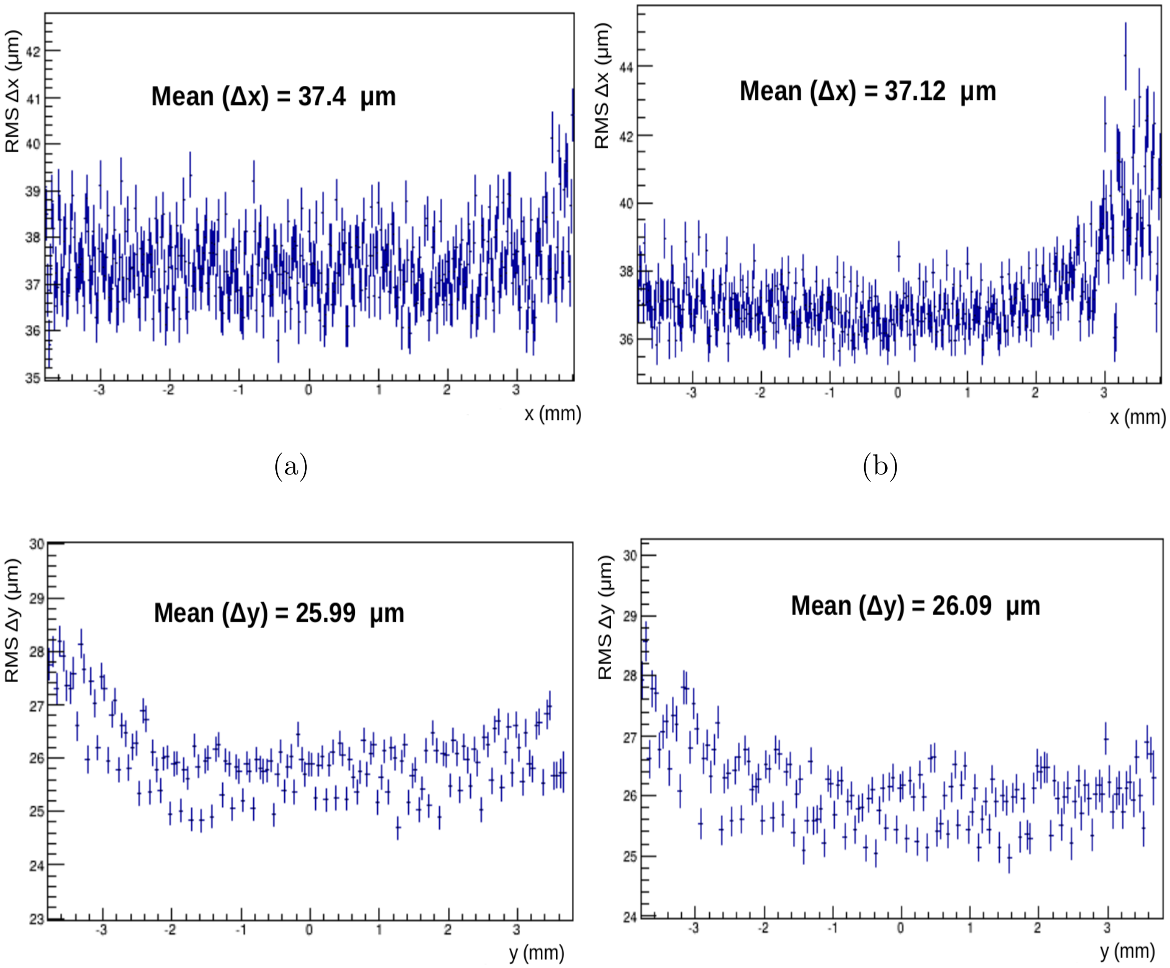

(a) (b)

(c) (d)

Figure 5.32: *Measured resolution for the two unirradiated 3D pixel sensors patterns: In the X coordinate (a) sparse and (b) dense. In the Y coordinate (c) sparse and (d) dense. Sensors are biased to a voltage of 20 V. The resolution improves with respect to the binary prediction, where charge sharing isn't considered (see text).*

both maps, the pn-junction columns are not visible. This result was expected because the electric field is higher at the pn-junction.

A novel result obtained with this study is that the efficiency map is more homogeneous for the sensor with a p-column dense pattern than for the sensor that has the sparse pattern. This shows that the sensor

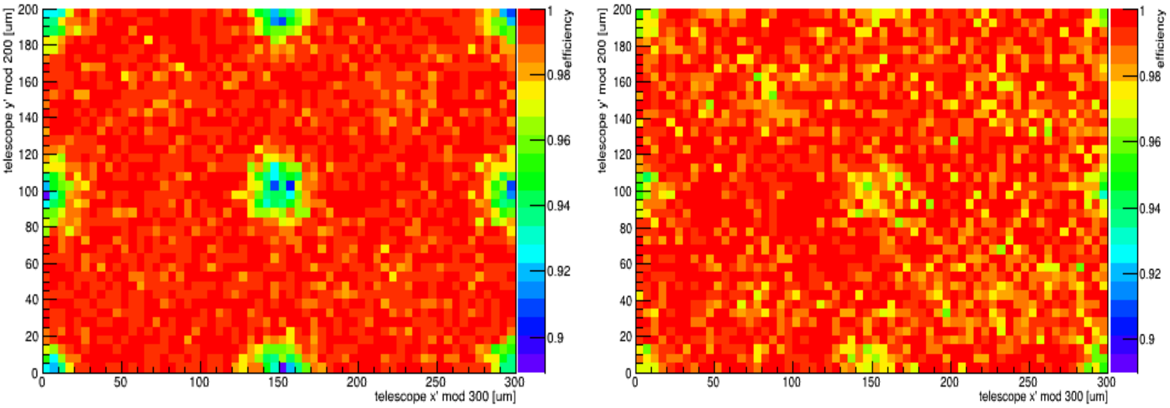

(a) (b)

Figure 5.33: *Efficiency map for the two unirradiated 3D pixel sensors patterns measured in a test beam at DESY: (a) sparse and (b) dense. Sensors are biased to a voltage of 20 V. The sensor including a dense pattern in ohmic columns shows a more homogeneous behavior.*

efficiency can be improved by homogenizing the electric field, adding ohmic columns.

Measurements show a lower drop in efficiency in case of the dense pattern than in the sparse pattern. This result is shown in Figure 5.34, where the detector efficiency is plotted. Every entry of the histogram corresponds to the efficiency average value. Looking at these histograms we can see the different efficiencies in the total area and in the area surrounding the ohmic columns. The efficiency drops from a mean of 99 % to 94 % in the sparse pattern detector, while in case of the detector with dense patterns, the drop is only of 1%.

In both cases, these efficiency drop can be compensated if the incidence of the particle is not perpendicular with respect to the sensor's plane. They are fully avoidable by tilting the sensor or bending the particle trajectory using a magnetic field.

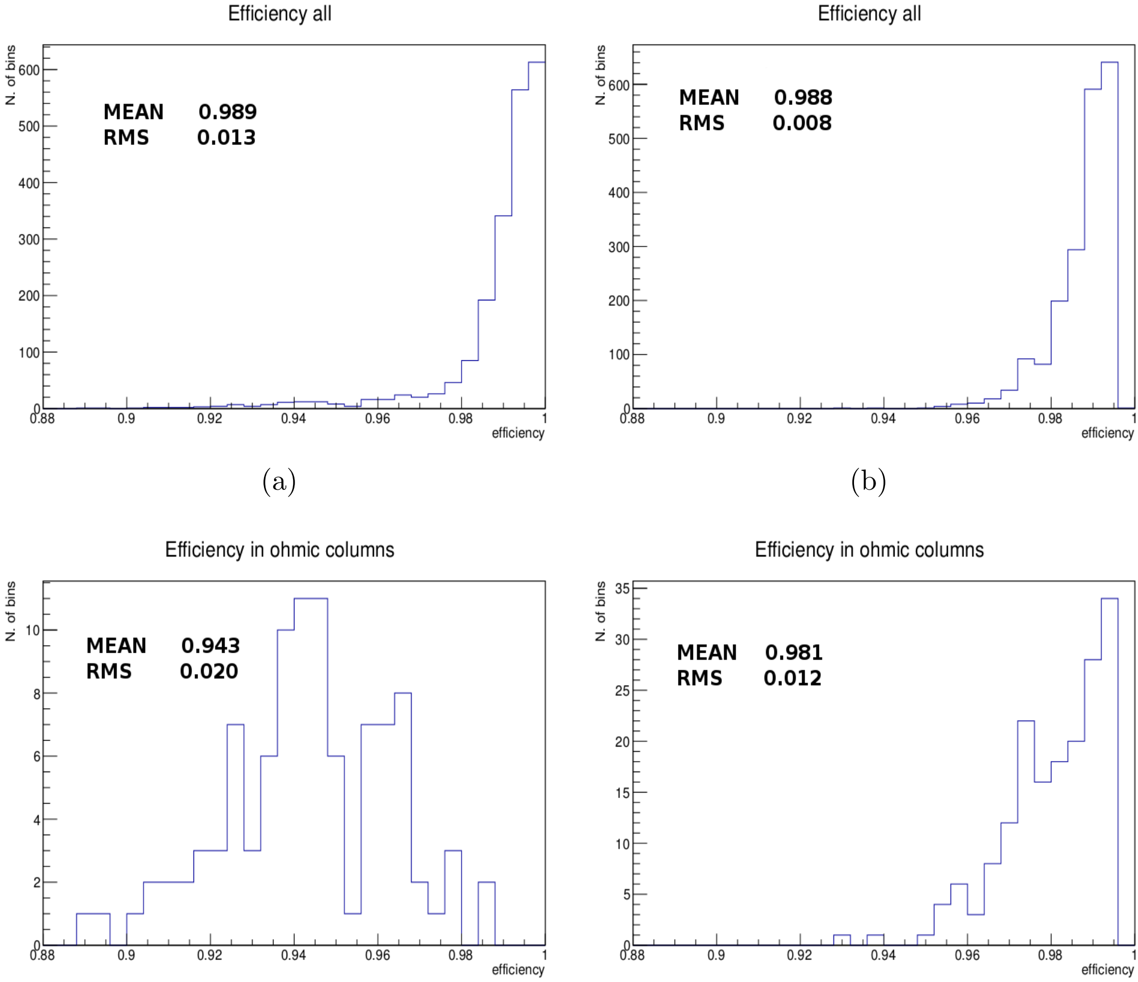

(a) (b)

(c) (d)

Figure 5.34: *Measured efficiency distributions for the two unirradiated 3D pixel sensor patterns: Efficiency in the total area (a) sparse and (b) dense. Efficiency in the ohmic column areas (c) sparse and (d) dense.The drop in efficiency in the ohmic columns is higher in the sensor with sparse pattern.*

5.8.2 Irradiated sensors

The test stand for irradiated samples was the same as described before but with and a N_2 atmosphere. The same measurements were performed but at temperature of about -15℃ and with a constant nitrogen (N_2) flow in order to ensure a relative humidity below 20 % during the test.

The cooling system was integrated by a chiller and two peltier units. With the chiller, a closed water circuit refrigerated the setup. The water was kept a few degrees above zero, to avoid condensation in tubes reaching the electronics. With this test stand in the beam area the lowest reachable temperature on the sensors was approximately -15 ℃.

It is important to keep in mind that the readout chip was irradiated along with the sensor. Therefore, sensor and chip were damaged by radiation. While the radiation damage caused in a sensor is being studied in detail since decades (recent works are [10, 69, 70, 79]), the readout chip damage is not well understood yet.

Two different sensors irradiated with neutrons up to a fluence of $1 \cdot 10^{15}$ n_{eq}/cm^2 were tested. Each one has a different ohmic column pattern. These measurements were done at two different bias voltages.

According to the radioactive source characterization from section 5.7 the irradiated sensors up to $1 \cdot 10^{15}$ n_{eq}/cm^2 deplete at 120 V.

- **Collected charge**

  In Figure 5.35, the charge distributions for both sensor patterns under different bias voltages (120 and 140 V) are shown. We can see how the charge distribution shape changes with voltage, more evident in the case of the dense pattern sensor. For a better understanding of this we have to keep in mind how is the depleted volume growing with the applied voltage. Figure 5.36 show the difference between having a not fully depleted planar and a 3D device. For the same tracks family, in a planar device the charge will maintain a landau distribution because the depleted region is the same for every track but it will be "shifted" to lower values. However, in a 3D sensor there are many tracks with very different charge values (t1 and t3) and even some of them are fully lost (t2) while traversing only undepleted volume. The main consequences of this are, the change on the charge distribution with the applied voltage and the efficiency loss in undepleted volume.

  The charge distribution shape can be due in part to the fact that sensors are not fully depleted and in part to the readout chip calibration after irradiation, which is not fully understood. However, their shape change

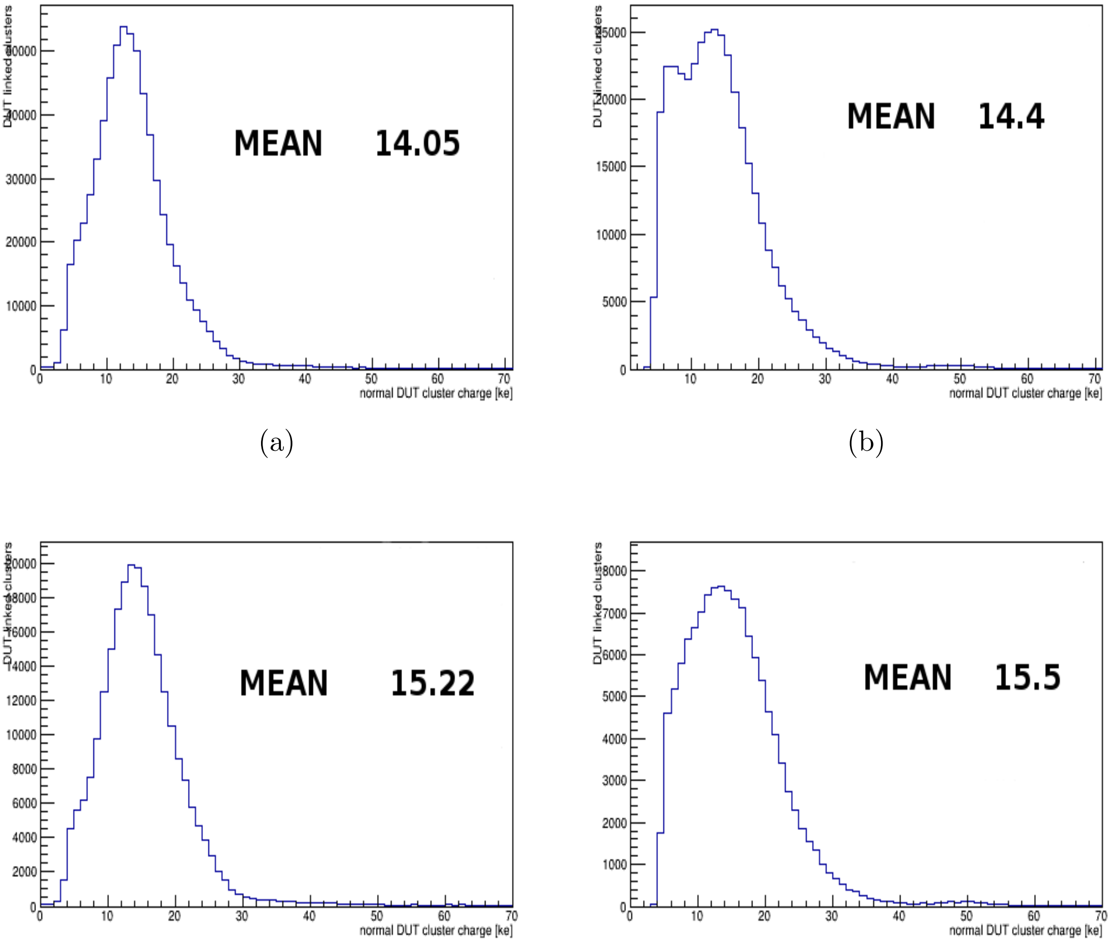

(a) (b)

(c) (d)

Figure 5.35: *Measured charge distribution for the two irradiated 3D pixel sensor patterns: Charge spectrum at 120 V (a) sparse and (b) dense. Charge spectrum at 140 V (c) sparse and (d) dense.*

with voltage can be attributed exclusively to the missing depleted volume.

- **Efficiency maps**

  Efficiency maps are shown in Figure 5.37. We can conclude that the low efficiency stripe between pn-junction columns is not fully depleted even

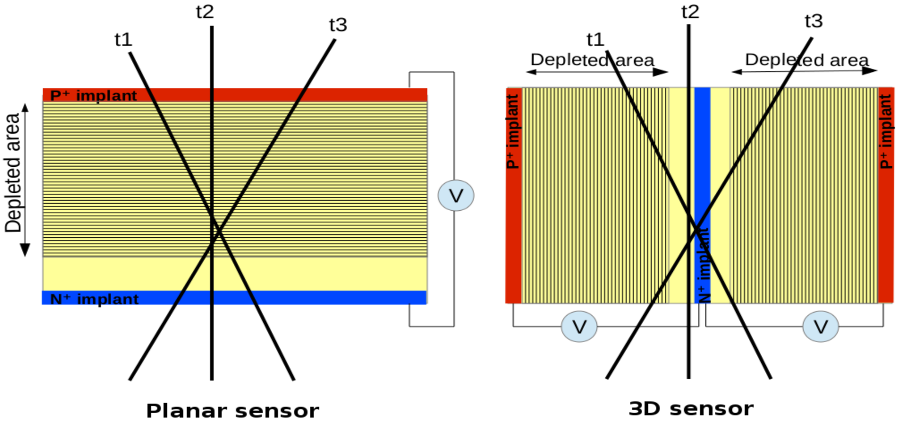

Figure 5.36: *Schematic of the depletion area in not fully depleted planar (left) and 3D devices (right). The same family of tracks is passing through both devices. While in a planar device, the charge distribution will keep the landau distribution but sifted to lower charge, in 3D sensors will suffer efficiency drops (t2) and many tracks with lower energies (t1 and t3).*

at 140 V in both cases. Unfortunately, we don't have data for higher voltages and the data runs applying a bias voltage of 140 V have less entries than those with 120 V.

If we consider only the depleted area the mean value for the efficiency operating at 140 V and with normal incidence are 0.929 and 0.922 for sensors with dense and sparse pattern, respectively.

- **Charge distribution uniformity**
  According to the results obtained and considering that the sensors were not fully depleted, the charge distribution uniformity plot, where the mean value in the cluster charge is represented, show how the electric field is growing in the sensor, starting in the pn column and growing circularly around it (see Figure 5.38).

In terms of charge sharing and resolution, there are not remarkable differences between unirradiated and irradiated samples. Relative to the charge distribution, in case of irradiated detectors, we have two aspects to consider, that sensors were not fully depleted and that the pulse calibration in the read-

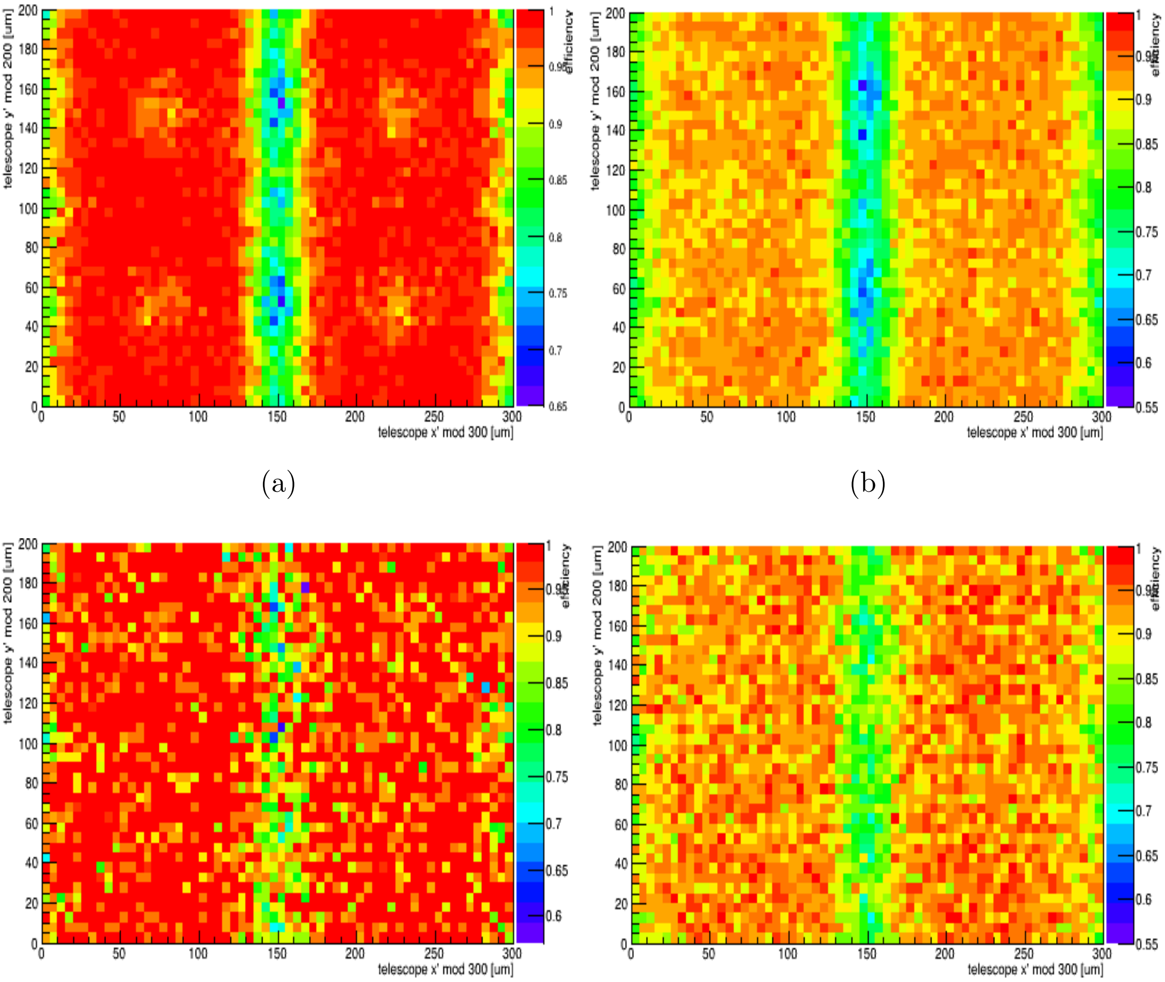

(a)

(b)

(c)

(d)

Figure 5.37: *Measured detection efficiency for the two irradiated 3D pixel sensors patterns: Efficiency maps @ 120 V (a) sparse and (b) dense. Efficiency maps @ 140 V (c) sparse and (d) dense. The low efficiency stripe are due to the partial depletion of the sensors.*

out chip is not fully understood. However, these results allow to map the electric field in a 3D sensor after irradiation.

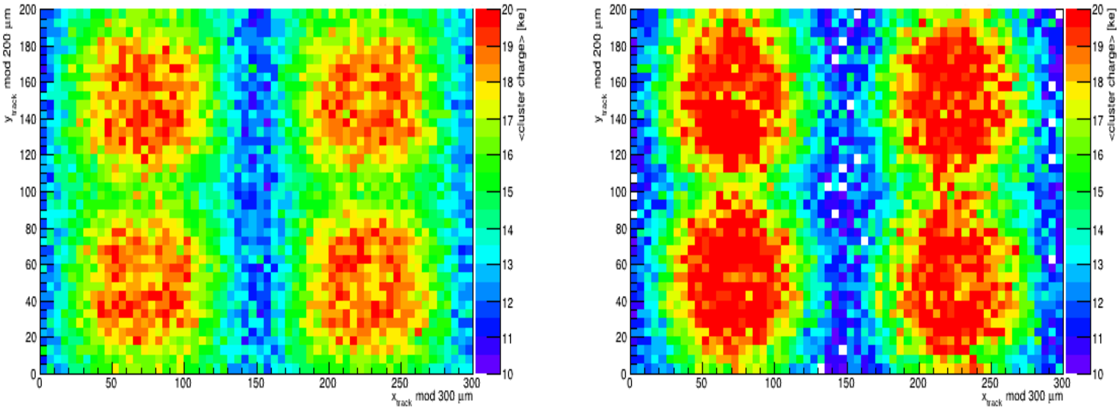

(a)

(b)

Figure 5.38: *Charge distribution uniformity for the two 3D pixel sensors patterns (irradiated up to* $1 \cdot 10^{15}$ n_{eq}/cm^2*) measured in a test beam at DESY: (a) sparse and (b) dense. Sensors are biased to a voltage of 140 V.*

5.9 Summary of the results and next steps

In this chapter, the results obtained from the characterization of 3D double-sided sensors have been presented. This section summarizes the most relevant results and describes some ongoing and future work.

- **Electrical characterization.**
  The homogeneity in the electrical response for manufactured sensors was very high. The required voltage to fully deplete an unirradiated sensor is 20 V. Finally, after the biasing studies we do not observe significant differences between biasing by punch-through and directly cell by cell.

- **Radioactive source characterization.**
  With the radioactive source we were able to measure the charge collection efficiency for either unirradiated or irradiated samples up to a fluence of $5 \cdot 10^{15}$ n_{eq}/cm^2. For this high fluence, the read out chip is highly dependent on temperature and its calibration becomes more difficult. This is the reason why we only tested one sample irradiated up to this dose.

We measured the collected charge and the newly defined *relative efficiency*. From those measurements we extracted the operation voltage values (V_{op}) for the different samples.

  - Unirradiated samples $\Longrightarrow V_{op} = 20$ V.
  - Irradiated samples up to 1 $\cdot 10^{15}$ $n_{eq}/cm^2 \Longrightarrow V_{op} = 120$ V.
  - Irradiated samples up to 5 $\cdot 10^{15}$ $n_{eq}/cm^2 \Longrightarrow V_{op} = 180$ V.

These results were published in [147].

- **Beam characterization.**
  In this characterization we operated the detectors at the operating voltages obtained from the radioactive source characterization measurements.

  As a novel result, the unirradiated detectors show that in terms of sensor efficiency, adding columns doesn't imply an efficiency loss. Moreover, the electric field is more homogeneous in the bulk with shorter distances between ohmic columns and junction columns. In terms of charge collection we did not observe a clear performance difference between both patterns.

  The irradiated detector results show that the depleted or active area in the sensors was not maximal. We need to go to higher voltage values to operate these sensors. The reason why we did not observe that in the radioactive source characterization is because in the test beam we really had normal tracks to the sensor surface, however in the radioactive source characterization (with an ^{90}Sr source), we have also oblique tracks that can hide this effect.

Next steps. A still ongoing work is the data analysis on irradiated devices, that has to be improved in order to try to correct (offline) some of the radiation damages suffered by the read out chip.

A new sensor production is being planned, taking into account the results here presented in this dissertation:

- Including an extra passivation layer to avoid stress issues during sensor handling and especially during bump bonding and reflow.

- Trying a different bump bonding technique to avoid Indium adhesions into the column holes that can generate differences in the connection conductivity.
- The necessity of having a read out chip able to work after the irradiation dose expected at HL-LHC is essential to characterize the 3D sensor performance.
- Making a correct estimation of depletion voltage for irradiated samples. For example by means of the Transient Current Technique (TCT).

Chapter 6

Conclusions

The research reported here assessed the performance of two kinds of novel sensors for their application in tracker detectors for future collider experiments. For the first time, the charge division concept has been implemented on microstrip silicon sensors; concerning the 3D pixel sensors, a new layout of electrode columns and a sensor biasing structure were assessed.

On one hand a novel device has been characterized, which is a two dimensional position sensitive microstrip sensor. This sensor is based on the resistive charge division principle. In standard microstrip sensors, the electrodes are made of Aluminum, while in this concept the electrode material is highly doped polycrystalline silicon. The strips are readout from both electrode ends simultaneously. In this way, the transversal coordinate is given by the capacitive charge sharing between strips and the longitudinal coordinate from the resistive charge division in an electrode. The longer the distance the signal travels along the strip, the more attenuated is the amplitude readout. Therefore, one can compare the signal amplitudes at both electrode ends and determine the particle impact point. Recently, the use of the charge-division method in very long microstrip sensors -several tens of centimeters- has been proposed as a possible tracking technology for the ILC experiments [11].

The other kind of studied sensors are pixel sensors. These sensors *3D double-sided double-type sensors.* The 3D sensors have cylindrical vertical electrodes that penetrate into the detector bulk [73]. Electrons and holes, moving parallel to the sensor surface, are then collected at the respective electrodes. Carrier drift time and device depletion voltage are determined by the electrode spacing. Depending on the electrode's pitch the charge carriers generated by ionizing radiation can be collected within a time smaller than the trapping time of the radiation-induced defects [132]. This makes them more radiation resistant than planar sensors and one of the technology candidates to replace the current vertex detector sensors in the HL-LHC [9] scenario where the particle fluence will increase considerably.

Both technologies were characterized electrically. The two-dimensional position-sensitive microstrip sensors were mainly characterized with a laser allowing to study in detail both, resistive charge division and noise. In case of 3D pixel sensors, the main characterizations were done with a radioactive source and a particle beam either in irradiated or unirradiated samples to study the sensor radiation resistance.

- The performance of two different two-dimensional position-sensitive microstrip sensor prototypes with different resistances of the electrodes (R/l = 2.8 Ω/µm and R/l = 12.2 Ω/µm) was studied (results are published in [13]). Results show that accordantly with the simulation the position resolution along the longitudinal coordinate for a signal of about 6 MIPs is 225 µm and 232 µm for the low and high resistive electrode sensors, respectively, confirming the non dependence of the resolution with the resistance. The electrical simulations of the detector and front-end electronics are able to reproduce experimental results in reconstructing the fractional position of the signal generation point. This validates the simulation as an adequate tool for future sensor designs. Comparing experimental and simulated measurements, we studied the signal propagation effects: signal attenuation and broadening of the signal. Both effects cause a systematic non constant ballistic deficit when a non optimized front-end electronics is used to readout the signal. With the radioactive characterization using a ^{90}Sr source, we measured a signal to noise ratio (SNR) of about 12 for the sensor with low resistive electrodes.

  The possibility of reading out the detector from only one side of it was also studied integrating an Aluminum routing line to drive the signal (published in [59]). This prototype showed the importance of having a good insulation between implants with respect to the metal routing to reduce parasitic capacitances inducing signal cross-talk.

In order to optimize the future prototype performance several factors have to be taken into account:

- The detector spatial resolution depends on the signal to noise ratio. The optimal shaping time to maximize the SNR comes from a trade-off between the opposite requirements of the serial and parallel resistance noise terms.
- The electrode resistance should be as small as possible; minimizing the signal attenuation while still resolving the amplitude differences at the end of the strip electrode. A detailed position resolution study was developed in reference [60].

The above aspects can be optimized using the developed simulation.

- The performance of double-sided 3D pixel sensors before and after irradiation was studied. Results obtained from the electrical characterization show a high homogeneity and a full depletion voltage about 10 V. After a biasing study, we did not observe significant differences between biasing by punch-through and directly cell by cell through a polysilicon resistor grid.

  Measuring the sensor response to a radioactive source we obtained the charge collection efficiency for both unirradiated and irradiated samples up to a fluence of $5 \cdot 10^{15}$ n_{eq}/cm^2. We measured the collected charge and the *relative efficiency* under a low humidity (HR < 20%)atmosphere and temperature (- 20 °C) extracting the appropriated operation voltages (V_{op}) to collect the total charge. The collected signal is reduced with fluence. For samples irradiated up to $1 \cdot 10^{15}$ n_{eq}/cm^2 the signal reduction was about 30 % and for irradiated samples up to $5 \cdot 10^{15}$ n_{eq}/cm^2 the reduction is about 60%. In the characterization at the DESY test beam facilities, we operated the detectors at the operating voltages obtained from the radioactive source characterization and we studied the sensor efficiencies. As a novel result, the unirradiated detectors show that in terms of sensor efficiency, adding columns does not imply an efficiency loss and in terms of charge collection we do not observe a clear difference between the Landau distributions. In case of irradiated detectors, the reduction on the collected charge with fluence is the same than the obtained with radioactive source characterization. The irradiated samples were not operated at the right voltage and depleted area was not maximized. We need to go to higher voltage values to operate these sensors. The test beam data analysis on irradiated devices has to be improved and completed in order to try to correct (offline) some of the radiation damages suffered by the read out chip. A new sensor production is being planned, taking into account the results presented here.

Resumen

1 Motivación e Introducción

El Gran Colisionador Hadrónico o LHC (por sus siglas en inglés) [3] está operando satisfactoriamente desde finales del año 2010 en el Laboratorio Europeo de Física de Partículas (CERN). El LHC es un colisionador circular de partículas que acelera protones o iones de plomo hasta que alcanzan velocidades cercanas a la velocidad de la luz y luego las hace colisionar en diferentes lugares a lo largo del acelerador. En cada uno de esos puntos de colisión hay un experimento, ALICE, LHCb,CMS y ATLAS. ALICE estudia las colisiones de iones y su cometido es reproducir los primeros instantes del universo. LHCb [5] estudia la física de las partículas que están formadas por un quark b (beauty) con el propósito de entender por qué el universo muestra predilección por la materia frente a la antimateria. Finalmente hay dos experimentos de propósito general, CMS [6] y ATLAS [7]. CMS y ATLAS anunciaron el 4 de Julio de 2012 el descubrimiento de una nueva partícula, el bosón de Higgs.

Los experimentos que se necesitan para la medida de propiedades y el descubrimiento de partículas son de grandes dimensiones y suelen tener una estructura de capas también llamada “de cebolla”. Un ejemplo de ello es el experimento CMS, la Figura 1.1 muestra una sección transversal del mismo y las trazas que las partículas dejan a su paso por los distintos detectores según su naturaleza. En la capa más interna, como se muestra en la figura, se encuentra el detector de trazas compuesto de varias capas de detectores de silicio. En la zona intermedia, se encuentran los calorímetros electromagnético y hadrónico y en la capa más externa se encuentran las cámaras de muones.

La interacción de las partículas con los diferentes detectores permite conocer su identidad y su energía. Un múon, por ejemplo, interactúa con el detector de trazas y las cámaras de muones fundamentalmente mientras que un fotón lo hará sólamente con el calorímetro electromagnético. En el caso de partículas cargadas además debido al campo magnético de cuatro Teslas generado mediante un solenoide, su trayectoria se curvará y lo hará en mayor medida cuanto menor sea su momento (energía).

En esta tesis se estudian nuevas tecnologías que tienen cabida en futuros detectores de trazas de silicio. Los detectores de trazas están compuestos por varias capas de sensores de silicio. Las capas más internas están compuestas por detectores de píxeles, que tienen una alta granularidad para poder resolver vértices secundarios. Las capas más externas están formadas por detectores de microtiras, donde la granularidad es menor, pero suficiente para reconstruir trazas con una resolución por debajo de diez micras.

Los detectores de silicio semiconductores se usan en física de altas energías desde hace treinta años [8] y se han convertido en una tecnología estándar en detectores de trazas. Las características que tiene que tener un detector para formar parte de un detector de trazas son: alta granularidad para tener la mejor resolución en la medida de la posición, que el sensor sea sensible a una pequeña cantidad de energía y que sea resistente a radiación. Al mismo tiempo, el experimento requiere que la cantidad de material sea la menor posible para disminuir, en la medida de lo posible, el scattering múltiple de partículas. En detectores de silicio, se dan estas condiciones y además, al ser un material muy usado en otras aplicaciones (como las telecomunicaciones) es más accesible tanto tecnológica como económicamente que otros materiales semiconductores como por ejemplo, el diamante.

Sin embargo, las características que tienen que cumplir los detectores de silicio para operar en futuros conlisionadores son más exigentes y dependen del tipo de colisionador. Los futuros colisionadores tendrán luminosidades más altas, aumentando el flujo de partículas en los detectores como es el caso del Gran Colisionador de Hadrones de Alta Lunminosidad (HL-LHC) [9]. O bien serán aceleradores lineales leptónicos, cuya principal característica es que son capaces de hacer medidas de propiedades de partículas con una gran resolución. Éste es el caso del Colisionador Lineal Internacional (ILC) [11].

En los detectores de silicio, aumentar la resolución se traduce en desarrollar nuevos detectores más resistentes a radiación para lidiar con altas luminosidades en el HL-LHC, o en el caso del ILC hay que desarrollar detectores de mayor granularidad disminuyendo al máximo el material necesario, evitando el scattering y aumentando la resolución en la medida.

Como referencias para el estudio detallado de la física de detectores semiconductores son señalables los libros: H. Spieler [66], G.F. Knoll [67] y G. Lutz [68]. En cuanto al desarrollo de nuevos detectores en física de altas energías, los siguientes artículos [8], [17], [18] resumen el estado de la tecnología en detectores de silicio. Mientras que como bibliografía específica en resistencia a radición en detectores de silicio tres tesis son una referencia: Michael Moll [69], Gregor Kramberger [70] and Nicola Pacifico [71].

En el capítulo 1 de esta tesis se incluye un resumen del estado actual de la tecnología en detectores de silicio y en el capítulo 2 un estudio detallado de la física de detectores semiconductores y de el deterioro que produce en ellos la radiación. Estos dos capítulos sirven para establecer tanto el contexto de este trabajo como las bases para su completo entendimiento.

2 Descripción de dispositivos

Los detectores de silicio son diodos estándar que se usan en física de altas energías como fotodetectores o como detectores de trazas. Como detectores de trazas, nos proporcionan información sobre la posición de la partícula en el plano del detector cuando ésta pasa por él. Para conseguir la mayor resolución en la medida los detectores están segmentados, bien en microtiras o en píxeles (ver Figura 2.3). La anchura de las tiras en un detector de microtiras suele ser menor de cien micras y los detectores de píxeles objeto de estudio en esta tesis son rectangulares y tienen un tamaño de 100 µm × 150 µm. La segmentación del sensor puede ser en la parte de la unión pn, tal y como se ve en la figura o también en la parte de la unión óhmica dependiendo de la aplicación.

Las diferentes formas de leer ambos dispositivos son también visibles en la Figura 2.3, los sensores de microtiras son leídos desde un lateral del mismo, mientras que un sensor de píxeles necesita una lectura “uno-a-uno”, es decir el chip de lectura tiene que estar conectado celda a celda con cada píxel del sensor a modo “sandwich”, haciendo necesarias técnicas específicas para interconectar el sensor con el chip de lectura. La técnica más usada es conocida como "bump-bonding" [29]. En esta tesis se presentan los resultados obtenidos en la cualificación de dos nuevos sensores para su implementación en detectores de trazas de futuros colisionadores.

2.1 Detectores de microtiras sensible en dos coordenadas

Este detector consiste en un nuevo sensor de microtiras que incluye electrodos resistivos en lugar de los metálicos permitiendo obtener información de dos coordenadas de la posición en un único sensor (ver Figura 4.3). Por un lado, obtenemos la posición en la coordenada transversal a las tiras gracias a la división de carga entre las mismas. Por otro lado, dado que el electrodo es resistivo y que es leído por sus dos extremos, comparando la amplitud de las señales podemos determinar la posición en la coordenada paralela a las microtiras.

Estos detectores tienen aplicaciones en diferentes campos, además de en física de partículas, se usan en el monitorizado de haces, ya sean de láser o de partículas para alineamiento o terapias hadrónicas. En esta tesis se han caracterizado detectores con diferente resistividad en los electrodos y también prototipos que incluyen un *routing* de metal para poder leer todos los canales del detector desde un mismo lado del sensor.

2.2 Detectores de píxeles con tecnología 3D

Estos sensores están formados por píxeles, donde en lugar de contar con electrodos en la parte superior e inferior del sensor (como ocurre con tecnología planar), cuentan con electrodos verticales. A este tipo de tecnología también se le da el nombre de tecnología 3D y ha demostrado ser más resistente a radiación y necesitar voltajes de operación más pequeños que la tecnología estándar o planar. En la Figura 2.4 podemos ver las diferencias estructurales entre un sensor fabricado en tecnología planar y tecnología 3D. En un sensor 3D los electrodos atraviesan todo o parte del espesor del sensor, reduciendo así la distancia entre ellos mientras que en el caso de un sensor planar la distancia entre electrodos coincide con el espesor del sensor.

En esta tesis, se han caracterizado píxeles 3D con dos diferentes distribuciones de columnas óhmicas (tipo p) tanto irradiados como sin irradiar. Además, una de las obleas de sensores fabricadas incluye una red de polarización que permite polarizar celda a celda en lugar de únicamente por difusión a través del anillo de polarización.

3 Técnicas de Laboratorio

Para conocer el funcionamiento y características de estos sensores como detectores de partículas usamos diferentes técnicas:

- Caracterización eléctrica. Este tipo de caracterización es la que se lleva a cabo inmediatamente después de una producción de sensores. Consiste en comprobar que los parámetros eléctricos diseñados prevalecen en el producto final. Las medidas más características son:
  - La medida de la corriente de vaciado del sensor a lo largo de una rampa de voltaje o curva IV. Con ésta medida podemos saber el grado de pureza del silicio y cuál es el voltaje de ruptura del sensor.
  - La medida de la capacidad del sensor en una rampa de voltaje o curva CV. Esta medida nos permite medir el voltaje que es necesario aplicar para vaciar el sensor de portadores de carga libres o para crear la mayor área activa posible (en el caso de sensores irradiados).
  - Resistencias y capacidades de los diferentes componentes del sensor. Midiendo estos parámetros, podemos caracterizar los diferentes acoplos que hay entre los mismos que pueden provocar pérdidas de carga o señal.
- Caracterización con láser. Usando este método, se realizan barridos con el haz láser en la superficie del sensor de microtiras. De esta manera pudimos demostrar el principio de operación del sensor, la división de carga resistiva. Con esta técnica también somos capaces de hacer una primera estimación de la resolución del sensor en la medida de la posición a lo largo del electrodo resistivo.
- Caracterización con fuente radioactiva. Midiendo la respuesta de los

sensores con una fuente radioactiva ^{90}Sr medimos la razón señal-ruido y la eficiencia del sensor en la colección de carga.

- Caracterización con un haz de partículas. En un *test beam* en DESY [102] (Hamburgo) y con la ayuda de un telescopio [105] pudimos estudiar la efficiencia de detección y resolución de los detectores de píxeles 3D.

En el caso de los sensores de microtiras, los detectores además han sido simulados usando SPICE [118] implementando en la simulación los resultados obtenidos en la calibración eléctrica.

4 Resultados

Los resultados obtenidos para cada uno de estos tipos de detectores se resumen en esta sección.

4.1 Detectores de microtiras sensible en dos coordenadas

En el caso de los detectores de microtiras con electrodos resistivos los resultados más destacados son:

- La resolución en la medida de la posición en la coordenada longitudinal al electrodo es del orden de 225 y 232 µm para las dos resistividades estudiadas de $R/l = 2.8\ \Omega/\mu m$ y $R/l = 12.2\ \Omega/\mu m$, respectivamente.
- Tanto la simulación del detector, como las medidas experimentales muestran los efectos de la resistividad del electrodo en la propagación de la señal, esos efectos son: atenuación de la amplitud de señal y retardo del tiempo de pico (o *peaking time*). Estos resultados indican la necesidad de optimizar la electrónica de lectura para colectar la señal correctamente y evitar el deficit balístico [58].
- En cuanto a la razon señal−ruido, ésta es del orden de 13, que es menor que la que se obtiene con sensores de microtiras con electrodos metálicos. Esta razón podrá ser aumentanda usando lo aprendido con los resultados obtenidos con estas caracterizaciones, disminuyendo la resistividad de los electrodos, disminuyendo el ruido y optimizando la electrónica de lectura.

- En lo que tiene que ver con el prototipo que incluye un “routing” metálico, hemos encontrado acoplamientos capacitivos que han de ser evitados en futuros diseños.

- Un estudio detallado del ruido en sensores de microtiras resistivas fue también llevado a cabo .

- La simulación de los sensores reproduce los resultados experimentales y es una herramienta muy útil para el diseño de nuevos sensores que incluyan electrodos resitivos.

El trabajo realizado con sensores de microtiras resistivas dió lugar a varias publicaciones donde hay una descripción más detallada, tanto de los dispositivos caracterizados como de los resultados obtenidos [13, 59, 60].

4.2 Detectores de píxeles con tecnología 3D

En el caso de los detectores de píxeles en tecnología 3D los resultados más destacados son:

- No hay diferencias significativas en las medidas eléctricas entre polarizar sensores usando el anillo de polarización o celda a celda.

- De las medidas de eficiencia de colección de carga con una fuente radioactiva se obtuvieron los voltaje de polarización, que son:
  - Sensores sin irradiar $\Longrightarrow$ $V_{op} = 20$ V.
  - Sensores irradiados a $1 \cdot 10^{15}$ $n_{eq}/cm^2 \Longrightarrow V_{op} = 120$ V.
  - Sensores irradiados a $5 \cdot 10^{15}$ $n_{eq}/cm^2 \Longrightarrow V_{op} = 180$ V.

- En las medidas de eficiencia de los sensores en un haz de partículas con incidencia normal, se encontró que:
  - En sensores no irradiados. Aumentando el número de columnas óhmicas la respuesta del sensor es más homogénea y no disminuye la eficiencia.

  - En sensores irradiados. No se consiguió vaciarlos totalmente operándolos a los voltajes obtenidos como resultado de la caracterización con fuente radioactiva. La razón de este resultado es que midiendo con una fuente radioactiva consideramos también trazas con incidencia oblícua que en cierto modo pueden *"esconder"* las areas más ineficientes del sensor.

El trabajo realizado con sensores de píxeles 3D fue publicado en [147].

5 Conclusiones

Resumiendo, con el trabajo presentado en esta tesis por primera vez se ha implementado el concepto de división de carga en sensores de silicio; en cuanto a los sensores 3D, hemos estudiado un nuevo esquema de electrodos y su efecto en el comportamiento del sesor y se ha implementado una red resistiva para hacer estudios de polarización. Resultados de este trabajo a destacar son:

- El desarrollo de una herramienta de simulación para el diseño de nuevos detectores de microtiras resistivas que reproduce los resultados experimentales.

- La completa caracterización de la respuesta de sensores con electrodos resistivos usando un haz láser y fuente radioactiva, siendo capaces de medir la resolución del detector a lo largo del electrodo. Esta resolución es del orden 10% de la longitud del mismo.

- No hemos medido diferencias sustanciales entre la medida de corriente de vaciado usando el método de "punch-trough" o la red resistiva (celda a celda).

- Se ha caracterizado y medido sistemáticamente la eficiencia de colección de píxeles 3D irradiados y sin irradiar en laboratorio, haciendo uso de una fuente radioactiva, y con un haz de positrones en DESY. Hemos sido capaces de evaluar cuantitativamente la pérdida de señal en los sensores por efecto del deterioro que los mismos sufren tras la irradiación.

- No hemos apreciado un deterioro en eficiencia del sensor cuando se añaden electrodos en sensores 3D, sino que observamos una mayor homogeneidad.
- Las resultados obtenidos ayudarán y serán tenidos en cuenta para la optimización de nuevos diseños de sensores.

List of Figures

1.1 Schematic of the CMS experiment 2
1.2 Basic structures of p-on-n type sensors 6
1.3 DC and AC couplings 7
1.4 FOSTER sensor 10
1.5 Layout of an integrated pitch adapter 11
1.6 Schematic of a hybrid pixel sensor 12
1.7 Bump-bonding technique 13
1.8 SLID process 14
1.9 Collected charge for proton (26MeV) irradiated planar detectors biased at 900 V 18
1.10 Radiation damage compensation 18
1.11 DEPFET pixel sensor 21
1.12 CMOS Pixel Sensor. CPS 22
1.13 Structure of a SOI sensor 23
1.14 Structure of a HV-CMOS sensor 24
1.15 Structure of a sensor in 3D integration technology 25
1.16 Structure of an APD sensor 28

2.1 pn junction description 35
2.2 Structure of a diode p-on-n type 38
2.3 Layout of p-on-n type segmented detectors 39
2.4 Inner structure of p-on-n type sensor 40
2.5 Block diagram of sensor, preamplifier, shaper and digitizer . . . 43
2.6 Electronic components in the preamplifier and shaper 44
2.7 Simulation of defects formation in silicon by different particles . 50

2.8 N_{eff} and V_{fd} variation with irradiation fluence in a FZ p-on-n sensor . . . 52

3.1 Details of a microstrip detector where the different structures that compose it are visible . . . 57
3.2 Picture of one area of a 2D position-sensitive microstrip sensor 58
3.3 Measurement of the current dependence with the reverse bias voltage in two 1 cm^2 diodes. IV curve . . . 59
3.4 Measurement of the 1/C^2 dependence with the bias voltage. CV curve . . . 61
3.5 TSCAP structure layout . . . 62
3.6 CV curve for a MOS structure . . . 63
3.7 Zoom of one extreme of the CAP-TS-AC structure layout . . . 64
3.8 Zoom of one extreme of the CAP-TS-DC structure layout . . . 65
3.9 Zoom of one extreme of a sheet structure with different materials and geometries . . . 66
3.10 Photography of the laser test-stand at IFCA laboratory . . . 68
3.11 Laser beam focusing strategy . . . 69
3.12 Beta decay energy spectrum for Yttrium-90 . . . 70
3.13 Bethe-Bloch graph for beta electron absorption in silicon . . . 71
3.14 PCB sensor board with a 3D pixel sensor set on top of it . . . 72
3.15 Test-stand for a radioactive source characterization at PSI laboratory . . . 72
3.16 AIDA telescope at the DESY line 21 . . . 74
3.17 Photography of a sensor board plug into the test board . . . 76
3.18 Beam profile visible on an unirradiated 3D-pixel detector during a test beam at DESY facilities . . . 77

4.1 Basic structure of a standard strip detector p-on-n type . . . 80
4.2 Photo of a wafer including a 2D position-sensitive sensor . . . 82
4.3 Novel 2D position-sensitive microstrip sensor . . . 83
4.4 IV and CV curves in 2D position sensitive microstrip sensor diodes test structures . . . 85
4.5 IV curves comparative . . . 85
4.6 Sensor in an Alibava daughter board . . . 87

4.7 Schematic of one of the 80 cells used to model the detector . . 88
4.8 Schematic of the modeled front-end 88
4.9 Simulated signal input 89
4.10 Attenuation of the signal read at the entrance of the preamplifier 89
4.11 Simulated fractional position against the actual one and residuals 90
4.12 Gaussian distribution of the sensor signal 91
4.13 Laser pulse shapes 92
4.14 Peaking time displacement with position 93
4.15 Experimental and simulated fractional position results 93
4.16 Experimental and simulated residuals results 94
4.17 Raw distributions of pedestals for A_1 and A_2 99
4.18 correlation parameter for A_1 and A_2 100
4.19 Noise values for the A_1 signal along the strip scanning points . 101
4.20 Correlation coefficients ρ at the different scan points 101
4.21 Fractional position measurement error at each scanning point . 102
4.22 Signal to noise distribution in a 2D position-sensitive sensor . . 103
4.23 2D position-sensitive sensors prototypes including metal routing 104
4.24 Alibava Daughter board reading two prototypes including the Aluminum routing 105
4.25 Schematic of the measurement and results 106
4.26 Fractional position in sensors with routing 107
4.27 Pictures of some details of the new designs 108

5.1 n-on-n pixel sensor structure 113
5.2 Photo of four pixel cells from the CMS barrel vertex detector . 113
5.3 Photo of one of the produced wafers in 3D technology 115
5.4 Sensor pixel cells including polysilicon bias grid and SEM picture of one pixel cell 116
5.5 Diagrams of the two different p-column patterns 117
5.6 Schematic of a 3D double sided detector 118
5.7 Microscope pictures of 3D pixel sensors 118
5.8 Schematic of the fabrication process of double-sided 3D silicon detectors 119
5.9 Current voltage characteristics of the sensors in one 3D-wafer . 120

5.10 Current voltage characteristics of one sensor with the polysilicon bias grid 121
5.11 1/C^2 voltage characteristics of 3D pad detectors 122
5.12 Stability measurement for two 3D pixel sensors 123
5.13 PSI46 readout chip for the CMS pixel detector 124
5.14 Schematic of a pixel unit cell 125
5.15 Readout sequence of a PSI46 ROC 126
5.16 Histogram of the sampled address levels of a ROC 127
5.17 SEM pictures of Indium bumps 128
5.18 SEM pictures of indium bumps before and after flip chip 129
5.19 Schematic of the relevant components for the bump bonding test 130
5.20 Bump-bonding test result for two different 3D pixel sensors . . 132
5.21 Hit occupancy maps for two different sensors after a second reflow 133
5.22 *Tornado* plot for a pixel unit ROC 134
5.23 Pixel map for a ROC 134
5.24 Vcal distribution for a ROC before and after trimming 135
5.25 Cluster charge distribution for the two 3D pixel sensor patterns before irradiation 138
5.26 Most Probable Value against bias voltages in irradiated samples 139
5.27 Normalized relative Efficiency, E$_r$, against bias voltage 139
5.28 Schematic of the DESY test beam setup 141
5.29 Cluster charge distribution for the two unirradiated 3D pixel sensor patterns measured in a DESY test beam 142
5.30 Charge collection uniformity for the two unirradiated 3D pixel sensor patterns measured in a test beam at DESY 143
5.31 Charge sharing map for the two unirradiated 3D pixel sensor patterns measured in a DESY test beam 144
5.32 Measured resolution for the two unirradiated 3D pixel sensors patterns 145
5.33 Efficiency map for the two unirradiated 3D pixel sensors patterns measured in a DESY test beam 146
5.34 Measured efficiency distributions for the two unirradiated 3D pixel sensor patterns 147

5.35 Measured charge distribution for the two irradiated 3D pixel sensor patterns 149
5.36 Schematic of the depletion area in not fully depleted planar and 3D devices 150
5.37 Measured detection efficiency for the two irradiated 3D pixel sensors patterns 151
5.38 Charge distribution uniformity for the two irradiated 3D pixel sensors patterns 152

List of Tables

1.1 State of the art table 30

4.1 Microstrip detector parameters 86
4.2 Measured electrical parameters of the detector prototype 103
4.3 List of values used in the simulation of the sensor's equivalent circuit. 104

5.1 Name, quantity and description of the devices included in each wafer 120

Bibliography

[1] LEP. Large electron positron collider. *http://public.web.cern.ch/public/en/research/lep-en.html.*

[2] Tevatron. Tevatron website. *http://www.fnal.gov/pub/tevatron/.*

[3] Oliver Sim et al. Brning. LHC Design Report, CERN-2004-003. 1998.

[4] ALICE Collaboration. ALICE Technical Design Report, ALICE-TDR. 2001.

[5] LHCb Collaboration. LHCb Magnet: Technical Design Report, LHCb-TDR. 2000.

[6] The CMS Collaboration. CMS Technical Design Report, CMS-TDR. 1998.

[7] ATLAS Collaboration. ATLAS technical design report, ATLAS-TDR. 1998.

[8] Hans-Günther Moser. Silicon detector systems in high energy physics. *Progress in Particle and Nuclear Physics*, 63(1):186 – 237, 2009.

[9] F. Gianotti et al. Physics potential and experimental challenges of the LHC luminosity upgrade. *European Physical Journal C*, 39(3):293 – 333, 2005.

[10] M. Moll. Development of radiation hard sensors for very high luminosity colliders- CERN-RD50 project. *Nucl. Instr. and Meth. A*, 511(1-2):97 – 105, 2003.

[11] ILC. International linear collider website. *http://www.linearcollider.org/ILC.*

[12] ILC Collaboration. ILC detectors. *http://www.linearcollider.org/ILC/physics-detectors/Detectors.*

[13] D. Bassignana et al. First investigation of a novel 2D position-sensitive semiconductor detector concept. *Journal of instrumentation, 2012 JINST 7 P02005.*

[14] Institut Jozef Stefan. Ljubljana irradiation facilities. *http://www-rcp.ijs.si/main/en/index.html.*

[15] Karlsruhe Institute of Technology. Karlsruhe irradiation facilities. *http://www.anka.kit.edu/english/legals.php.*

[16] Markus Friedl. *The CMS Silicon Strip Tracker and its Electronic Readout.* PhD thesis, Vienna University of Technology, 2001.

[17] F. Hartmann. Silicon tracking detectors in high-energy physics. *Nucl. Instr. and Meth. in Phys. Res. A*, 666(0):25 – 46, 2012. Advanced Instrumentation.

[18] M. Battaglia et al. R&D paths of pixel detectors for vertex tracking and radiation imaging. *Nucl. Instr. and Meth. in Phys. Res. A 716 (2013) 29.*

[19] M.J. French et al. Design and results from the APV25, a deep submicron CMOS front-end chip for the CMS tracker. *Nucl. Instr. and Meth. in Phys. Res. A 466 (2001) 359.*

[20] Marko Dragicevic. *The New Silicon Strip Detectors for the CMS Tracker Upgrade.* PhD thesis, Institut für Hochenergiephysik der Österreichischen Akademie der Wissenschaften und am Atominstitut der Österreichischen Universitäten, 2010.

[21] R. Turchetta. Spatial resolution of silicon microstrip detectors. *Nucl. Instr. and Meth. in Phys. Res. A*, 335(12):44 – 58, 1993.

[22] E. Belau et al. Charge collection in silicon strip detectors. *Nuclear Instruments and Methods in Physics Research*, 214(23):253 – 260, 1983.

[23] M. Dragicevic et a. Optimising the strip geometry for very fine pitch silicon strip sensors. *Nucl. Instr. and Meth. in Phys. Res. A 617 (2010) 532.*

[24] G. Auzinger. Analysis of testbeam data of irradiated silicon prototype sensors for the CMS tracker upgrade. *Nucl. Instr. and Meth. in Phys. Res. A*, (0):–, 2013.

[25] Hamamatsu. Hamamatsu. *http://www.hamamatsu.com.*

[26] M. Strelzyk. *Design studies of n-in-p silicon strip sensors for the CMS tracker. Diploma Thesis.* PhD thesis, Institut für Experimentelle Kernphysik. Fakultät für Physik. Karlsruher Institut für Technologie.

[27] A. Dierlamm for the CMS Collaboration. Characterization of silicon sensor materials and designs for the cms tracker upgrade. *Conference Report at VERTEX2012. CMS CR*, 370, 2012.

[28] K.-H. Hoffmann et al. R&D on novel sensor routing and test structure development. *Nucl. Instr. and Meth. in Phys. Res. A*, 628(1):268 – 271, 2011.

[29] Ch. Broennimann et al. Development of an Indium bump bond process for silicon pixel detectors at PSI. *Nucl. Instr. and Meth. in Phys. Res. A 565 (2006) 303.*

[30] A. Macchiolo et al. Performance of thin pixel sensors irradiated up to a fluence of 10^{16} neq/cm^{-2} and development of a new interconnection technology for the upgrade of the ATLAS pixel system. *Nucl. Instr. and Meth. in Phys. Res. A 650 (2011) 145.*

[31] H.C. Theuerer. U. S. Patent. *2, 060, 123*, 1962.

[32] J. Czochralski. Metalle. Z.Phys.Chem. *92:219*, 1918.

[33] S. M. Sze. *Semiconductor Devices, Physics and Technology.* 1985.

[34] P. Dervan. Silicon Detectors for the HL-LHC. Recent RD50 Results. *Pixel 2012, as a poster contribution on behalf of RD50 collaboration.*

[35] G. Kramberger, V. Cindro, I. Dolenc, I. Mandi, M. Miku, and M. Zavrtanik. Performance of silicon pad detectors after mixed irradiations with neutrons and fast charged hadrons. *Nucl. Instr. and Meth. in Phys. Res. A*, 609(23):142 – 148, 2009.

[36] M. Capeans et al. Atlas insertable b-layer technical design report. Technical Report CERN-LHCC-2010-013. ATLAS-TDR-19, CERN, Geneva, Sep 2010.

[37] A. Macchiolo et al. Thin n-in-p pixel sensors and the SLID-ICV vertical integration technology for the ATLAS upgrade at the HL-LHC. *Nucl. Inst. and Meth. A*, 2013.

[38] L. Strder, P. Holl, G. Lutz, and J. Kemmer. Device modeling of fully depletable CCDs. *Nucl. Instr. and Meth. in Phys. Res. A*, 253(3):386 – 392, 1987.

[39] J. Schieck. DEPFET pixels as a vertex detector for the BELLE II experiment. *Nucl. Instr. and Meth. in Phys. Res. A*, (0):–, 2013.

[40] Universitt Bonn, Research group of Norbert Wermes. DEPFET principle.

[41] R. Turchetta. CMOS monolithic active pixel sensors (maps): Developments and future outlook. *Nucl. Instr. and Meth. in Phys. Res. A 582 (2007) 866.*

[42] The STAR experiment. The STAR experiment at the relativistic heavy ion collider, Brookhaven National Laboratory. *http://www.star.bnl.gov/.*

[43] Electronic Instrumentation Laboratory, Pavia, Italy. CMOS monolithic active pixel sensors for charged particle tracking applications. *http://eil.unipv.it/eil/?q=node/24.*

[44] Y. Arai et al. Developments of SOI monolithic pixel detectors. *Nucl. Instr. and Meth. in Phys. Res. A*, 623(1):186 – 188, 2010. 1st International Conference on Technology and Instrumentation in Particle Physics.

[45] I. Perić and C. Kreidl and P. Fischer. Particle pixel detectors in high-voltage CMOS technology. New achievements. *Nuc. Inst. and Meth. in Physics A*, 650(1):158 – 162, 2011. International Workshop on Semiconductor Pixel Detectors for Particles and Imaging 2010.

[46] A. Marras et al. Design of a Monolithic Momentum Detector using a 3D IC Vertical Integration Approach. *presented to the conference: Vertically Integrated Pixel Sensors (VIPS)*, 2010.

[47] M. Bouterfa et al. Charge collection mapping of a novel ultra-thin silicon strip detector for hadrontherapy beam monitoring. *Nucl. Instr. and Meth. in Phys. Res. A*, (0), 2013.

[48] J. Bensinger and T. Rodrigo. Alignment systems in LHC general purpose detectors. *Nucl. Instr. and Meth. in Phys. Res. A 666 (2012) 173.*

[49] M. Fernandez Garcia et al. Semi-transparent silicon strip sensors for the precision alignment of tracking detectors. *Nucl. Instr. and Meth. in Phys. Res. A 461 (2001) 213.*

[50] D. Bassignana et al. Silicon microstrip detectors for future tracker alignment systems. *Nucl. Instr. and Meth. in Phys. Res. A*, 628(1):276 – 281, 2011. VCI 2010.Proceedings of the 12th International Vienna Conference on Instrumentation.

[51] Axis Communications. CCD and CMOS sensor technology. *Technical white paper.*

[52] CMS Collaboration. Performance and operation of the cms electromagnetic calorimeter. *Journal of Instrumentation*, 5(03):T03010, 2010.

[53] Super-Kamiokande. The Super-Kamiokande experiment. Detection principle. *http://www-sk.icrr.u-tokyo.ac.jp/sk/detector/howtodetect-e.html.*

[54] Microscopy resource center. Avalanche Photodiodes. *http://www.olympusmicro.com/primer/digitalimaging/concepts/avalanche.html.*

[55] N. D'Ascenzo and V. Saveliev. Study of silicon photomultipliers for the medical imaging systems. *Nucl. Instr. and Meth. in Phys. Res. A*, 695(0):265 – 267, 2012. New Developments in Photodetection NDIP11.

[56] P. Allport A. Affolder and G. Casse. Charge collection efficiency measurements of heavily irradiated segmented n-in-p and p-in-n silicon detectors for use at the super-lhc. *IEEE TRANSACTIONS ON NUCLEAR SCIENCE, VOL. 56, NO. 3, JUNE 2009.*

[57] M. Kohler et al. Beam Test Measurements With Planar and 3D silicon Strip Detectors Irradiated to sLHC Fluences. *IEEE Trans. Nucl. Sci. NS-58(3).*

[58] V. Radeka. Signal, noise and resolution in position-sensitive detectors. *IEEE Transaction on Nuclear Science NS-26 (1979) 225.*

[59] D. Bassignana et al. Development of a novel 2D position-sensitive semiconductor detector concept. *Journal of instrumentation, 2012 JINST 7 C04008.*

[60] D. Bassignana et al. 2D position sensitive microstrip sensors with charge division along the strip: Studies on the position measurement error. *Nuc. Instrum. Meth. A*, 732(0):186 – 189, 2013. Vienna Conference on Instrumentation 2013.

[61] T. Rohe et al. Fluence dependence of charge collection of irradiated pixel sensors. *Nucl. Instr. and Meth. in Phys. Res. A*, 552(12):232 – 238, 2005. Proceedings of the 5th International Conference on Radiation Effects on Semiconductor Materials, Detectors and Devices.

[62] G. Casse. Recent achievements of the atlas upgrade planar pixel sensors r&d project. *JINST 9 C04006.*

[63] W. Dulinski Y Gornushkin M. Deveaux, G. Claus. G. Deptuch and M. Winter. Neutron radiation hardness of monolithic active pixel sensors for charged particle tracking. *Nuclear Instruments and Methods in Physics Research Section A: Accelerators, Spectrometers, Detectors and Associated Equipment*, 512(12):71 – 76, 2003. Proceedings of the 9th European Symposium on Semiconductor Detectors: New Developments on Radiation Detectors.

[64] Radiation effects in silicon-on-insulator transistors with back-gate control method fabricated with {OKI} semiconductor 0.20m fd-soi technology. *Nucl. Instr. and Meth. in Phys. Res. A*, 636(1, Supplement):S62 – S67, 2011. 7th International.

[65] I Peric. Active pixel sensors in high-voltage CMOS technologies for ATLAS. *Journal of Instrumentation*, 7(08):C08002, 2012.

[66] H. Spieler. *Semiconductor Detector Systems.* 2006.

[67] Glenn F. Knoll. *Radiation detection and measurement.* 2010.

[68] G. Lutz. *Semiconductor Radiation Detectors: Device Physics.* 1999.

[69] Michaell Moll. *"Radiation Damage in Silicon Particle Detectors - microscopic defects and macroscopic properties-".* PhD thesis, University of Hamburg, 1999.

[70] Gregor Kramberger. *"Signal development in irradiated silicon detectors".* PhD thesis, University of Ljubljana. Faculty for Mathematics and Physics, 2001.

[71] Nicola Pacifico. *Radiation Damage study on innovative silicon sensors for the CMS tracker upgrade.* PhD thesis, University of Bari, 2012.

[72] Frank Hartmann. *Evolution of Silicon Sensor Technology in Particle Physics.* 2008.

[73] S.I. Parker et al. 3D- A Proposed new architecture for solid-state radiation detectors. *Nucl. Instrum. Meth. A 395 (1997) 328.*

[74] Giulio Pellegrini. *Technology development of 3D detectors for high energy physics and medical imaging.* PhD thesis, University of Glasgow, 2002.

[75] S. Ramo. Currents induced by electron motion. *Proc. IRE, 27, 584585*, 1939.

[76] G Lindström et al. Radiation hard silicon detectorsdevelopments by the RD48 (ROSE) collaboration. *Nucl. Instrum. and Meth. A*, 466(2):308, 2001.

[77] M. Huhtinen. Simulation of non-ionising energy loss and defect formation in silicon. *Nucl. Instr. and Meth. in Phys. Res. A*, 491(12):194 – 215, 2002.

[78] R. Wunstorf et al. Investigations of donor and acceptor removal and long term annealing in silicon with different boron/phosphorus ratios. *Nucl. Instr. and Meth. in Phys. Res. A*, 377(23):228 – 233, 1996. Proceedings of the Seventh European Symposium on Semiconductor.

[79] R. Wunstorf. *A Systematic investigation of the radiation hardness of silicon detectors for high-energy physics experiments.* PhD thesis, DESY, 1992.

[80] G. C. Messenger and M. S. Ash. *Semiconductor Radiation Detectors: Device Physics.* 1992.

[81] G Kramberger et al. Determination of effective trapping times for electrons and holes in irradiated silicon. *Nucl. Instr. and Meth. in Phys. Res. A*, 476(3):645 – 651, 2002. Proc. of the 3rd Int. Conf. on Radiation Effects on Semiconductor Materials, Detectors and Devices.

[82] G. Casse et al. Enhanced efficiency of segmented silicon detectors of different thicknesses after proton irradiations up to $1 \cdot 10^{16} neq/cm^2$. *Nucl. Instr. and Meth. in Phys. Res. A*, 624(2):401 – 404, 2010. New Developments in Radiation Detectors. Proc. of the 11th European Symposium on Semiconductor Detectors.

[83] M. Miku et al. Study of anomalous charge collection efficiency in heavily irradiated silicon strip detectors. *Nucl. Instr. and Meth. in Phys. Res. A*, 636(1, Supplement):S50 – S55, 2011. 7th International Hiroshima Symposium on the Development and Application of Semiconductor Tracking Detectors.

[84] Instituto de Física de Cantabria. *http://www.ifca.es/*.

[85] Thomas Bergauer. *Process Quality Control of Silicon Strip Detectors for the CMS Tracker.* PhD thesis, Institut für Hochenergiephysik der

Österreichischen Akademie der Wissenschaften und am Atominstitut der Österreichischen Universitäten, 2004.

[86] Alexander Furgeri. *Quality Assurance and Irradiation studies on CMS silicon strip sensors.* PhD thesis, Fakultät für Physik der Universität Karlsruhe (TH), 2006.

[87] Centro Nacional de Microelectrónica de Barcelona. CNM-IMB. *http://www.imb-cnm.csic.es/index.php?lang=en.*

[88] Cascade Microtech. *http://www.cmicro.com.*

[89] Keithley Instruments Inc. *www.keithley.com.*

[90] Agilent Technologies. *www.agilent.com.*

[91] C. W. Gwyn. Calculated small signal characteristics for irradiated pn junctions. *IEEE Trans. Nucl. Sci. NS-19(355)*, 1972.

[92] QPHOTONICS. *http://www.qphotonics.com/.*

[93] Standford Research System. *http://www.thinksrs.com/.*

[94] Schäfter + Kirchhoff. Optics, Metrology and Photonics. *http://www.sukhamburg.com/.*

[95] Alivaba system. *http://www.alibavasystems.com/.*

[96] Minimum Ionizing Particle. http://www.utef.cvut.cz/en/index.php. *Institute of experimental and applied Phicics. Czech Technical University in Prague.*

[97] Neil S. Patel et al. Treatment planning dosimetric parameters for a 90-Y coil source used in intravascular brachytherapy. *Cardiovascular Radiation Medicine*, 2(2):83 – 92, 2001.

[98] H. Spieler. Energy Deposition in the Detector and Spectrum Formation-1. *Lecture Notes - Physics 198, Spring Semester 1999 - UC Berkeley* , 1999.

[99] Paul Sherrer Institut. *http://www.psi.ch/.*

[100] Lakeshore. *http://www.lakeshore.com/.*

[101] Honeywell Sensing and Control. *http://sensing.honeywell.com/.*

[102] DESY test beam facilities. *http://testbeam.desy.de/.*

[103] CMS DESY group. *http://cms.desy.de/e48943/.*

[104] Advanced European Infrastructures for Detectors at Accelerators. *http://aida.web.cern.ch/aida/index.html.*

[105] Hanno Perrey. An EUDET/AIDA Pixel Beam Telescope for Detector Development. (AIDA-CONF-2013-001), Nov 2012.

[106] Artem Kravchenko. MIMOSA26 sensor. *https://twiki.cern.ch/twiki/bin/view/MimosaTelescope/MIMOSA26.*

[107] D. Cussans. A trigger/timing logic unit for ilc test-beams. *http://cds.cern.ch/record/1091502?ln=en.*

[108] CAEN,Electronic Instrumentation. *http://www.caen.it/csite.*

[109] NIM,Nuclear Instrumentation Module. *http://en.wikipedia.org/wiki/Nuclear- _Instrumentation_Module.*

[110] Jozef Stefan Institute and Department of Physics, University of Ljubljana, SI-1000 Ljubljana, Slovenia.

[111] Karlsruhe Institute of Technology. karlsruhe. germany. http://www.ekp.kit.edu/english/264.php.

[112] R. Turchetta. Spatial resolution of silicon microstrip detectors. *Nucl. Instrum. Meth. A 335 (1993) 44.*

[113] C. Rubbia H. Foeth, R. Hammarstrom. On the localization of the position of the particle along the wire of a multiwire proportional chamber. *Nuc. Inst. and Meth. in Physics Research 109 (1973) 521.*

[114] P. Schuberlin et al. Low mass cylindrical multiwire proportional chamber with unambiguous dual coordinate readout. *Nuc. Inst. and Meth. in Physics Research 131 (1975) 39.*

[115] I. Linscott G. Moneti A. Feinberg, N. Horwitz. A frameless, cylindrically shaped, multiwire proportional chamber using charge division readout. *Nuc. Instrum. Meth. in Physics Research 141 (1977) 277.*

[116] M.L. Awcock R.B. Owen. One and two dimensional position sensing semiconductor detectors. *IEEE Transaction on Nuclear Science NS-15 (1958) 290.*

[117] J. K. Carman et al. Longitudinal resistive charge division in multi-channel silicon strip sensors.

[118] SPICE electronic circuit simulator. www.linear.com/designtools/software/.

[119] Beetle - a readout chip for LHCb. *http://www.kip.uni-heidelberg.de/lhcb/.*

[120] N. Bachetta et al. SPICE analysis of signal propagation in Si microstrip detectors.

[121] Virtuoso spectre data sheet, cadence. available at http://www.cadence.com/ products/custom ic/index.aspx.

[122] R. Brun et al. ROOT An Object-Oriented Data Analysis Framework. *http://root.cern.ch/drupal/.*

[123] R.Marco-Hernandez et al. A portable readout system for microstrip silicon sensors (ALIBAVA). *Nuclear Science Symposium Conference Record, 2008. NSS '08. IEEE 19-25 Oct. 2008 Page(s):3201 - 3208.*

[124] Taylor Cunnington. Examining long ladder limits for ILC silicon strip detectors. *Diploma Thesis. University of California.*

[125] Y. Allkofer et al. Design and performance of the silicon sensors for the cms barrel pixel detector. *Nucl. Instr. and Meth. in Phys. Res. A*, 584(1):25 – 41, 2008.

[126] G. Bolla et al. Design and test of pixel sensors for the CMS experiment. *Nucl. Instrum. Meth. A 461 (2001) 182.*

[127] R. Kaufmann. *Development of radiation hard pixel sensors for the CMS experiment.* PhD thesis, Universität Zürich, 2001.

[128] G. Bolla et al. Sensor development for the CMS pixel detector. *Nucl. Instrum. Meth. A 485 (2002) 89.*

[129] G. Bolla et al. Irradiation studies of silicon pixel detectors for CMS. *Nucl. Instrum. Meth. A 501 (2003) 160.*

[130] A. Dorokhov et al. Tests of silicon sensors for the CMS pixel detector . *Nucl. Instrum. Meth. A 530 (2004) 71.*

[131] T.Rohe et al. Position Dependence of Charge Collection in Prototype Sensors for the CMS Pixel Detector. *IEE Trans. Nucl. Sci. NS-51 (2004) 1150.*

[132] D. Pennicard et al. Simulation Results from Double Sided 3D Detectors. *IEEE Trans. Nucl. Sci. NS-54(4).*

[133] M. Barbero et al. Design and test of the CMS pixel readout chip. *Nucl. Instr. and Meth. A 517 (2004) 349.*

[134] G. Pellegrini et al. First double-sided 3D detectors fabricated at CNM-IMB. *Nucl. Instr. And Meth. A 592*, 2008.

[135] C. kenney and S.I. Parker. Silicon detectors with 3D electrode arrays: fabrication and initial test result. *IEEE Trans. Nucl. Sci. NS-46(4).*

[136] J. Llacer. Planar and coaxial high purity germanium radiation detectors. *Nucl. Inst. and Meth. A 98 (1972) 259.*

[137] PSI46 Pixel Chip - External Specification.

[138] H.Chr. Kästli et al. Design and performance of the CMS pixel detector readout chip. *Nucl. Instr. and Meth. in Phys. Res. A 565 (2006) 188.*

[139] A. Starodumov et al. Qualification procedures of the CMS pixel barrel modules. *Nucl. Instr. and Meth. in Phys. Res. A 565 (2006) 67.*

[140] D. Kotliski et al. The control and readout systems of the CMS pixel barrel detector. *Nucl. Instr. and Meth. in Phys. Res. A 565 (2006) 73.*

[141] D. Oleson and R. Horisberger. Crosstalk in the CMS Pixel Tracker Read-Out-Chip. Technical report, University of Nebraska-Lincoln.

[142] M. Dentan et al. DMILL, A Mixed Analog-Digital Radiation-Hard. BICMOS Technology for High Energy Physics Electronics. *IEEE Trans. Nucl. Sci. NS-43(1763).*

[143] CMS-PIRE pixel group. PixelPIRE testboard.

[144] A. Starodumov et al. CMS pixel module test procedures. *Silicon Detector Workshop. Split, Croatia, October 8-10, 2012.*

[145] CMS pixel group. PSI46 software.

[146] S. Dambach. *CMS pixel module readout optimization and study of the lifetime in the semileptonic decay mode.* PhD thesis, Eidgenössische Technische Hochschule Zürich, ETHZ, 2009.

[147] M. Fernandez et al. Radiation resistance of double-type double-sided 3D pixel sensors. *Nucl. Instr. And Meth. A* , 732(0):137 – 140, 2013. Vienna Conference on Instrumentation 2013.